nature

https://doi.org/10.1038/s41586-019-1904-x

Supplementary information

Conversion of non-van der Waals solids to 2D transition-metal chalcogenides

In the format provided by the authors and unedited

Zhiguo Du, Shubin Yang, Songmei Li, Jun Lou, Shuqing Zhang, Shuai Wang, Bin Li, Yongji Gong, Li Song, Xiaolong Zou & Pulickel M. Ajayan

Supplementary Information for

Conversion of non-van der Waals solids to 2D transition-metal chalcogenides

Zhiguo Du[1], Shubin Yang[1]*, Songmei Li[1], Jun Lou[2], Shuqing Zhang[3], Shuai Wang[1], Bin Li[1], Yongji Gong[1], Li Song[4], Xiaolong Zou[3] & Pulickel M. Ajayan[2]*

[1]Key Laboratory of Aerospace Advanced Materials and Performance of Ministry of Education, School of Materials Science and Engineering, Beihang University, Beijing, China

[2]Department of Materials Science and NanoEngineering, Rice University, Houston, TX, USA

[3]Shenzhen Geim Graphene Center and Low-Dimensional Materials and Devices Laboratory (LDMD), Tsinghua-Berkeley Shenzhen Institute (TBSI), Tsinghua University, Shenzhen, China

[4]National Synchrotron Radiation Laboratory, CAS Center for Excellence in Nanoscience, University of Science and Technology of China, Hefei, China

*e-mail: yangshubin@buaa.edu.cn; ajayan@rice.edu

Table of Contents

S1. Materials and Methods

Materials.

Raw materials: Mo (99.5%, 10μm, Aladdin Reagent), Ge (99.999%, 100 mesh, Alfa Aesar), graphite (99.9%, 10 mesh, Alfa Aesar), Ti (99.99%, 300 mesh, Aladdin Reagent), Nb (99.95%, 325 mesh, Aladdin Reagent), W (99.99%, 12 μm, Aladdin Reagent), Y (99.9%, Aladdin Reagent), Al (99.95%, 25μm, Aladdin Reagent), Sn (99.5%, 100 mesh, Aladdin Reagent), Se (99.9%, Macklin), P (98.5%, Aladdin Reagent), MoB (99%, Alfa Aesar), $MoSi_2$ (99.9%, 1 μm, HAOXI Research Nanomaterials, Inc.), bulk WS_2 (99.9%, 25 μm, Aladdin Reagent), isopropyl alcohol (IPA, Beijing Chemical Works), N-methyl-pyrrolidinone (NMP, Aladdin Reagent), Nylon Membrane Filters (Φ 50 mm, 0.22 μm, Shanghai Xinya Purification Equipment Co., Ltd.). Ti_3SiC_2 and Ti_2AlC MAX phases were purchased from Kanthal ® (Sweden). Ta_2AlC was purchased from Laizhou Kai Kai Ceramic Materials Co., Ltd. (Yantai, China). Nb_2AlC and Mo_2Ga_2C were purchased from 11 Technology Co., Ltd. (Jilin, China). All the reagents were purchased without further purification.

Synthesis of MAX phases.

Synthesis of MAX-$(W_{2/3}Y_{1/3})_2AlC$ (ref. [1]): In a glove box with oxygen level of less than 0.1 ppm, elemental powders of W, Y, Al and graphite with the desired stoichiometric ratios were sealed in an agate container with agate balls. And then the mixed powders were milled at 600 rpm for 10 h (XQM-1). The milled powders were then transferred to an alumina crucible, and heated in tube furnace (NBD-T1700-80) at a rate of 3 K min^{-1} until 1723 K and maintained at such a high temperature for 2 h under Ar flow. After cooling to room temperature, the bulk was ground, producing MAX-$(W_{2/3}Y_{1/3})_2AlC$.

Synthesis of MAX-$(Ti_{1/2}Nb_{1/2})_2AlC$ (ref. [2]): Similar to the fabrication of above MAX-$(W_{2/3}Y_{1/3})_2AlC$, elemental Ti, Nb, Al powders and graphite with a molar ratio of 1:1:1.2:1 were ball milled at 600 rpm for 20 h. The mixtures were then heated at a heating rate of 3 K min^{-1} to 1773 K for 1 h under Ar flow. After cooling to room temperature, the bulk was ground to produce MAX-$(Ti_{1/2}Nb_{1/2})_2AlC$.

Synthesis of MAX-Mo_2TiAlC_2 (ref. [3]): Similar to the fabrication of above MAX-$(W_{2/3}Y_{1/3})_2AlC$, Mo, Ti, Al and graphite powders were ball milled at 600 rpm for 20 h. The Mo/Ti/Al/graphite molar ratio was 2:1:1.1:2. Powder mixture was then heated to 1873 K at 3 K min^{-1} and held there for 4 h under Ar flow. After cooling, the bulk was ground to obtain Mo_2TiAlC_2.

Synthesis of MAX-Ti_2SnC (ref. [4]): Commercial Ti, Sn and graphite powders with a molar ratio of 2:1.5:1 were firstly sealed in an agate container, and then milled at 600 rpm for 20 h. The resultant powders were cold-pressed at 30 MPa into a cylinder with a diameter of 20 mm. The as-prepared cylinder was heated to 1573 K at a heating rate of 3 K min^{-1} and then maintained there for 2 h. After cooling to room temperature, the bulk was ground, producing MAX-Ti_2SnC.

Conversion of non-van der Waals solids to transition-metal chalcogenides.

Conversion of non-van der Waals solid MAX phases to accordion-like transition-metal chalcogenides: In a standard procedure, transition-metal chalcogenides were prepared by the reaction of MAX phases, borides or silicides with chalcogen vapours at temperatures of 1073-1373 K, subsequently associated with a natural cooling process. To inhibit the re-stacking of already expanded layers, the conversion reaction of MAX phases with chalcogen vapours was conducted at high temperatures and subsequent fast quenching treatment. Taking highly expanded accordion-like Y-doped WS_2 as an example, 300 mg MAX-$(W_{2/3}Y_{1/3})_2AlC$ was heated under Ar flow, and H_2S/Ar (10 vol.% H_2S) mixture was injected when the temperature reached 1273 K. After the

conversion reaction, the expanded sample was rapidly transferred to a low temperature zone (room temperature) to generate highly expanded accordion-like Y-doped WS_2.

Conversion of thin non-van der Waals solid to 2D transition-metal chalcogenides: Typically, a transition-metal carbide MXene-Mo_2CT_x (T_x represents the surface terminations, such as -O, -OH and -F) was firstly fabricated via chemical etching of Mo_2Ga_2C (ref. [5]). And then the Mo_2CT_x was used as a starting material to react with chalcogen vapours at temperatures of 873-1373 K, similar to the procedures of converting MAX phases to transition-metal chalcogenides.

Collection of side products.

The side products (GeS, SiSe and SnS) were collected from the output end of furnace tube after the transformation of MAX phases to transition-metal chalcogenides.

Liquid-phase exfoliation of accordion-like MoS_2 and Y-doped WS_2.

According to the classical liquid-phase exfoliation method[6], accordion-like MoS_2 or Y-doped WS_2 powders were dispersed in isopropyl alcohol (IPA) or N-methyl-pyrrolidinone (NMP) solvent with a concentration 2 mg mL^{-1}, and then sonicated for 0.5-4 h with point probe under a power output of 300 W. Then the dispersions were centrifuged at 1500 rpm for 45 min to obtain the supernatants. The concentrations of exfoliated transition-metal dichalcogenides in the supernatants were evaluated by UV-vis-IR spectra and used to calculate the production yields.

Preparation of TEM samples.

TEM samples were prepared by dropping the sonicated dispersions of accordion-like transition-metal chalcogenides to the holey carbon grids. Cross-sectional TEM and HRTEM samples were prepared by ultrathin sectioning treatment of the accordion-like transition-metal chalcogenides. Specifically, the accordion-like transition-metal chalcogenides were imbedded in spurr resin and then immobilized in spur resin at 343 K for 24 h for solidification. The ultrathin sections, obtained

by cutting the above-mentioned solidified bulk with a diamond knife in an ultramicrotome (Leica EM UC7) at room temperature, were dispersed on bare carbon grids for cross-sectional TEM and HRTEM measurements.

Electrical conductivity measurement.

Specifically, the powder samples were initially filled in the sample cell and then given a pressure of 10 MPa. After steading for 10 min at the high pressure, the electrical resistance value (ρ) was stable and recorded. The electrical conductivity (κ) was calculated based on the equation of $\kappa = 1/\rho$.

Electrocatalytic measurements.

The electrocatalytic properties for HER were measured in a three-electrode configuration with an Ar-saturated 1 M KOH electrolyte, by using graphite rod, Ag/AgCl and glass carbon with active materials as counter, reference and working electrodes, respectively. The electrochemical measurements were performed on an Autolab workstation (PGSTAT302N). Polarization curves were carried out at a scan rate of 10 mV s^{-1} and stability measurements were recorded after 1000 cyclic voltammograms (CV) sweeps at a scan rate of 50 mV s^{-1}. All the potentials were converted to values with reference to a reversible hydrogen electrode (RHE).

Theoretical Calculations.

All the first-principles calculations were performed using projector-augmented wave method[7] within the framework of density functional theory as implemented in Vienna Ab initio Simulation Package[8]. The exchange and correlation functional were treated using the generalized gradient approximation of Perdew, Burke and Ernzerhof[9]. To obtain converged results, the Brillouin zones were sampled on Monkhorst-Pack grid[10] with a maximum spacing of 0.02 $Å^{-1}$, corresponding to 7×7×1 *k*-point grids for 4×4 supercells. The structures were fully relaxed with kinetic energy cutoff

of 500 eV and forces of all components were less than 0.01 eV $Å^{-1}$. A vacuum region of more than 15 Å was added to eliminate the possible interactions between layers. The electronic properties were calculated by Heyd-Scuseria-Ernzerhof 06 (HSE06)[11] hybrid functional to obtain accurate bandgap information.

S2. Characterization of 2D transition-metal chalcogenides derived from non-van der Waals solids

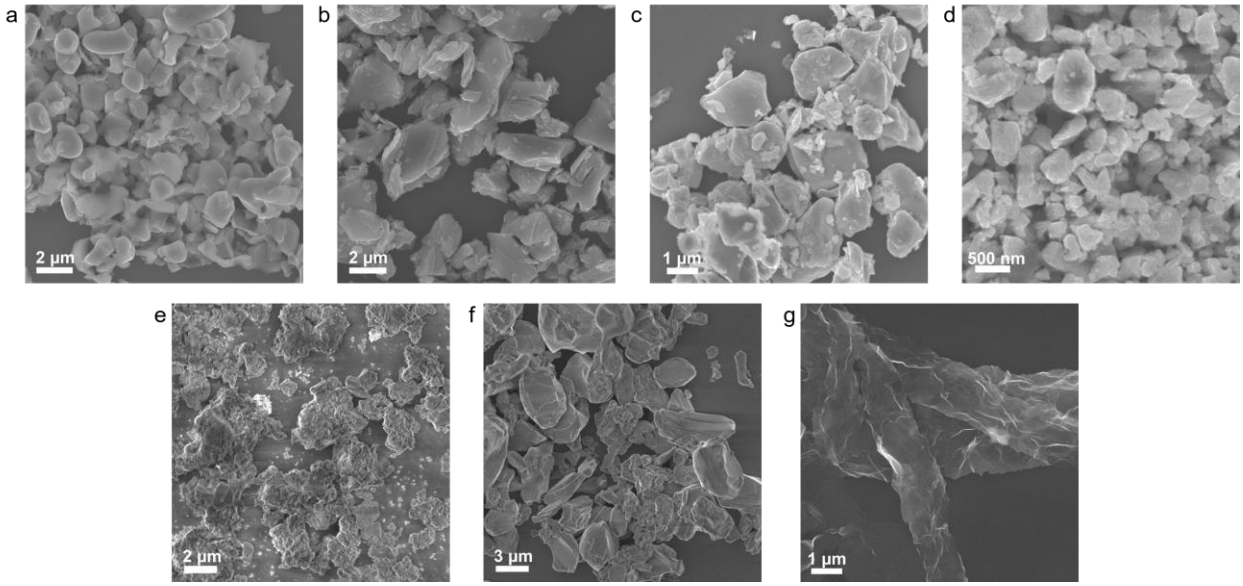

Fig. S1. Morphology characterization of various non-van der Waals solids. a-g, SEM images of (**a**) MAX-Mo_2GeC, (**b**) MAX-Ti_3SiC_2, (**c**) MoB, (**d**) $MoSi_2$, (**e**) MAX-$(W_{2/3}Y_{1/3})_2AlC$, (**f**) MAX-$(Ti_{1/2}Nb_{1/2})_2AlC$ and (**g**) MXene-Mo_2CT_x.

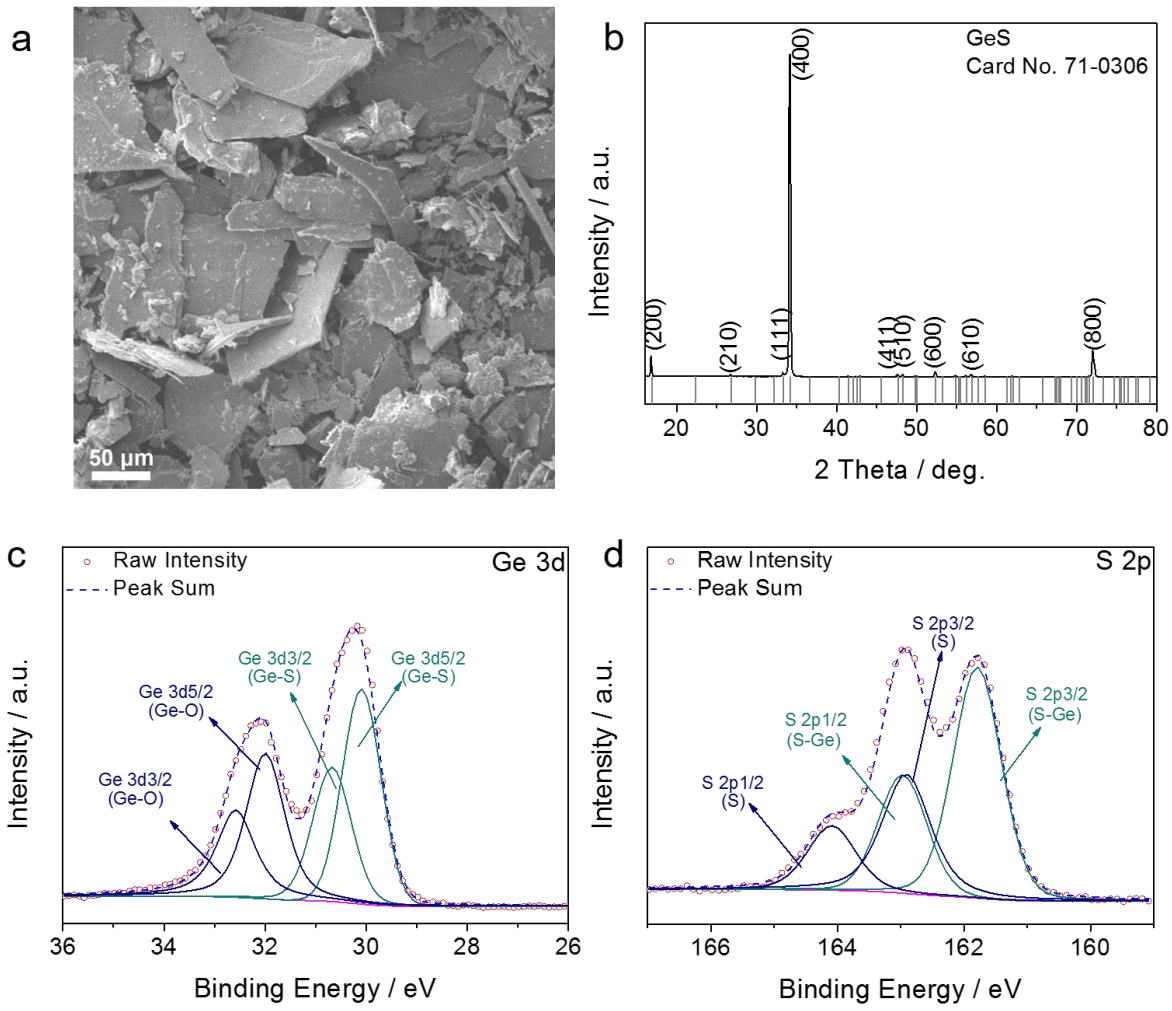

Fig. S2. Material characterization of side product GeS collected at the output end of furnace tube after the reaction of MAX-Mo_2GeC with H_2S gas at 1073 K. a, SEM image, and **b**, XRD patterns of GeS. **c**, High-resolution Ge 3d XPS spectra, and **d**, high-resolution S 2p XPS spectra. After the reaction between MAX-Mo_2GeC and H_2S gas at 1073 K, the side product was collected at the output end of furnace tube. As shown in Fig. S2a, the SEM image shows numerous layered bulks with sizes of hundreds of micrometers. XRD patterns of the side product exhibit the typical peaks at 16.9°, 34.1°, 52.4° and 72.1° (Fig. S2b), indexed to the (200), (400), (600) and (800) facets of GeS (JCPDS No. 71-0306), respectively. To further confirm the composition of the side product, X-ray photoelectron spectroscopy measurement and analysis were conducted. In Fig. S2c, high-

resolution Ge 3d spectra could be fitted into two doublets at 30.1/30.7 eV and 32.0/32.6 eV, respectively. The first doublet at 30.1 and 30.7 eV is indexed to the Ge 3d5/2 and Ge 3d3/2 peaks for Ge-S bonds, respectively. The second doublet at 32.0 and 32.6 eV is assigned to the Ge 3d5/2 and Ge 2d3/2 peaks for the Ge-O bonds, respectively, demonstrating that the side product GeS was slightly oxidized during our collection process. As shown in Fig. S2d, high-resolution S 2p spectra could be deconvoluted into two doublets, in which one at 161.8 and 163.0 eV is attributed to S 2p3/2 and S 2p1/2 of S-Ge bonds in the GeS, respectively; the other at 162.9 and 164.1 eV is corresponding to elemental sulfur, respectively. Based on all the results for the side product, it is clear that Ge-species could be extracted from MAX-Mo_2GeC under high temperatures.

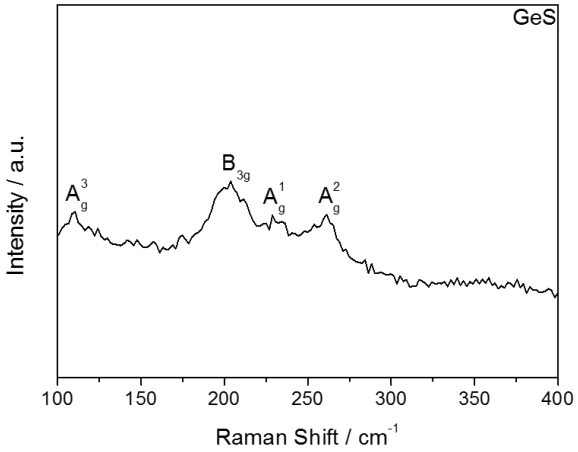

Fig. S3. Raman spectra of side product GeS collected at the end of furnace tube after the reaction of MAX-Mo_2GeC with H_2S gas at 1073 K. There are four peaks at 111, 211, 240 and 270 cm^{-1}, corresponding to A_g^3, B_{3g}, A_g^1 and A_g^2 phonon modes, respectively.

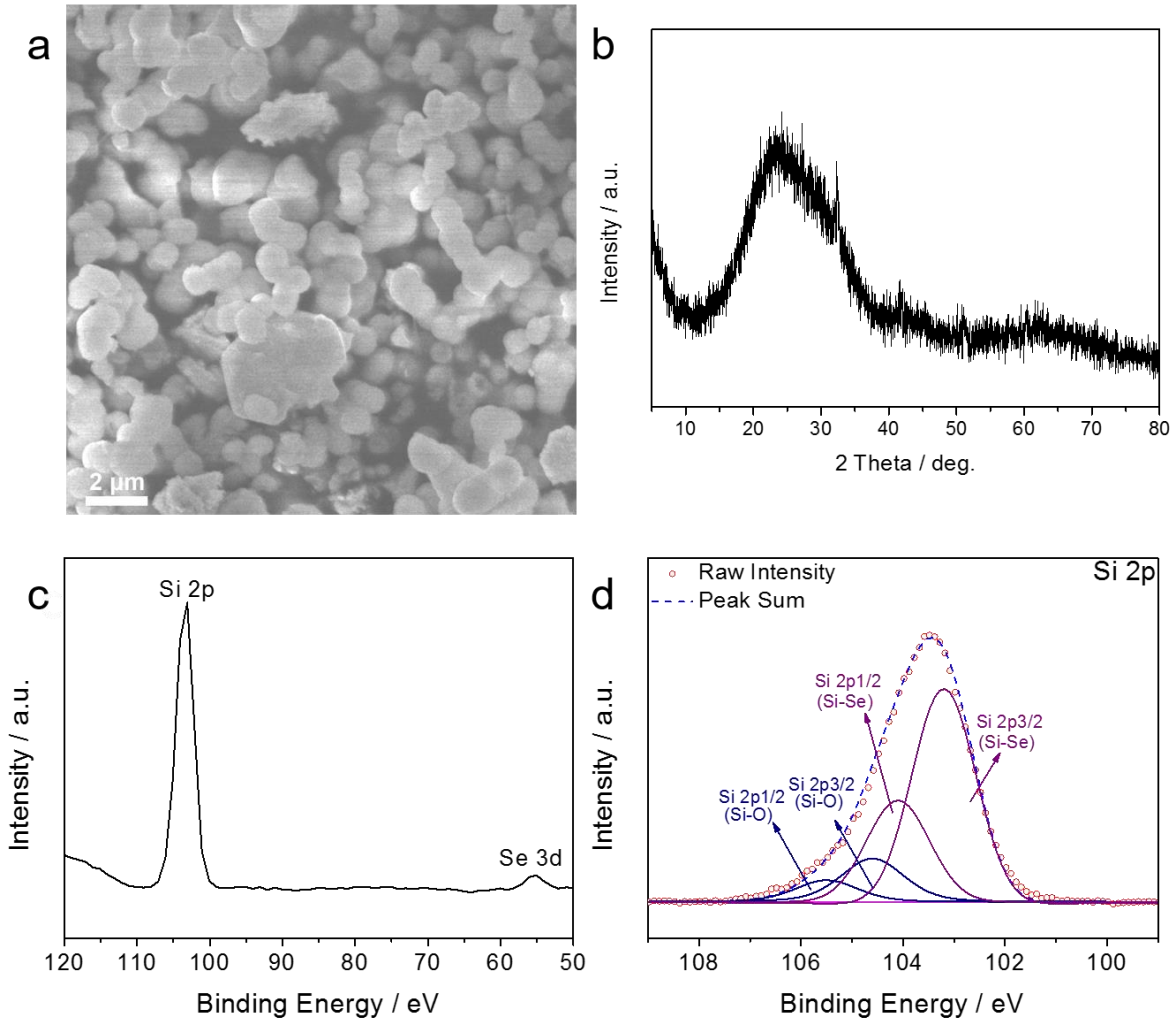

Fig. S4. Material characterization of side product SiSe collected at the output end of furnace tube after the reaction of MAX-Ti_3SiC_2 with Se vapour at 1173 K. a, SEM image, and **b**, XRD patterns of side product SiSe. **c**, XPS survey, and **d**, high-resolution Se 3d XPS spectrum of side product SiSe.

After the reaction of MAX-Ti_3SiC_2 with Se vapour at 1173 K, the side product was collected at the output end of furnace tube. As shown in Fig. S4a, the SEM image shows numerous particles. XRD patterns of the side product (Fig. S4b) exhibit no obvious diffraction peaks, possibly due to amorphous state and metastable nature of the side product. To further confirm the composition of the side product, X-ray photoelectron spectroscopy measurement and analysis were conducted. In

Fig. S4c, the XPS survey spectra disclose the existence of Si and Se species in the side product. As shown in Fig. S4d, high-resolution Si 2p spectra could be fitted to two peaks at 103.2 and 104.1 eV for Si 2p3/2 and Si 2p1/2, respectively, which are assigned to Si-Se bonds. In addition, two peaks at 104.6 and 105.5 eV are indexed to Si 2p3/2 and Si 2p1/2, respectively, corresponding to the Si-O bonds in SiSe due to the oxidation in air. Based on all the results for the side product, it can be concluded that Si-species are extracted from the reaction of MAX-Ti_3SiC_2 with Se vapour.

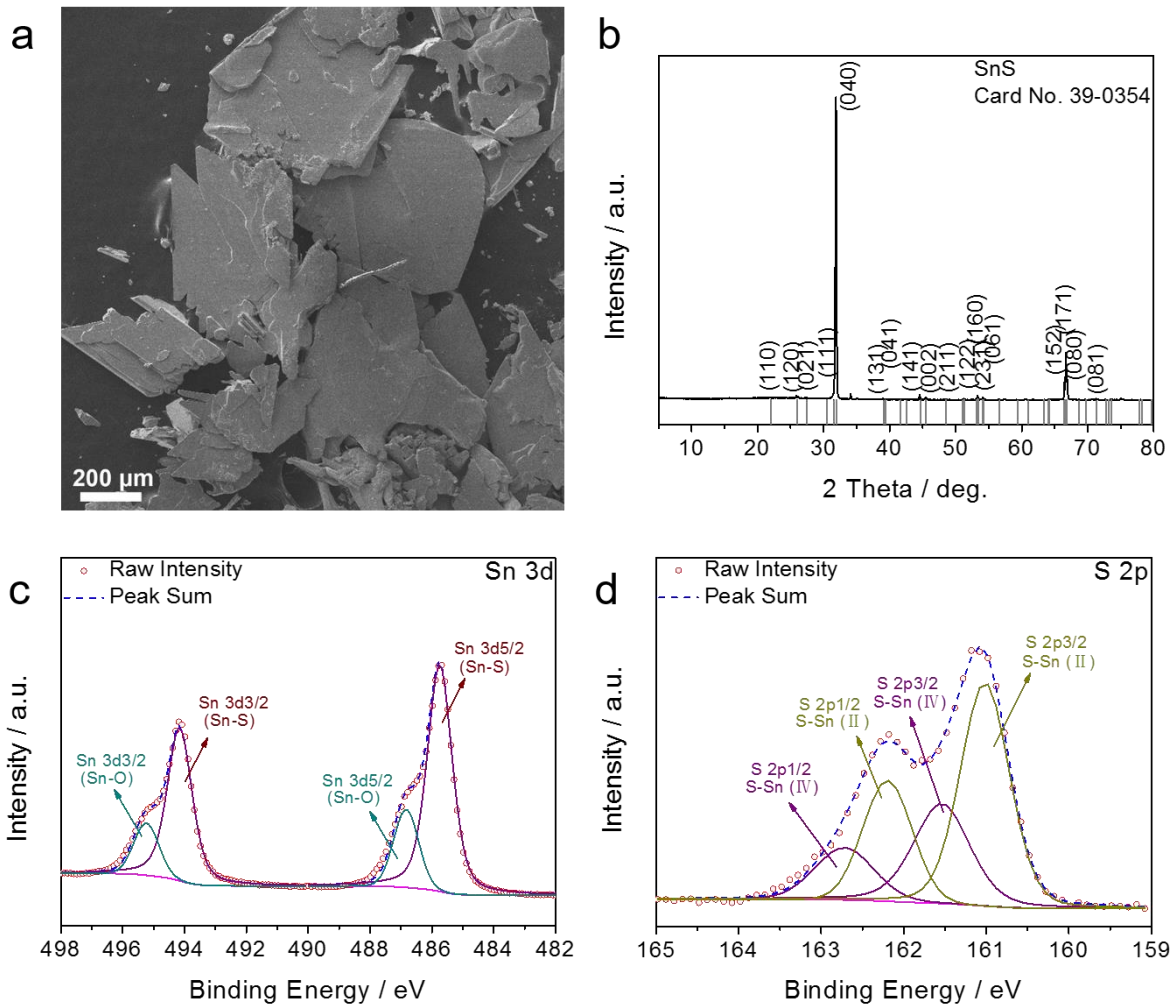

Fig. S5. Material characterization of side product SnS collected at the output end of furnace tube after the reaction of MAX-Ti_2SnC with H_2S gas at 1173 K. a, SEM image, and **b**, XRD patterns of side product SnS. **c**, High-resolution Sn 3d XPS spectra, and **d**, high-resolution S 2p XPS spectra of side product SnS.

After the reaction of MAX-Ti_2SnC with H_2S gas at 1173 K, the side product was collected at the end of furnace tube. As shown in Fig. S5a, a great deal of layered bulks with the sizes of several hundreds of micrometers were observed. XRD patterns (Fig. S5b) exhibit five prominent diffraction peaks at 26.0°, 31.8°, 44.7°, 45.5° and 66.6°, indexed to (120), (040), (141), (002) and (171) facets of SnS (JCPDS No. 39-0354), respectively. To further confirm the composition of the

side product, X-ray photoelectron spectroscopy measurement was conducted. In Fig. S5c, high-resolution Sn 3d spectra could be fitted into two peaks at 485.7 and 494.1 eV for Sn 3d5/2 and Sn 3d3/2, respectively, which are assigned to Sn-S bonds. In addition, two peaks at 486.8 and 495.2 eV for Sn 3d5/2 and Sn 3d3/2, respectively, are assigned to the Sn-O bonds due to the oxidation in air. As shown in Fig. S5d, high-resolution S 2p spectra can be deconvoluted into two doublets, in which one doublet shows two peaks at 161.0 and 162.2 eV for S 2p3/2 and S 2p1/2 peaks of S-Sn (II) bonds, respectively; another doublet exhibits two peaks at 161.5 and 162.7 eV for S 2p3/2 and S 2p1/2 peaks of S-Sn (IV) bonds[12], respectively. Based on the above-mentioned results for the side product, it is known that Sn-species can be extracted from MAX-Ti_2SnC during our conversion reaction.

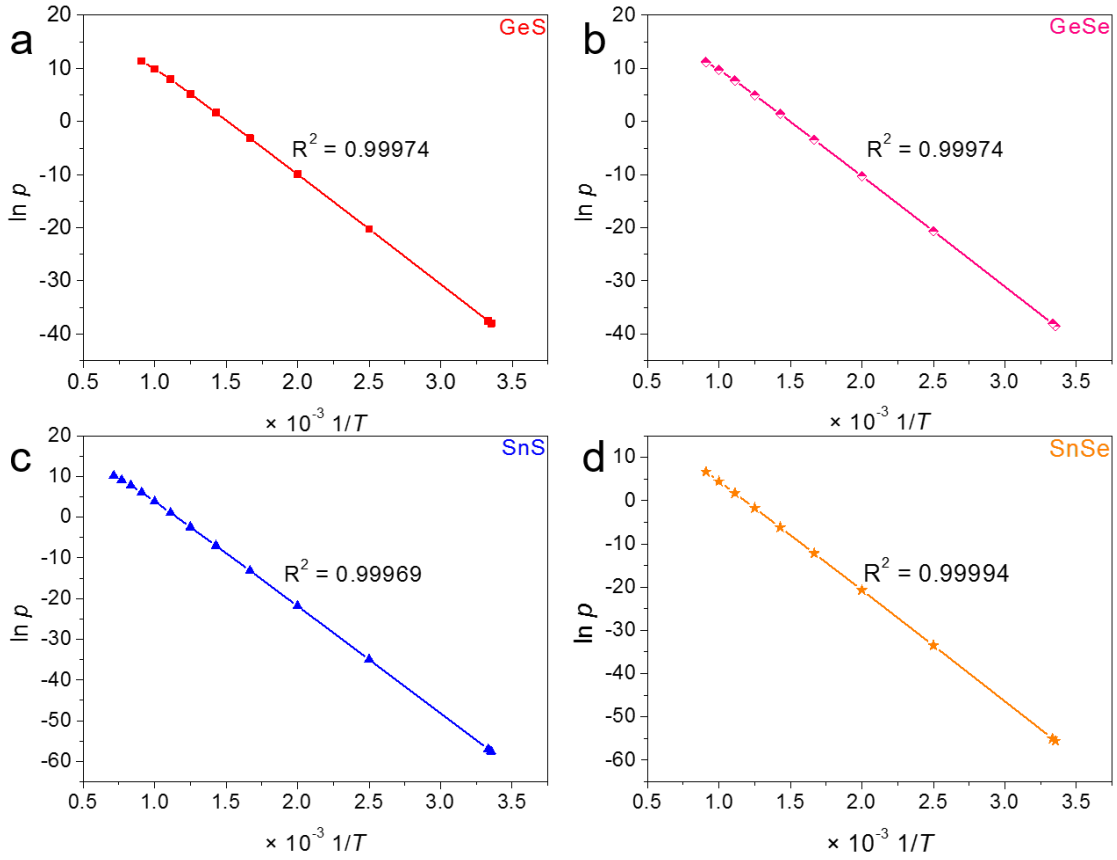

Fig. S6. Clausius-Clapyron equation plots of 1/*T* versus ln*p*. a-d, Clausius-Clapyron equation plots of 1/*T* versus ln*p* for GeS (**a**), GeSe (**b**), SnS (**c**) and SnSe (**d**), showing linear curves, demonstrating that Clausius-Clapyron equation can be applied to evaluate the relationship between vapour pressure and reaction temperature.

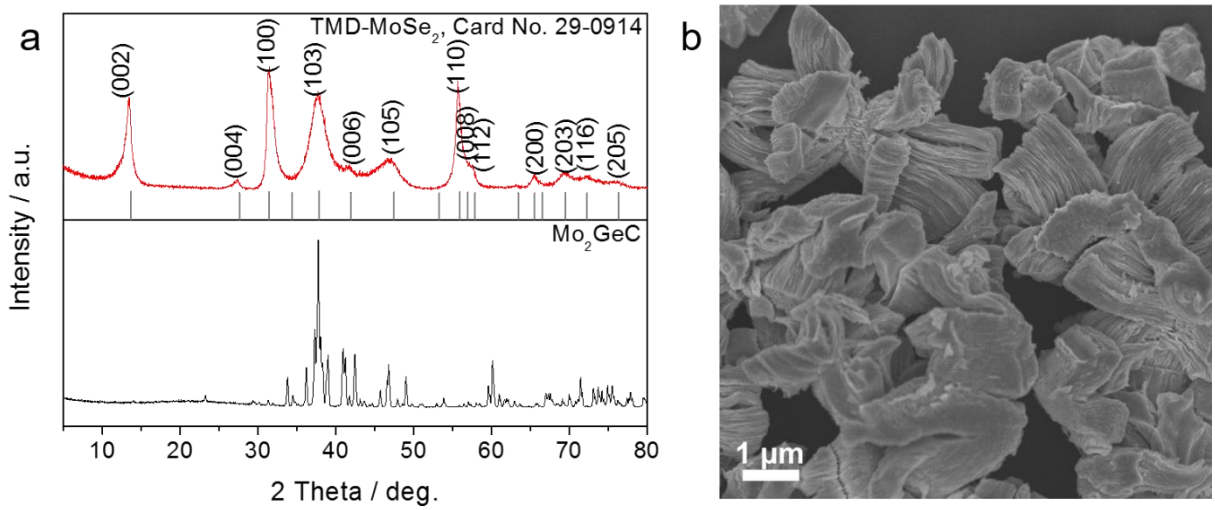

Fig. S7. Material characterization of $MoSe_2$ derived from engineering Mo_2GeC by Se vapour at 1073 K. a, XRD patterns of resultant $MoSe_2$ and Mo_2GeC. **b**, SEM image of resultant $MoSe_2$.

In Fig. S7a, a series of diffraction peaks at 13.7°, 31.4°, 37.9° and 55.9° are visible in the XRD patterns of the resultant $MoSe_2$, indexed to (002), (100), (103) and (110) facets of hexagonal $MoSe_2$ (JCPDS Card No. 29-0914), respectively. Moreover, there is no any peak of raw material Mo_2GeC, demonstrating the successful conversion and complete removal of Ge-layers from MAX-Mo_2GeC during our synthetic process. The SEM image of the resultant $MoSe_2$ (Fig. S7b) shows numerous nano-accordions with expanded structure.

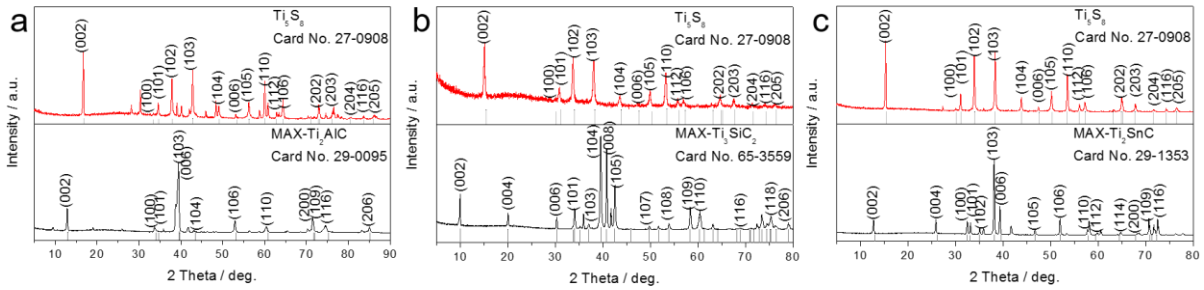

Fig. S8. Structural characterization of Ti_5S_8 derived from engineering Ti_2AlC, Ti_3SiC_2 and Ti_2SnC by H_2S gas. a-c, XRD patterns of (**a**) Ti_2AlC, (**b**) Ti_3SiC_2 and (**c**) Ti_2SnC and their corresponding derivatives Ti_5S_8.

After the reaction of MAX-Ti_2AlC, MAX-Ti_3SiC_2 and MAX-Ti_2SnC with H_2S gas at high temperatures of 1273, 1273 and 1173 K, respectively, Ti_5S_8 was obtained. In Fig. S8, there are five dominant peaks at 15.3°, 34.0°, 38.3°, 53.5° and 67.8° in the product derived from Ti_3SiC_2 (Fig. S8a), Ti_2AlC (Fig. S8b), Ti_2SnC (Fig. S8c), indexed to (002), (102), (103), (110) and (203) facets of Ti_5S_8 (JCPDS No. 27-0908), respectively. This demonstrates that Si-, Al- and Sn-containing MAX phases could be used as precursors to produce transition-metal chalcogenides by our conversion protocol.

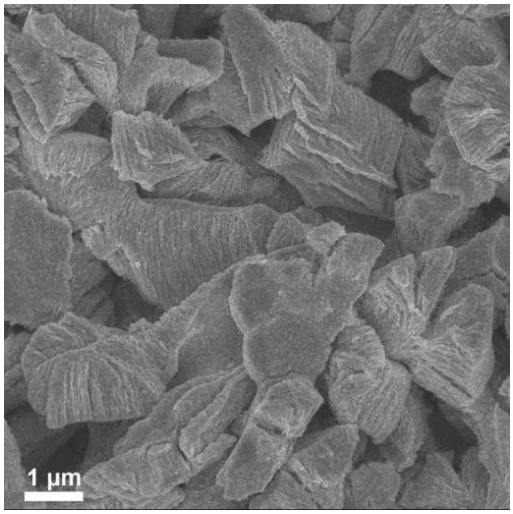

Fig. S9. Morphology characterization of the as-prepared accordion-like MoS_2 from engineering MAX-Mo_2GeC by H_2S gas at 1073 K. SEM image of the resultant MoS_2, showing numerous nano-accordions with expanded structure.

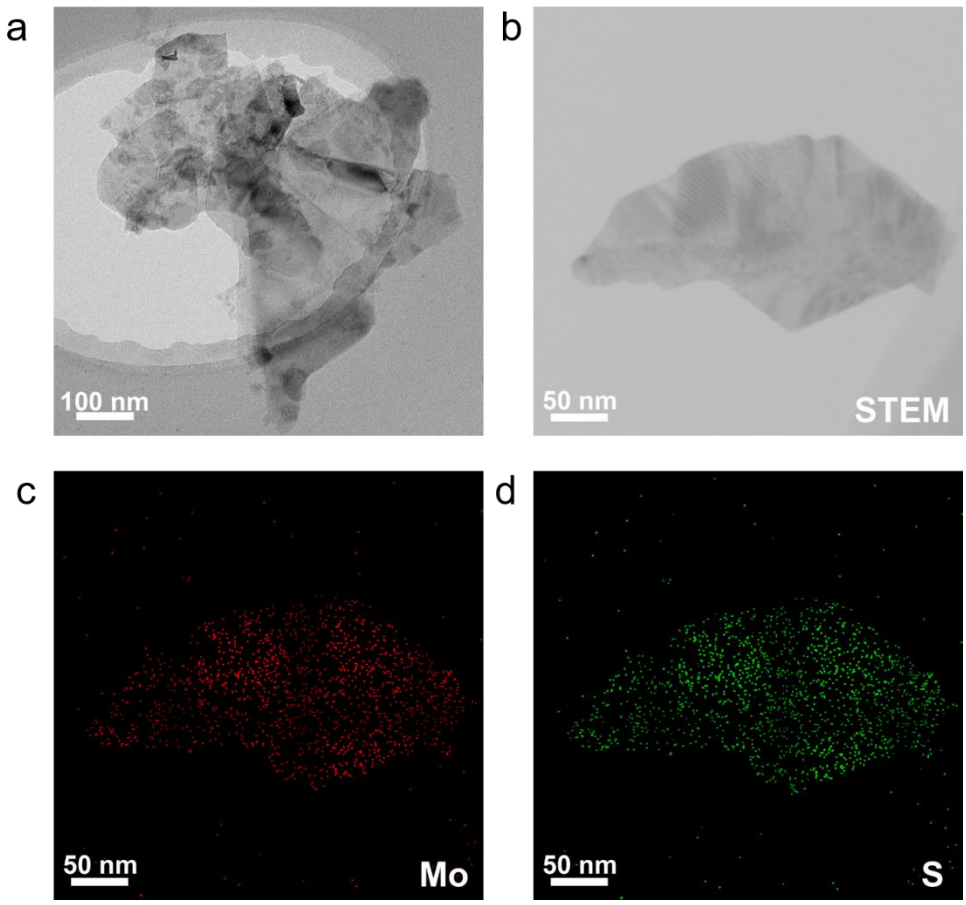

Fig. S10. Material characterization of 2H MoS_2 derived from engineering MAX-Mo_2GeC by H_2S gas at 1073 K. a, TEM image, **b-d**, STEM image (**b**) and the corresponding elemental mapping images of Mo (**c**), S (**d**) species.

After simple sonication of accordion-like MoS_2 in IPA solvents, a great deal of nanosheets could be exfoliated and directly used for the TEM test. As shown in Fig. S10a, some transparent nanosheets with lateral sizes of several hundreds of nanometers are visible. The STEM image (Fig. S10b) and elemental mapping images reveal the homogeneous distributions of Mo (Fig. S10c) and S (Fig. S10d) species in the nanosheets.

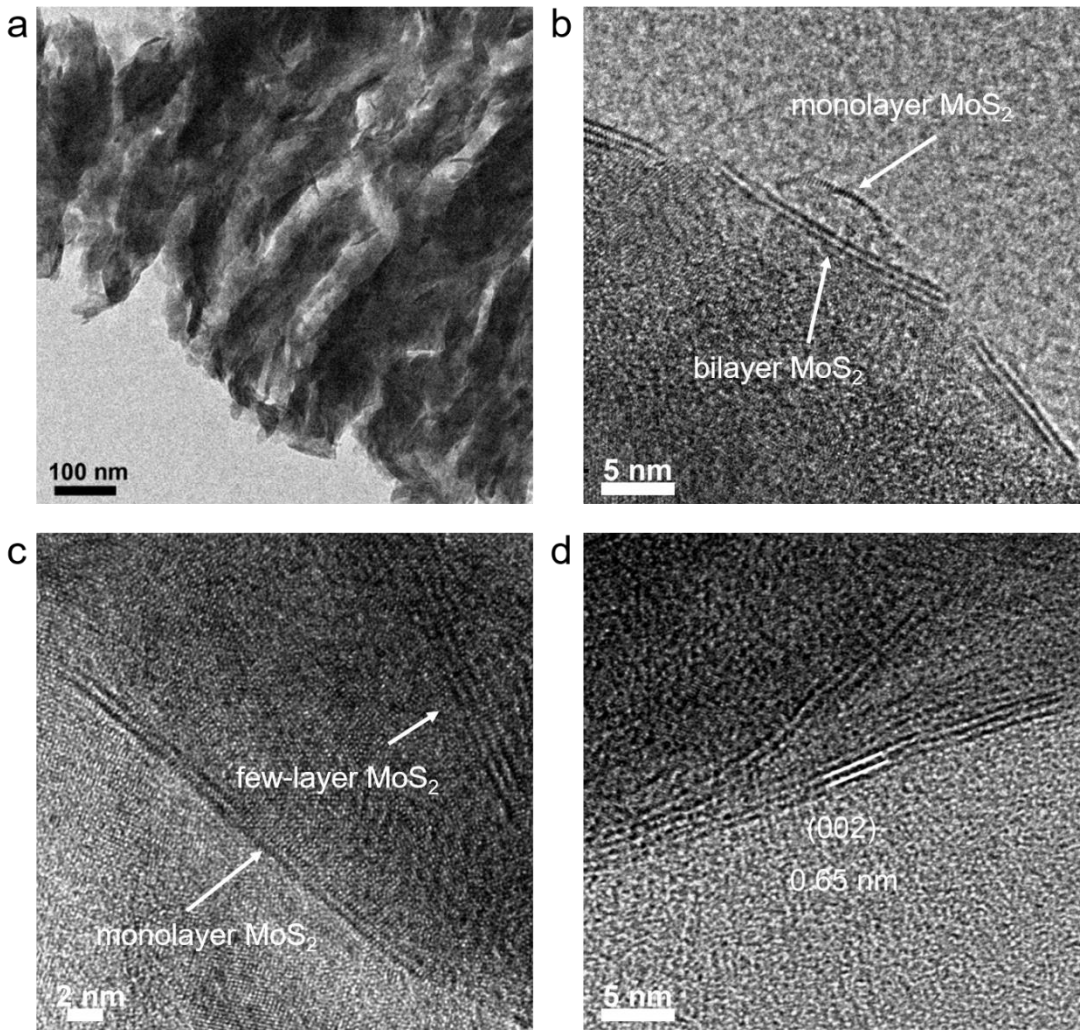

Fig. S11. The cross-sectional TEM and HRTEM images of 2H MoS_2 from engineering MAX-Mo_2GeC by H_2S gas at 1073 K. a, Cross-sectional TEM image of the resultant 2H MoS_2. **b-d**, Cross-sectional HRTEM images of the resultant 2H MoS_2.

To evaluate the interior structure of the accordion-like MoS_2, we conducted an ultrathin sectioning experiment. As shown in Fig. S11a, the cross-sectional TEM image shows the expanded structure, which is in good agreement with the SEM analysis of the resultant MoS_2 (Fig. 2c). Cross-sectional HRTEM images clearly exhibit the co-existence of monolayers (Figs. S11b and S11c), bilayers (Fig. S11b) and few layers (Figs. S11c and S11d) in the resultant MoS_2. In the few layers, the interlayer spacing is 0.65 nm, corresponding to the distance between the (002) facets of van der

Waals MoS_2 (ref. [13]), clearly demonstrating the conversion of non-van der Waals bulks to van der Waals transition-metal chalcogenides.

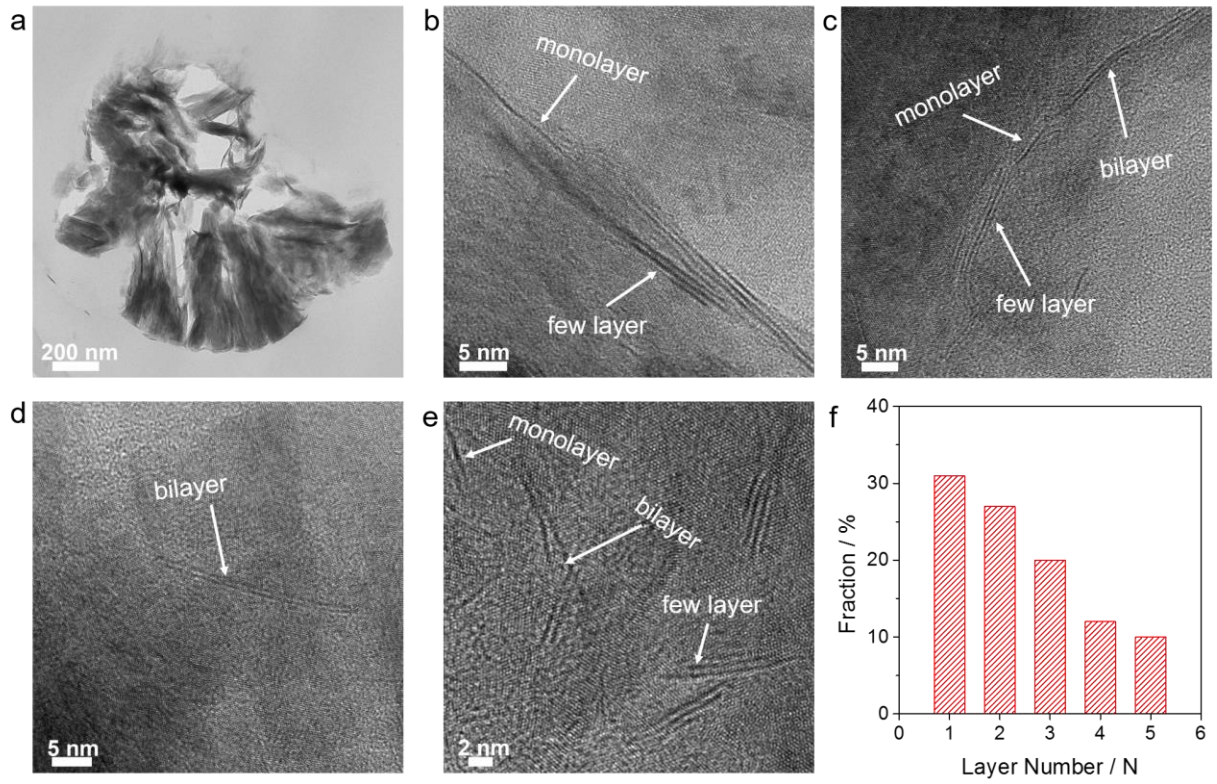

Fig. S12. Thickness analysis of highly expanded accordion-like MoS_2 synthesized from Mo_2GeC by our conversion reaction (fast quenching). a, Cross-sectional TEM image of highly expanded accordion-like MoS_2 produced by our topological conversion reaction associated with fast quenching. **b**-**e**, Cross-sectional HRTEM images, and **f**, statistical analysis of MoS_2 nanosheets based on the thickness.

By engineering MAX-Mo_2GeC with H_2S gas at 1073 K and then rapidly transferring the sample to a low temperature (room temperature) zone, highly expanded accordion-like MoS_2 was generated, as shown in the cross-sectional TEM image (Fig. S12a). Cross-sectional HRTEM images of highly expanded accordion-like MoS_2 (Fig. S12b-e) disclose that there are many monolayer, bilayer and few-layer MoS_2 in the sample. Thickness statistical analysis (Fig. S12f) demonstrates that the fraction of monolayer MoS_2 is 31%, which is much higher than that from the accordion-like MoS_2 produced via the standard conversion procedures (9%, Fig. S16c).

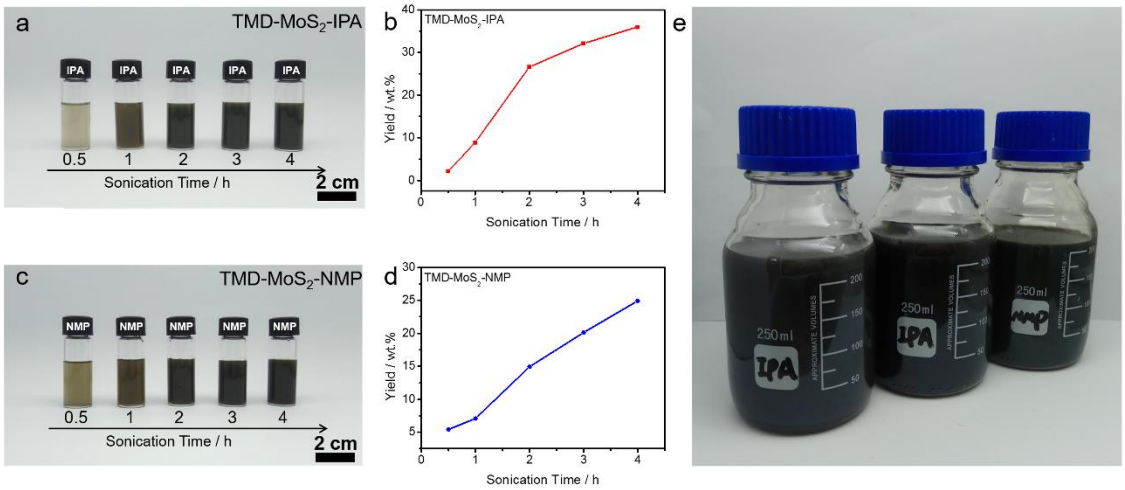

Fig. S13. Liquid-phase exfoliation of accordion-like MoS_2 in IPA and NMP solvents. a, **c**. Photographs of the supernatants of MoS_2 nanosheets exfoliated from accordion-like MoS_2 in IPA (**a**) and NMP (**c**) solvents with different sonication times from 0.5 to 4 h, showing that the colors of the supernatants become darker as increasing the sonication time. **b**, **d**. The production yields of MoS_2 nanosheets exfoliated in IPA (**b**) and NMP (**d**) solvents plotted as a function of sonication time. In the range of our study, the maximum production yields of exfoliated MoS_2 nanosheets from accordion-like MoS_2 in IPA (Fig. S13b) and NMP (Fig. S13d) solvents were 36.0 and 24.9 wt.%, respectively, much higher than those reported for exfoliated MoS_2 from bulk counterparts (0.6-4 wt.%)[6,14]. **e**, Photographs of high-throughput MoS_2 nanosheets exfoliated from accordion-like MoS_2 in IPA and NMP.

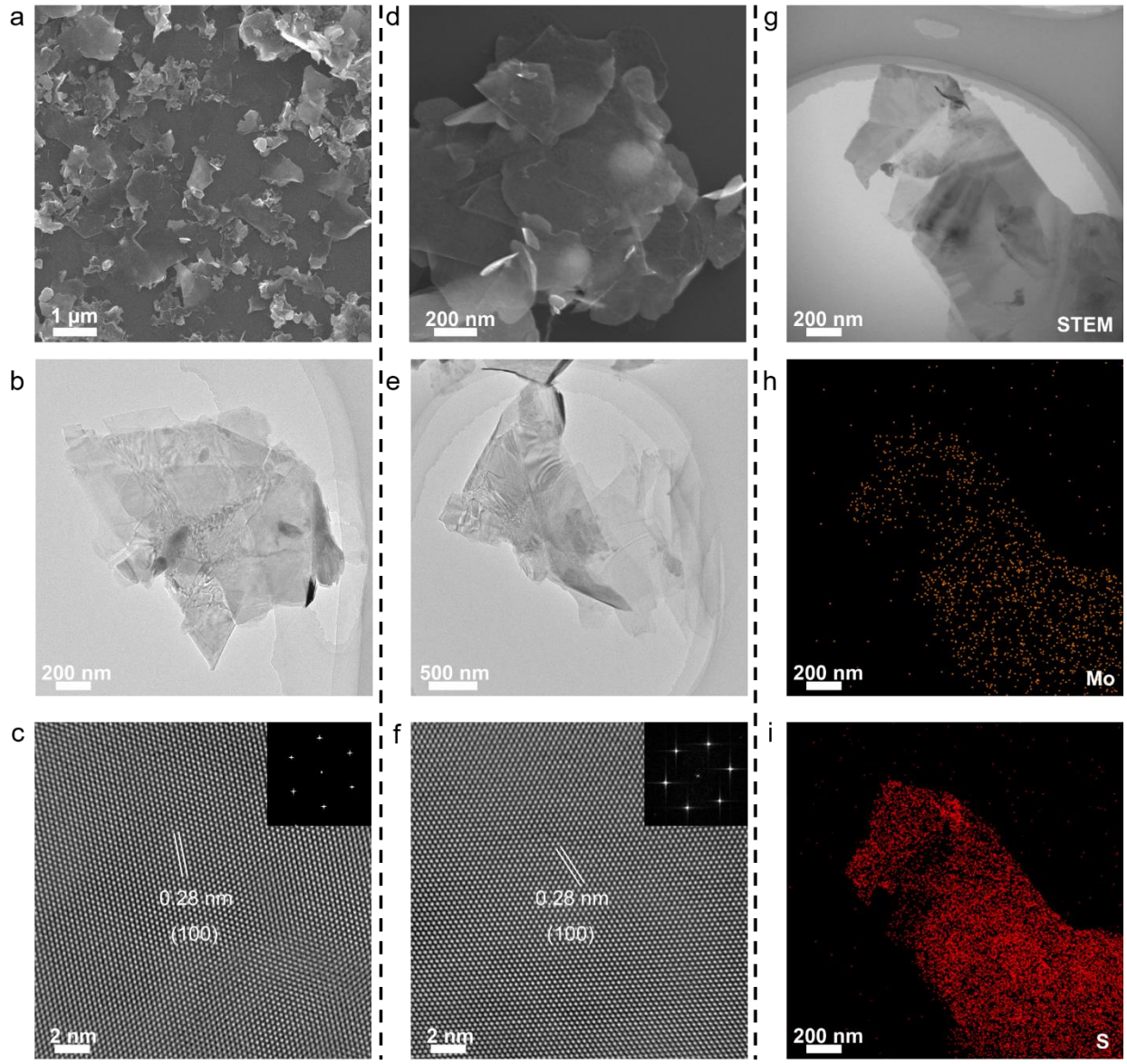

Fig. S14. Material characterization of exfoliated MoS_2 nanosheets from accordion-like MoS_2. **a**-**c**, SEM (**a**), TEM (**b**) and HRTEM (**c**) images of the exfoliated MoS_2 in IPA solvent. **c**-**e**, SEM (**c**), TEM (**d**) and HRTEM (**e**) images of the exfoliated MoS_2 in NMP solvents. **g**-**i**, STEM image (**g**), Mo (**h**) and S (**i**) elemental mapping images of exfoliated MoS_2 nanosheets. Insets in (**c**) and (**f**), the fast Fourier transform images of the corresponding HRTEM images.

To evaluate the free-standing MoS_2 nanosheets exfoliated from accordion-like MoS_2, scanning electron microscopy and transmission electron microscopy measurements were conducted. In Figs.

S14a and S14d, some transparent and wrinkled 2D nanosheets are observed, suggesting the thin feature. TEM images (Figs. 14b and 14e) further reveal free-standing 2D transparent nanosheets under the electron beam, in good agreement with the observation from SEM images. HRTEM images (Figs. S14c and S14f) disclose the regular atomic arrangement in the hexagonal system and the hexagonal diffraction spots (insets), which clearly demonstrates the high crystallinity of the resultant MoS_2 nanosheets. And a well-defined lattice distance of 0.28 nm is visible, indexed to the interplanar spacing between the (100) facets of 2H MoS_2. STEM image (Fig. S14g) and elemental mapping images reveal the homogeneous distributions of Mo (Fig. S14h) and S (Fig. S14i) species in the exfoliated MoS_2 nanosheets.

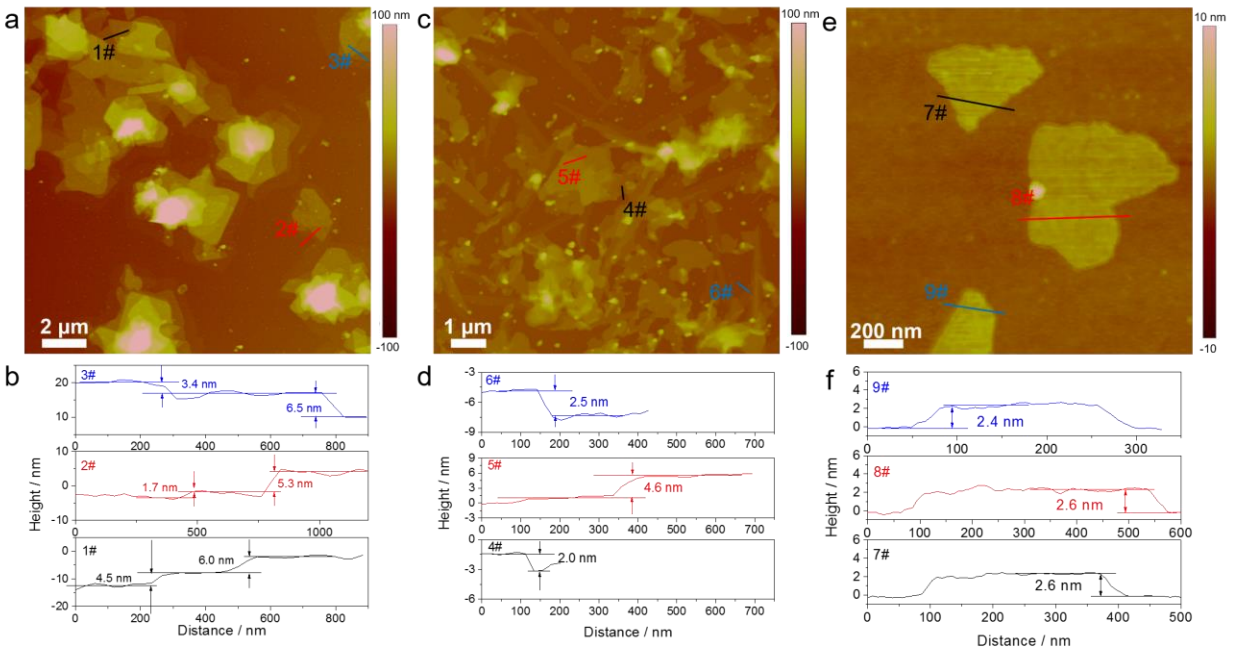

Fig. S15. Thickness analysis of MoS_2 nanosheets exfoliated from accordion-like MoS_2. a, AFM image of exfoliated MoS_2 nanosheets in IPA, and **b**, the corresponding thickness analysis. **c**, **e**. AFM images of exfoliated MoS_2 nanosheets in NMP, and **d**, **f**. the corresponding thickness analysis. Notably, the thin MoS_2 nanosheets without functional terminations tend to restack owing to their van der Waals force.

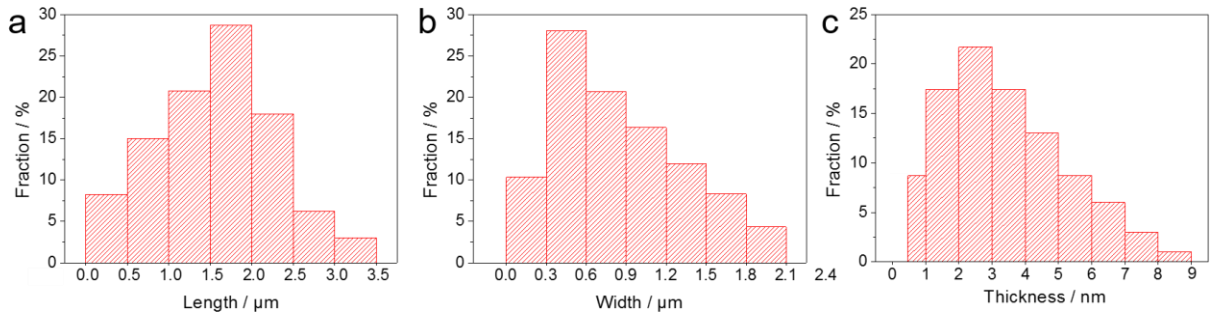

Fig. S16. Statistical analysis of MoS_2 nanosheets in accordion-like MoS_2. Statistical analysis of MoS_2 nanosheets based on the length (**a**), width (**b**) and thickness (**c**) of these nanosheets. As shown in Figs. S16a and S16b, the lateral sizes of the exfoliated MoS_2 nanosheets are mainly 0.5-2.5 μm in length and 0.3-1.5 μm in width, which are well consistent with the observations from SEM (Figs. S14a and S14d), TEM (Figs. S14b and S14e) and AFM (Fig. S15). Moreover, the thicknesses for the MoS_2 nanosheets are mainly 0.5-8 nm (Fig. S16c).

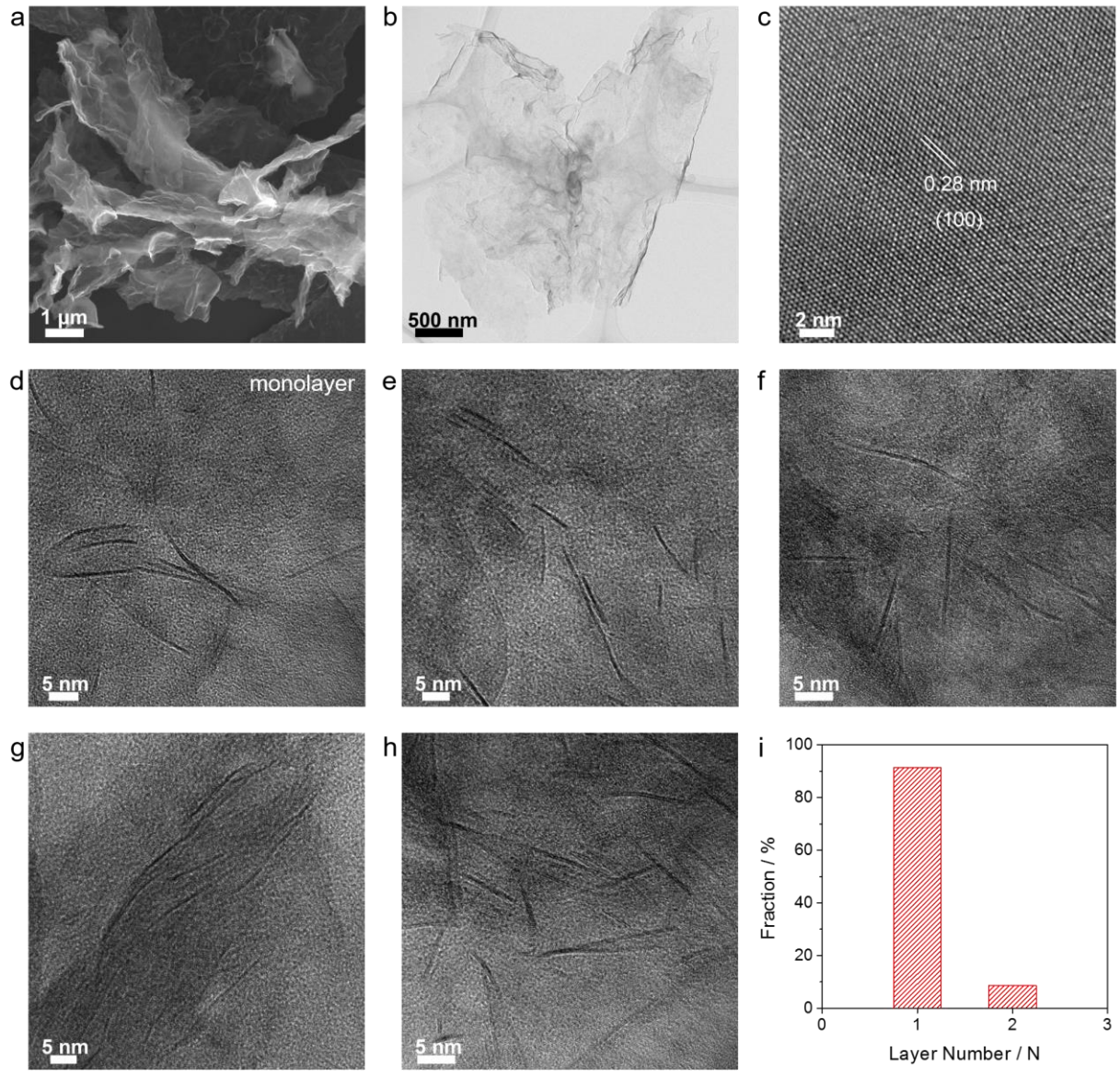

Fig. S17. Material characterization of MoS_2 nanosheets from engineering Mo_2CT_x in H_2S gas. **a-c**, SEM (**a**), TEM (**b**) and HRTEM (**c**) images of MoS_2 nanosheets. **d-h**, Cross-sectional HRTEM images of MoS_2 nanosheets. **i**, Statistical analysis of MoS_2 nanosheets based on the thickness.

Thin non-van der Waals solid Mo_2CT_x was used as a starting precursor to react with H_2S gas to synthesize van der Waals MoS_2. After the topological conversion reaction, flexible and ultrathin MoS_2 nanosheets were generated, as confirmed by the SEM (Fig. S17a) and TEM (Fig. S17b) images. HRTEM image (Fig. S17c) of MoS_2 nanosheets discloses a well-defined lattice distance

of 0.28 nm, indexed to the interplanar spacing between the (100) facets of 2H MoS_2. Cross-sectional HRTEM images (Fig. S17d-h) disclose that almost all the MoS_2 nanosheets were monolayers. The fraction of monolayer MoS_2 is up to ~91% (Fig. S17i). To the best of our knowledge, this is the highest value reported for producing monolayer transition-metal dichalcogenides.

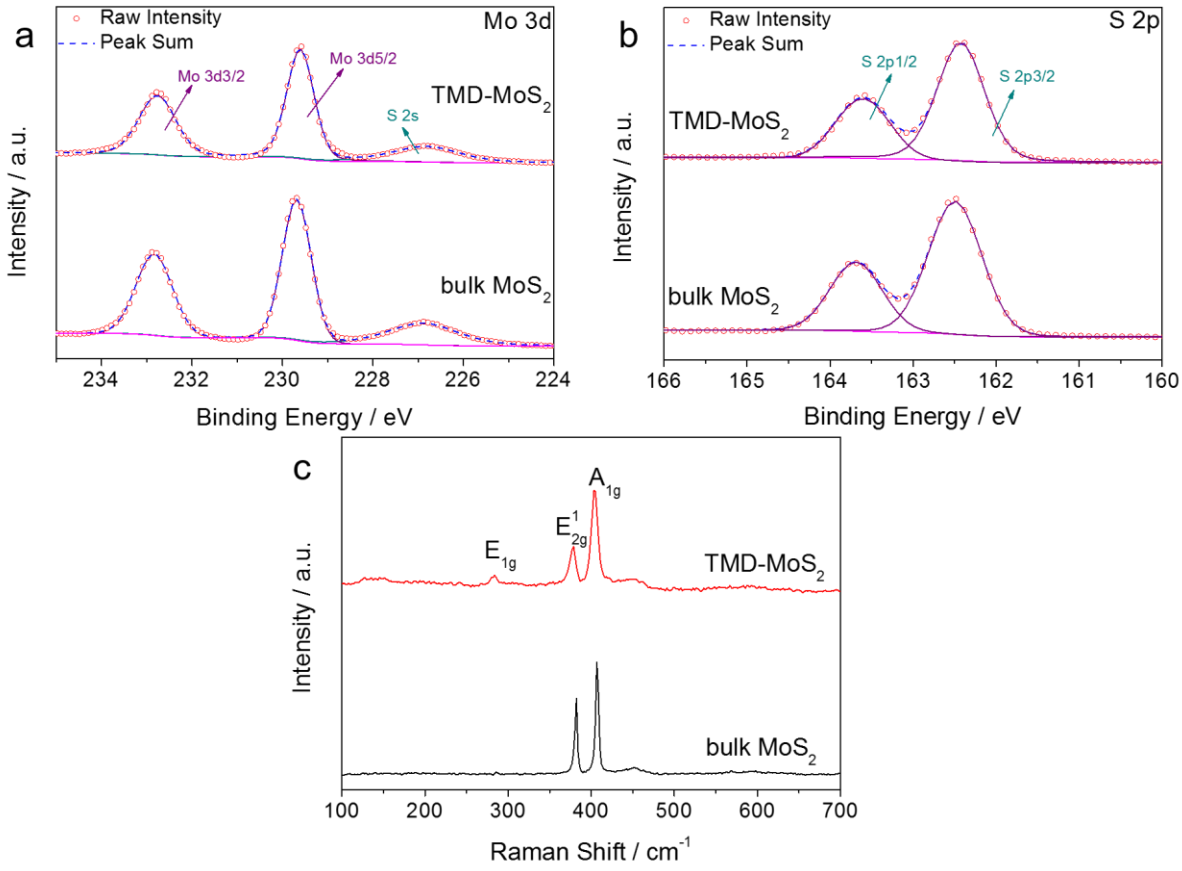

Fig. S18. Material characterization of accordion-like MoS_2 derived from engineering MAX-Mo_2GeC by H_2S gas at 1073 K. a, High-resolution Mo 3d XPS spectra, **b**, high-resolution S 2p XPS spectra, and **c**, Raman spectra of accordion-like MoS_2 and bulk 2H MoS_2.

To further identify the composition of the accordion-like MoS_2, X-ray photoelectron spectroscopy measurement was conducted. High-resolution Mo 3d XPS spectra of the accordion-like MoS_2 (Fig. S18a) could be fitted into two peaks at 229.6 and 232.8 eV, corresponding to Mo 3d5/2 and Mo 3d3/2 for Mo-S bonds, respectively, which are in good agreement with those of bulk 2H MoS_2. In addition, the peak at 226.8 eV is assigned to S 2s (ref. [13]). High-resolution S 2p XPS spectra (Fig. S18b) could be deconvoluted to one doublet at 162.4 and 163.6 eV, indexed to S 2p3/2 and S 2p1/2 signals of S-Mo bonds in the resultant MoS_2, respectively. Raman spectra of the resultant

MoS_2 (Fig. S18c) reveal two dominant peaks at 379 and 405 cm^{-1}, corresponding to in-plane $E_{2g}{}^1$ and out-of-plane A_{1g} vibrational modes of 2H MoS_2 (ref. [13]), respectively. Notably, one weak peak at 283 cm^{-1} is also identified, indexed to the E_{1g} peak of 2H MoS_2 (ref. [15]). This suggests there are some defects in the resultant MoS_2, owing to the relatively low conversion temperature (1073 K).

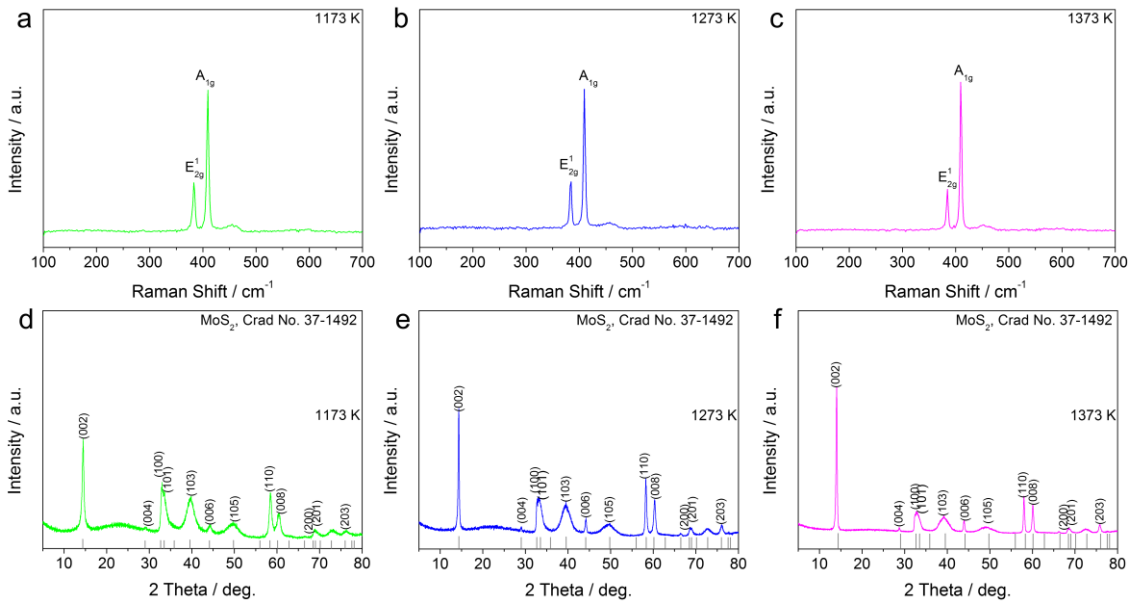

Fig. S19. Raman spectra and XRD patterns of accordion-like MoS_2 produced from MAX-Mo_2GeC at different temperatures (1173-1373 K). a-c, Raman spectra, and **d-f**, XRD patterns of accordion-like MoS_2 synthesized from Mo_2GeC at the temperatures of 1173-1373 K.

As shown in Figs. S19a-c, with increasing the reaction temperature from 1173 to 1373 K, the weak E_{1g} peak at 283 cm^{-1} in the Raman spectra was disappeared, and $E_{2g}{}^1$ (384 cm^{-1}) and A_{1g} (410 cm^{-1}) peaks become narrower, demonstrating the enhanced crystalline quality of resultant MoS_2. This could be further demonstrated by the XRD patterns as shown in Figs. S19d-f. Clearly, as increasing the reaction temperature from 1173 to 1373 K, all the diffraction peaks become more narrow and intense, instead of broad peaks of MoS_2 produced at a relatively low temperature of 1073 K (Fig. 2b).

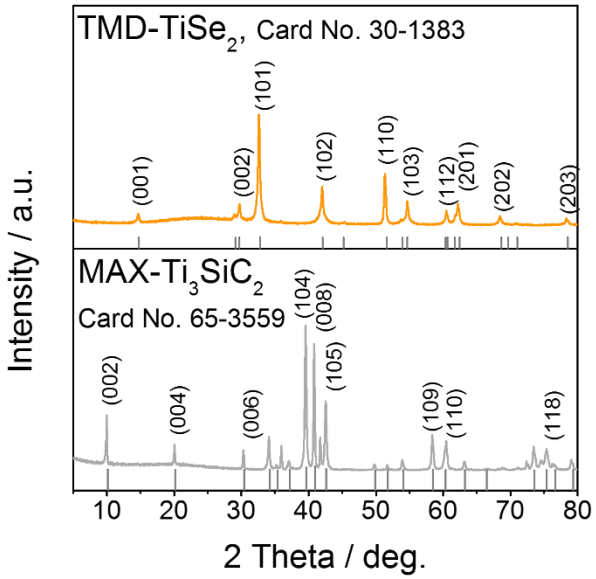

Fig. S20. XRD patterns of MAX-Ti_3SiC_2 and the resultant accordion-like $TiSe_2$ from engineering Ti_3SiC_2 by Se vapour at 1173 K. Different from the XRD patterns for MAX-Ti_3SiC_2, the XRD patterns of accordion-like $TiSe_2$ show a series of diffraction peaks at 29.7°, 32.8°, 42.1° and 51.6°, corresponding to (002), (101), (102) and (110) facets of hexagonal $TiSe_2$ (JCPDS No. 30-1383)[16], respectively, demonstrating the transformation of non-van der Waals Ti_3SiC_2 to van der Waals $TiSe_2$.

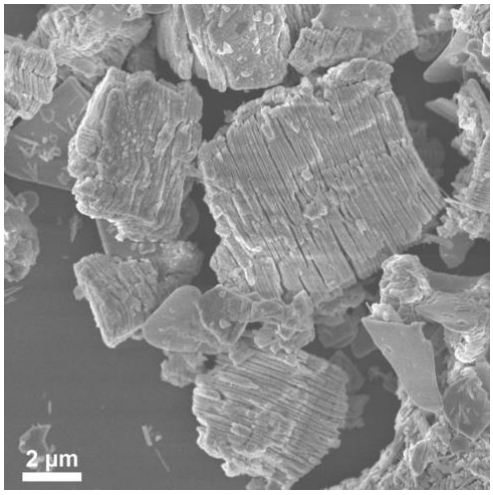

Fig. S21. SEM image of accordion-like $TiSe_2$ from engineering Ti_3SiC_2 by Se vapour at 1173 K. SEM image of the resultant $TiSe_2$, showing numerous nano-accordions with expanded interlayer spacing.

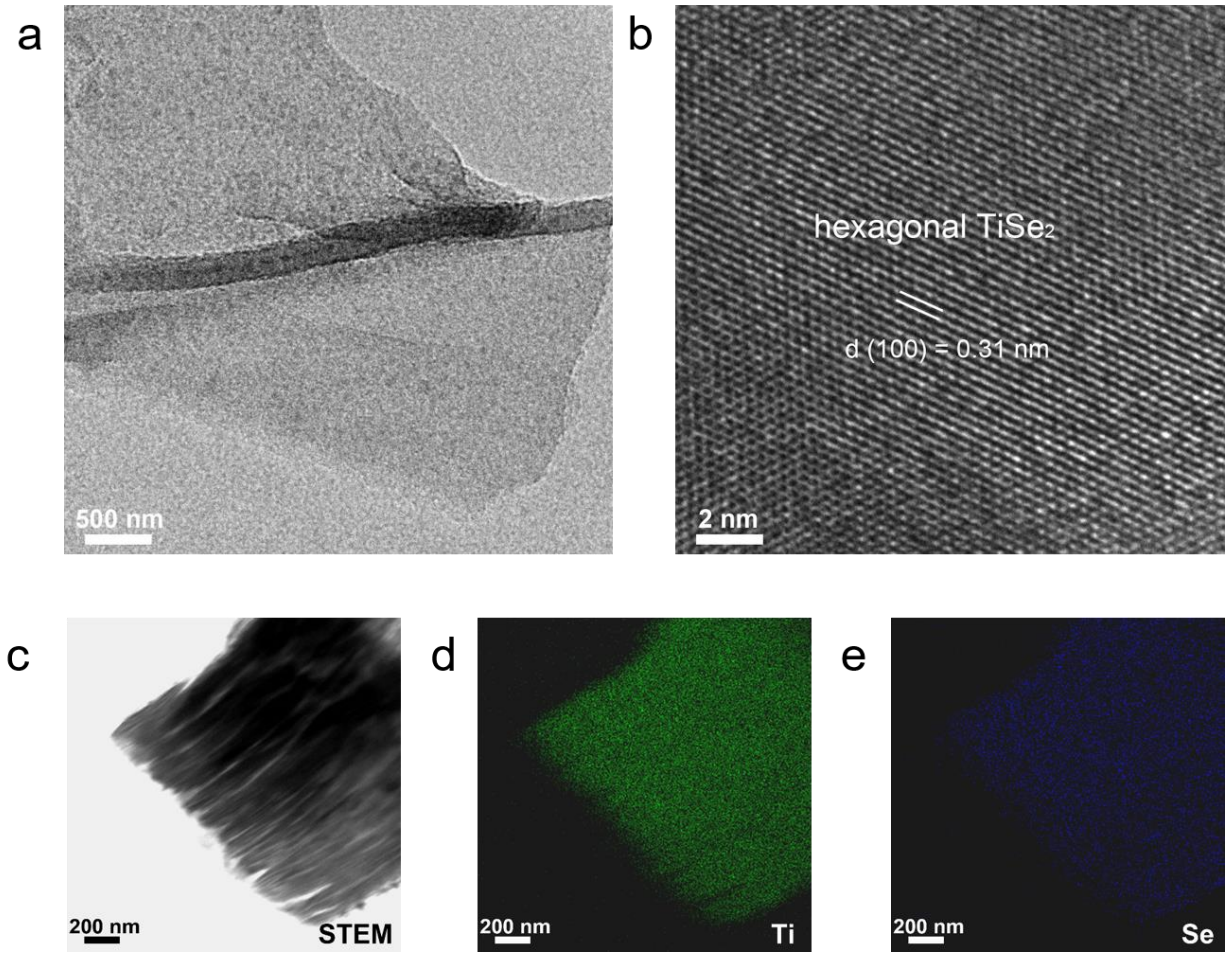

Fig. S22. Microstructure characterization of the resultant 1T $TiSe_2$ from engineering Ti_3SiC_2 by Se vapour at 1173 K. a, TEM image of the resultant $TiSe_2$ nanosheet exfoliated from accordion-like $TiSe_2$, exhibiting a transparent nanosheet under an electron beam. **b**, HRTEM image, manifesting a lattice spacing with 0.31 nm, indexed to the distance between the (100) facets of 1T $TiSe_2$ (ref. [17]). **c**-**e**, HAADF image (**c**), elemental mapping images, demonstrating the uniform distributions of Ti (**d**) and Se (**e**) elements.

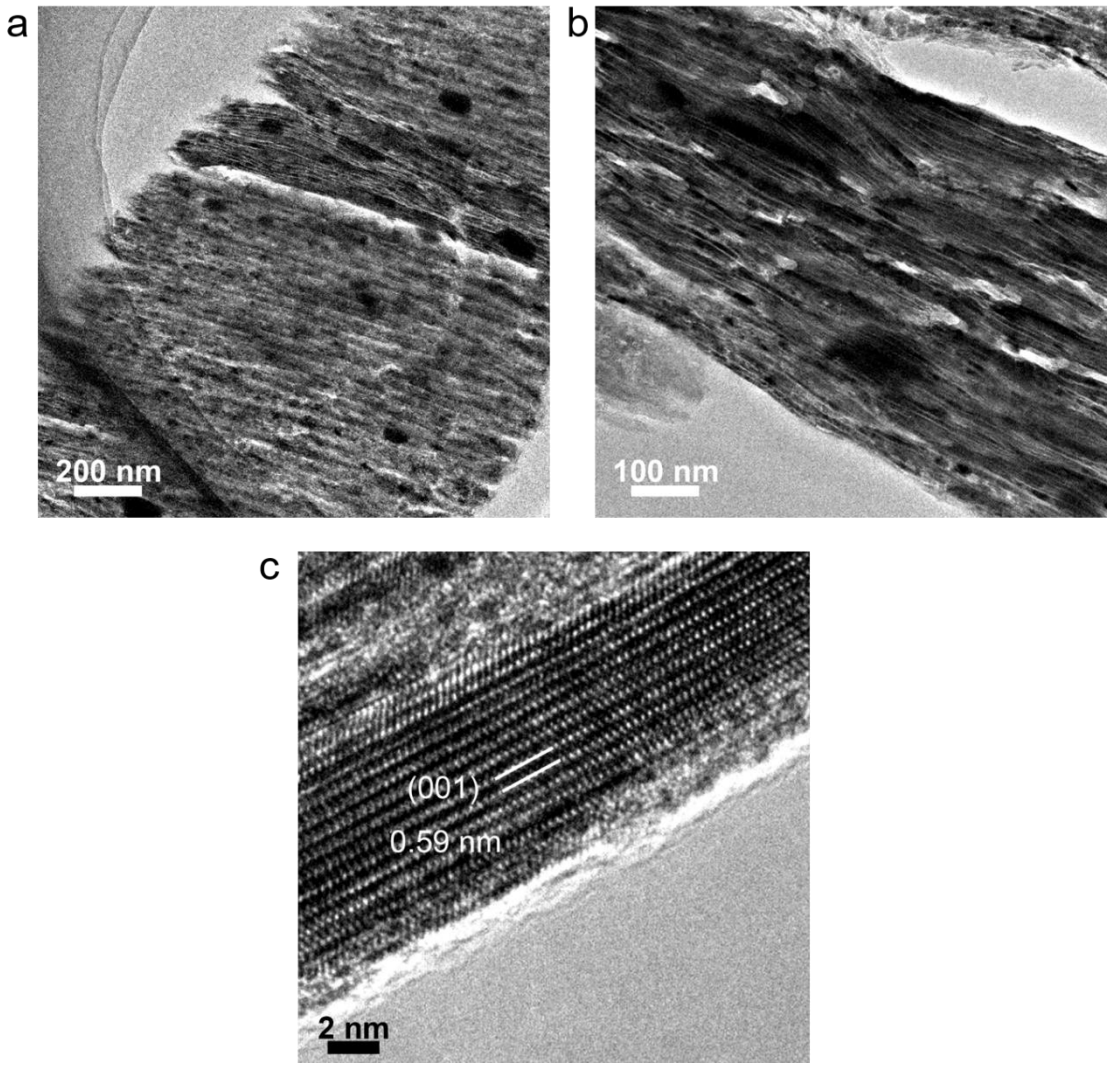

Fig. S23. Cross-sectional TEM and HRTEM images of accordion-like $TiSe_2$ from engineering Ti_3SiC_2 by Se vapour at 1173 K. a, b. Cross-Sectional TEM images, exhibiting the accordion-like structure. **c**, Cross-sectional HRTEM image, revealing the layered structure for van der Waals $TiSe_2$ and an interlayer spacing of 0.59 nm for the distance between the (001) facets of $TiSe_2$.

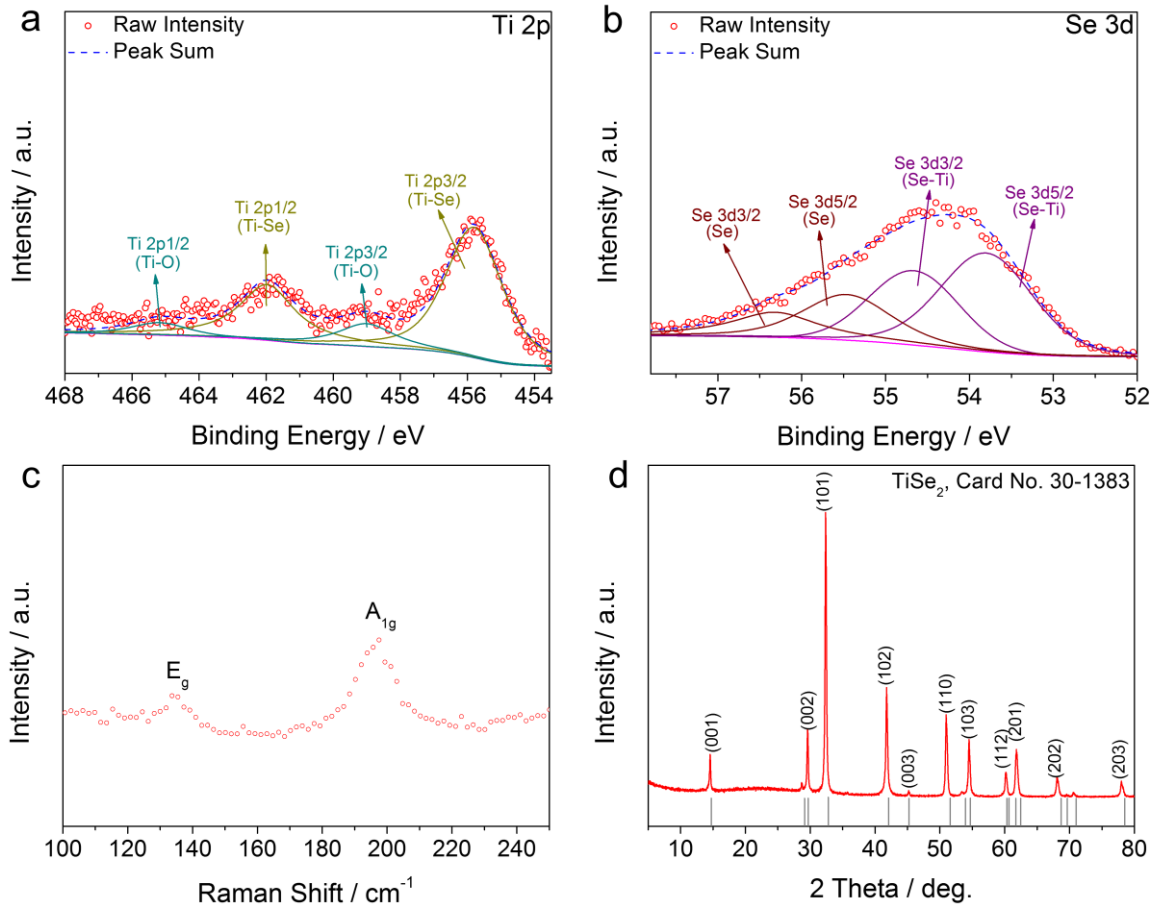

Fig. S24. Material characterization of accordion-like $TiSe_2$ from engineering Ti_3SiC_2 by Se vapour at 1273 K. a, High-resolution Ti 2p XPS spectra, **b**, high-resolution Se 3d XPS spectrum, **c**, Raman spectra, and **d**, XRD patterns of accordion-like $TiSe_2$.

By increasing the reaction temperature between Ti_3SiC_2 and Se vapour to 1273 K, accordion-like $TiSe_2$ could be obtained. To identify the composition of accordion-like $TiSe_2$, X-ray photoelectron spectroscopy measurement was conducted. As shown in Fig. S24a, high-resolution Ti 2p XPS spectra could be fitted into two doublets, in which one doublet shows the characteristic peaks for Ti-Se bonds at 455.8 and 461.9 eV, and the other doublet exhibits Ti 2p3/2 and Ti 2p1/2 peaks for Ti-O bonds at 459.0 and 465.2 eV, respectively. High-resolution Se 3d XPS spectrum (Fig. S24b) shows two peaks of Se-Ti bonds at 53.8 (Ti 2p3/2) and 54.7 (Ti 2p1/2) eV. In addition, there are two fitting peaks at 55.5 and 56.3 eV, corresponding to the Se 3d5/2 and Se 3d3/2 of elemental

selenium, respectively. Raman spectra (Fig. S24c) reveal two characteristic peaks at 136 and 198 cm^{-1} for the E_g and A_{1g} vibrational modes of 1T $TiSe_2$[17-21], respectively. The E_g mode corresponds to in-plane vibration of Se atoms, while the A_{1g} mode corresponds to out-of-plane vibration. According to the literature[16], the most stable form of $TiSe_2$ is 1T phase $TiSe_2$, consists of six Se atoms in octahedral coordination constituting a trigonal crystal structure. The crystal quality of $TiSe_2$ synthesized at 1273 K could be further confirmed by the sharp and intense diffraction peaks in Fig. S24d. There are a series of diffraction peaks at 29.7°, 32.8°, 42.1° and 51.6°, well indexed to the (002), (101), (102) and (110) facets of hexagonal $TiSe_2$ (JCPDS No. 30-1383)[17], respectively.

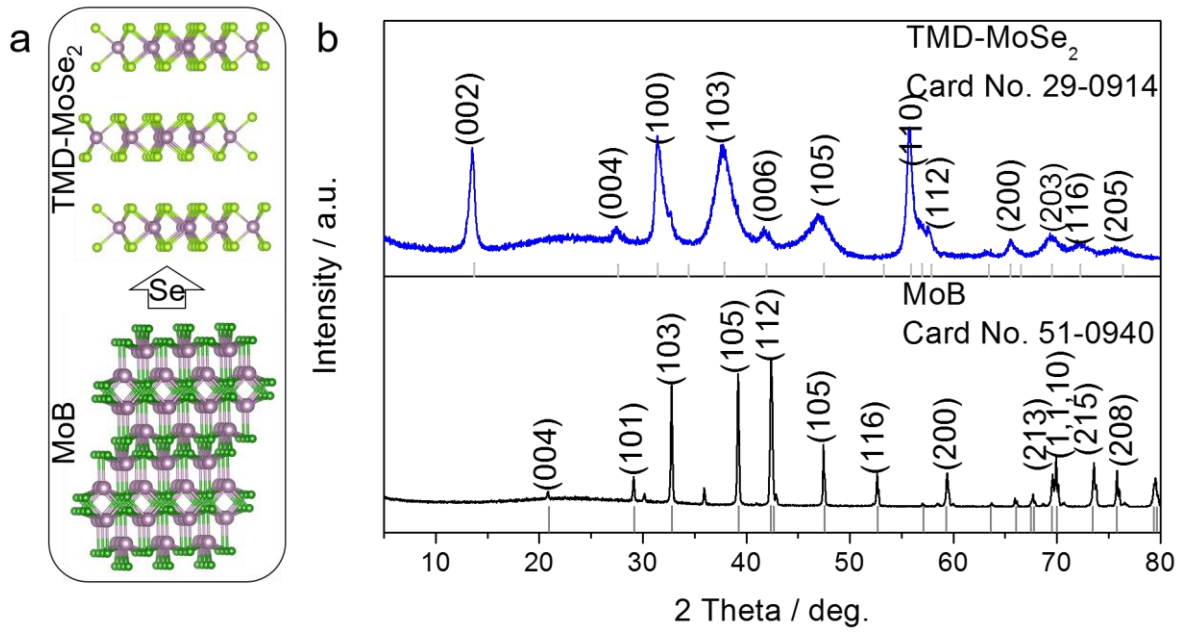

Fig. S25. Fabrication of 2H $MoSe_2$ by engineering non-van der Waals solid MoB with Se vapour at 1073 K. a, Schematic illustration of the transformation from non-van der Waals solid MoB to van der Waals $MoSe_2$. **b**, XRD patterns of the resultant $MoSe_2$ from MoB. As shown in Fig. S25b, a series of diffraction peaks at 13.7°, 31.4°, 37.9° and 55.9° can be identified, well indexed to (002), (100), (103) and (110) facets of hexagonal $MoSe_2$ (JCPDS Card No. 29-0914), respectively.

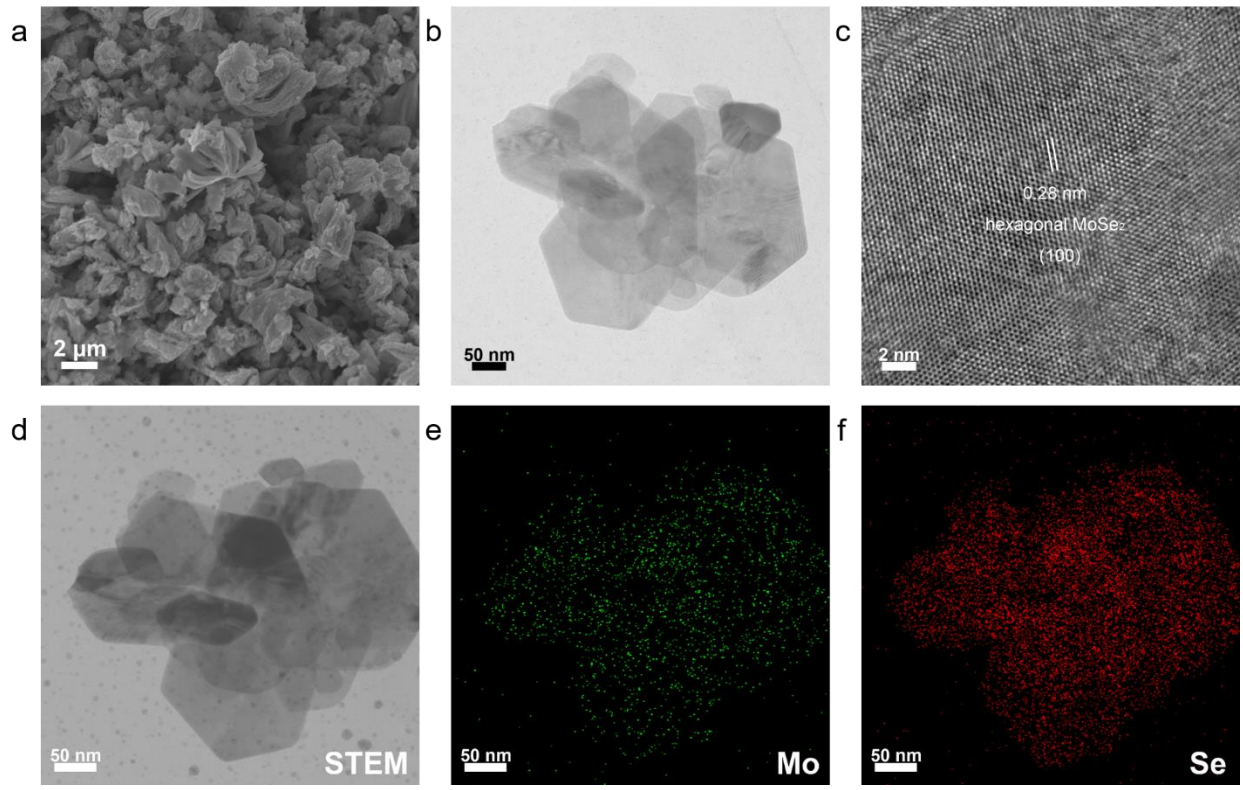

Fig. S26. Morphology and microstructure of 2H $MoSe_2$ by engineering non-van der Waals solid MoB with Se vapour at 1073 K. a, SEM image, showing the highly expanded structure for the resultant $MoSe_2$, which is dramatically different from that of solid MoB. **b**, TEM image of $MoSe_2$ layers exfoliated from the expanded $MoSe_2$, showing many transparent nanosheets with lateral sizes of several hundreds of nanometers, indicating the thin nature of $MoSe_2$ nanosheets. **c**, HRTEM image, disclosing clear lattice fringes with a distance of 0.28 nm, indexed well to the distance between the (100) facets of $MoSe_2$. **d-f**, STEM image (**d**), and elemental mapping images, demonstrating the uniform distributions of Mo (**e**) and Se (**f**) species in the nanosheets.

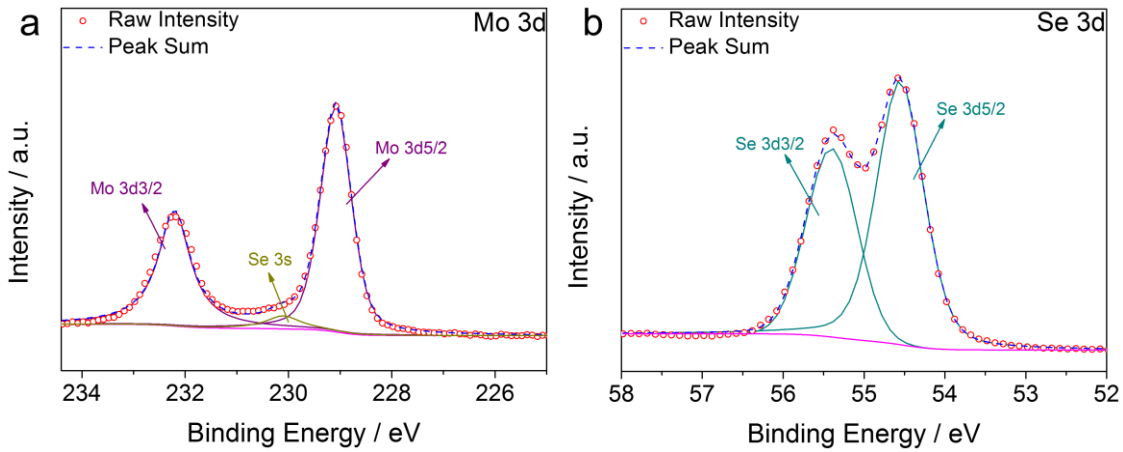

Fig. S27. XPS spectra of 2H $MoSe_2$ by engineering non-van der Waals solid MoB with Se vapour at 1073 K. a, High-resolution Mo 3d XPS spectra, **b**, high-resolution Se 3d XPS spectra of the resultant $MoSe_2$. As shown in Fig. S27a, high-resolution Mo 3d spectra could be deconvoluted into two peaks at 229.1 and 232.2 eV for Mo 3d5/2 and Mo 3d3/2, respectively, which are originated from Mo-Se bonds. In addition, the peak at 230.1 eV is indexed to Se 3s (ref. [22]). High-resolution Se 3d spectra (Fig. S27b) reveal two peaks at 54.6 and 55.4 eV, corresponding to the Se 3d5/2 and Se 3d3/2 of Se-Mo bonds, respectively.

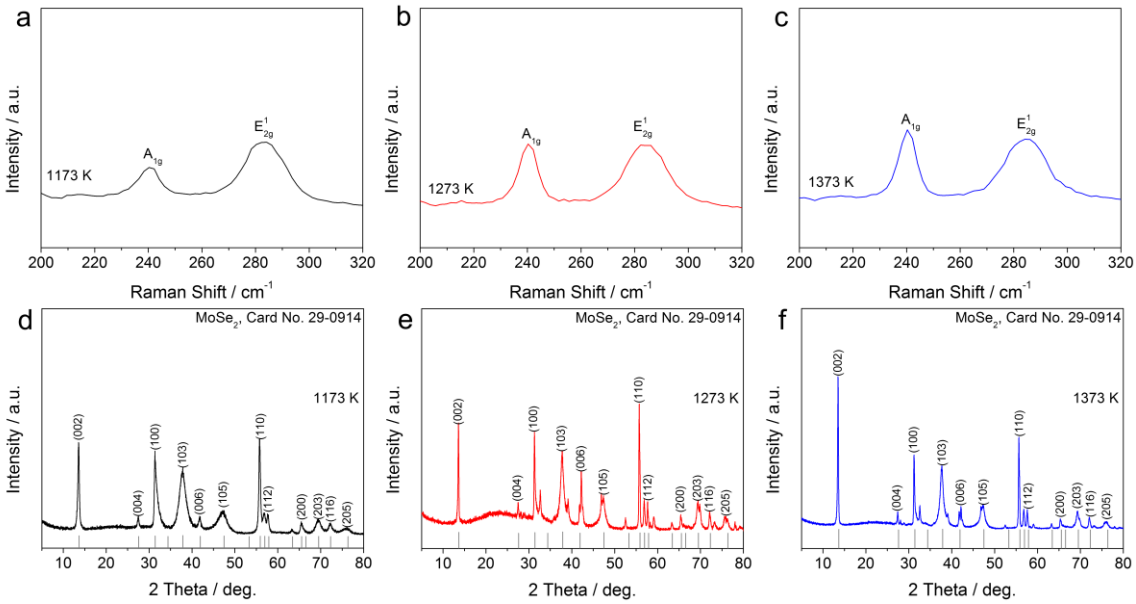

Fig. S28. Raman spectra and XRD patterns of 2H $MoSe_2$ produced from MoB at different temperatures from 1173 to 1373 K. a-c, Raman spectra, and **d-f**, XRD patterns of the resultant $MoSe_2$ derived from MoB at different temperatures from 1173 to 1373 K.

To evaluate the influence of the reaction temperature on the crystal quality of $MoSe_2$ produced from MoB, Raman and XRD measurements were carried out. As shown in Figs. S28a-c, with increasing the reaction temperature from 1173 to 1373 K, the characteristic peaks at 241 and 283 cm^{-1} for the out-of-plane A_{1g} and in-plane $E_{2g}{}^1$ vibrational modes of $MoSe_2$ (ref. [23]), respectively, are visible in the Raman spectra. In the XRD patterns (Figs. S28d-f), there are a series of diffraction peaks at 13.7°, 31.4°, 37.9° and 55.9°, indexed to (002), (100), (103) and (110) facets of hexagonal $MoSe_2$ (JCPDS Card No. 29-0914), respectively. Clearly, with increasing the reaction temperature from 1173 to 1373 K, all the diffraction peaks become more narrow and intense, instead of some broad peaks of $MoSe_2$ at a relatively low temperature of 1073 K (Fig. S25b).

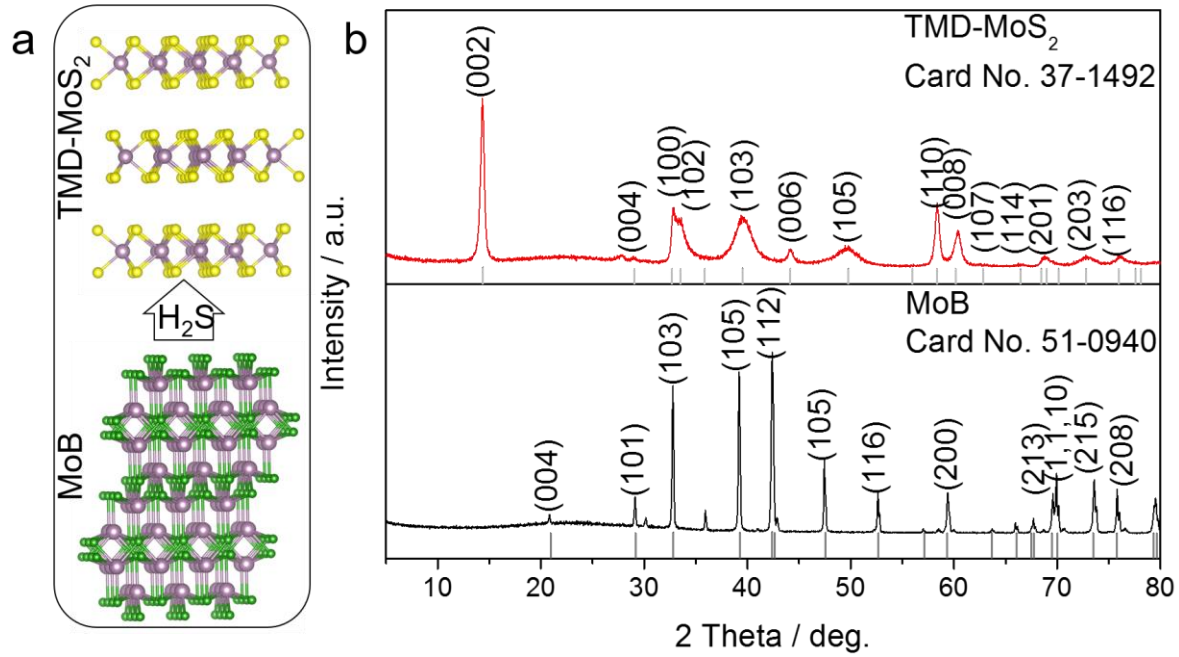

Fig. S29. Fabrication of 2H MoS_2 synthesized from engineering non-van der Waals solid MoB by H_2S at 1173 K. a, Schematic illustration of the transformation from non-van der Waals solid MoB to van der Waals MoS_2. **b**, XRD patterns of the resultant MoS_2 from MoB. As shown in Fig. S29b, a series of diffraction peaks at 14.1°, 32.7°, 39.5° and 58.3° can be identified, well indexed to (002), (100), (103) and (110) facets of hexagonal MoS_2 (JCPDS Card No. 37-1492), respectively.

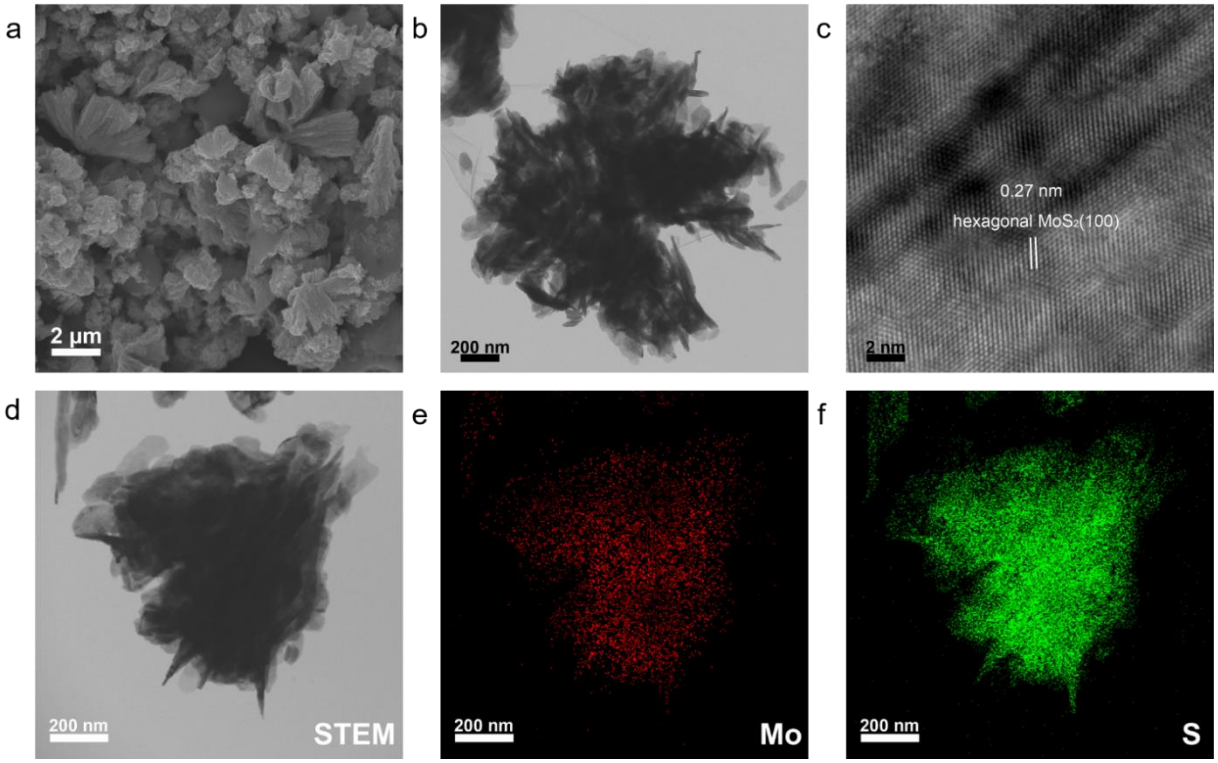

Fig. S30. Morphology and microstructure of 2H MoS_2 derived from engineering non-van der Waals solid MoB by H_2S at 1173 K. a, SEM image, exhibiting the highly expanded structure for the resultant MoS_2, which is dramatically different from that of solid MoB. **b**, TEM image of accordion-like MoS_2, showing that numerous MoS_2 nanosheets are interwoven together. **c**, HRTEM image, disclosing a lattice distance of 0.27 nm, indexed well to the distance between the (100) facets of 2H MoS_2. **d-f**, STEM image (**d**) and elemental mapping images, manifesting the uniform elemental distributions of Mo (**e**) and S (**f**) species.

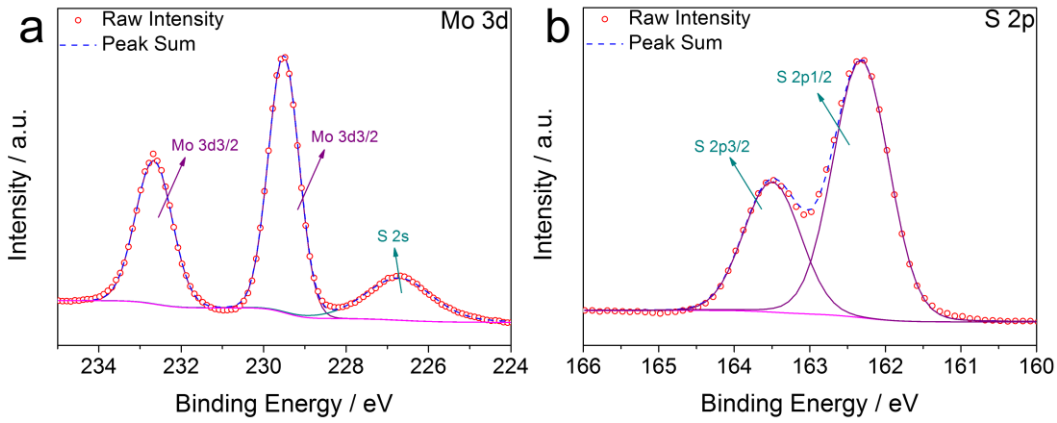

Fig. S31. XPS spectra of 2H MoS_2 derived from engineering non-van der Waals solid MoB by H_2S at 1173 K. a, High-resolution Mo 3d XPS spectra, **b**, high-resolution S 2p XPS spectra of the resultant MoS_2. As shown in Fig. S31a, high-resolution Mo 3d XPS spectra exhibit two peaks at 229.5 and 232.7 eV for Mo 3d5/2 and Mo 3d3/2 of Mo-S bonds, respectively, associated with one peak at 226.7 eV for S 2s (ref. [13]). High-resolution S 2p XPS spectra (Fig. S31b) could be deconvoluted into two peaks at 162.3 and 163.5 eV, corresponding to the S 2p3/2 and S 2p1/2 of S-Mo bonds, respectively.

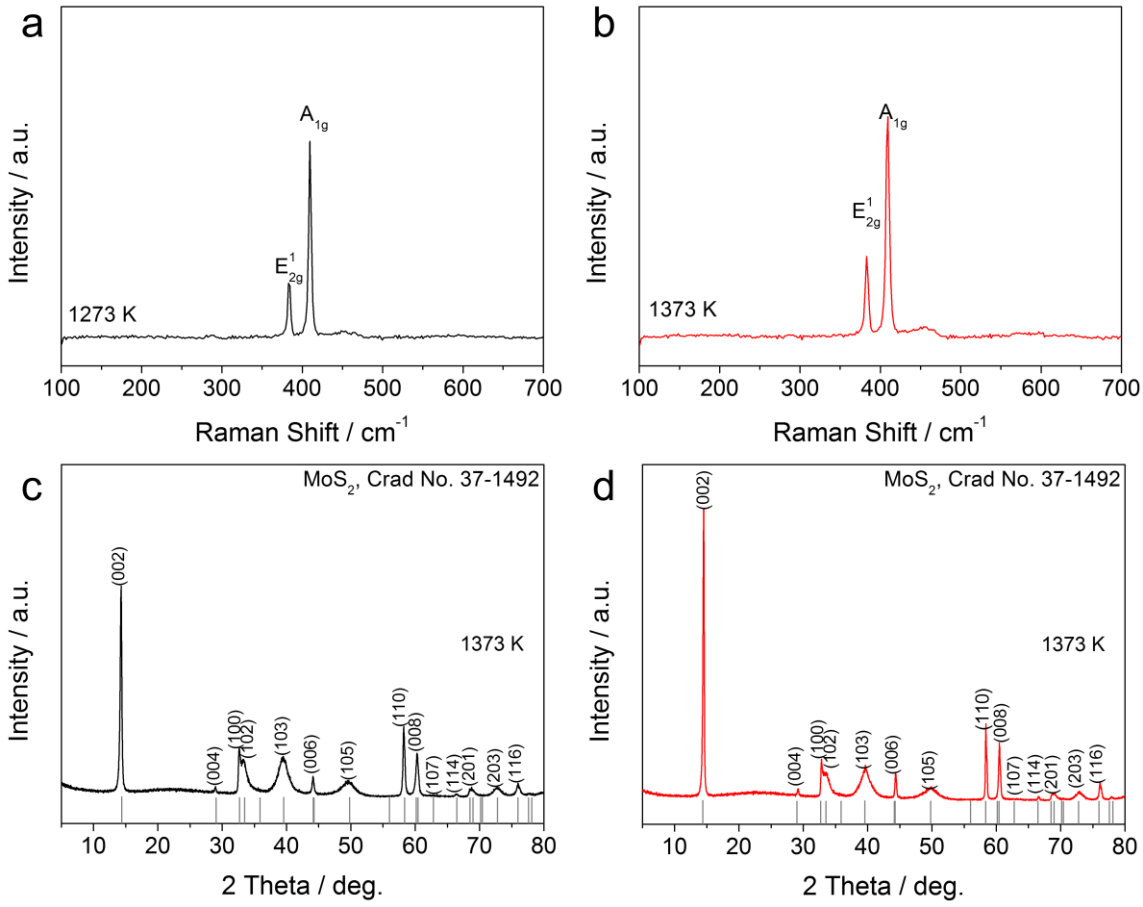

Fig. S32. Raman spectra and XRD patterns of 2H MoS_2 produced from MoB at the temperatures of 1273 and 1373 K. a, **b**. Raman spectra, and **c**, **d**. XRD patterns of the resultant MoS_2 derived from MoB at the temperatures of 1273 and 1373 K.

To evaluate the influence of the reaction temperature on the crystal quality of MoS_2 produced from MoB, Raman and XRD measurements were carried out. As shown in Figs. S32a and S32b, with increasing the reaction temperature to 1273 and 1373 K, the characteristic peaks at 385 and 410 cm^{-1} for the in-plane $E_{2g}{}^1$ and out-of-plane A_{1g} vibrational modes of MoS_2 become clear and narrow in the Raman spectra[13]. In the XRD patterns (Figs. S32c and S32d), a series of diffraction peaks at 14.1°, 32.7°, 39.5° and 58.3° can be identified, well indexed to (002), (100), (103) and (110) facets of hexagonal MoS_2 (JCPDS Card No. 37-1492), respectively. Clearly, with increasing the reaction temperature to 1273 and 1373 K, all the diffraction peaks become more narrow and

intense, instead of some broad peaks of $MoSe_2$ at a relatively low temperature of 1173 K (Fig. S29b).

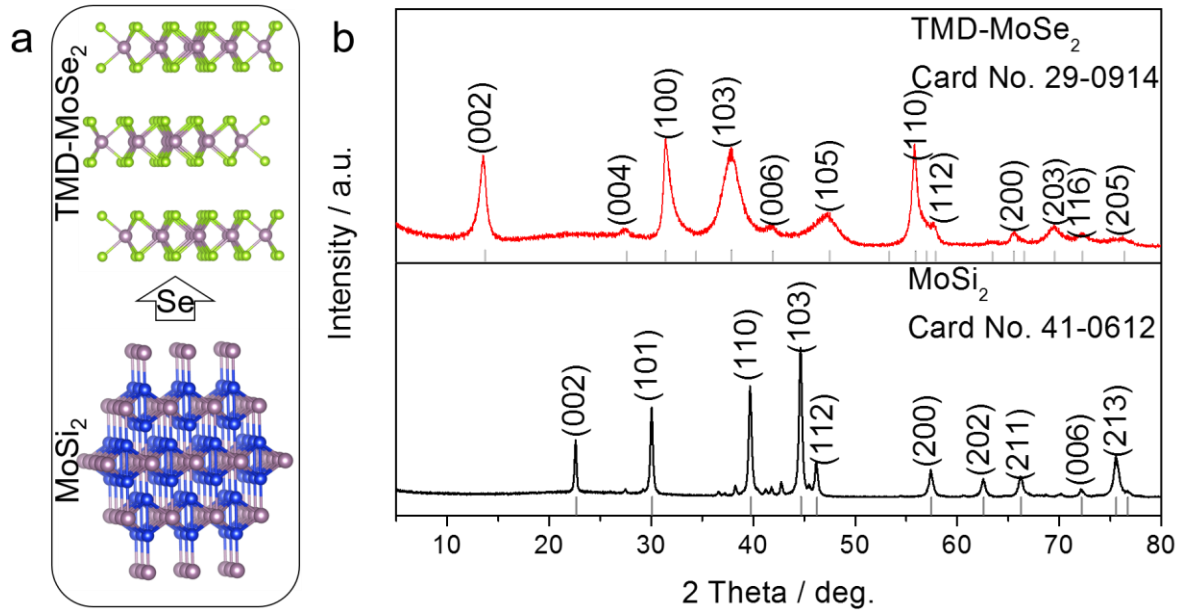

Fig. S33. Fabrication of 2H $MoSe_2$ by engineering non-van der Waals solid $MoSi_2$ under Se vapour at 1173 K. a, Schematic illustration of the transformation from non-van der Waals solid $MoSi_2$ to van der Waals $MoSe_2$. **b**, XRD patterns of the resultant $MoSe_2$ from $MoSi_2$. As shown in Fig. S33b, a series of diffraction peaks at 13.7°, 31.4°, 37.9° and 55.9° can be identified, well indexed to (002), (100), (103) and (110) facets of hexagonal $MoSe_2$ (JCPDS Card No. 29-0914), respectively.

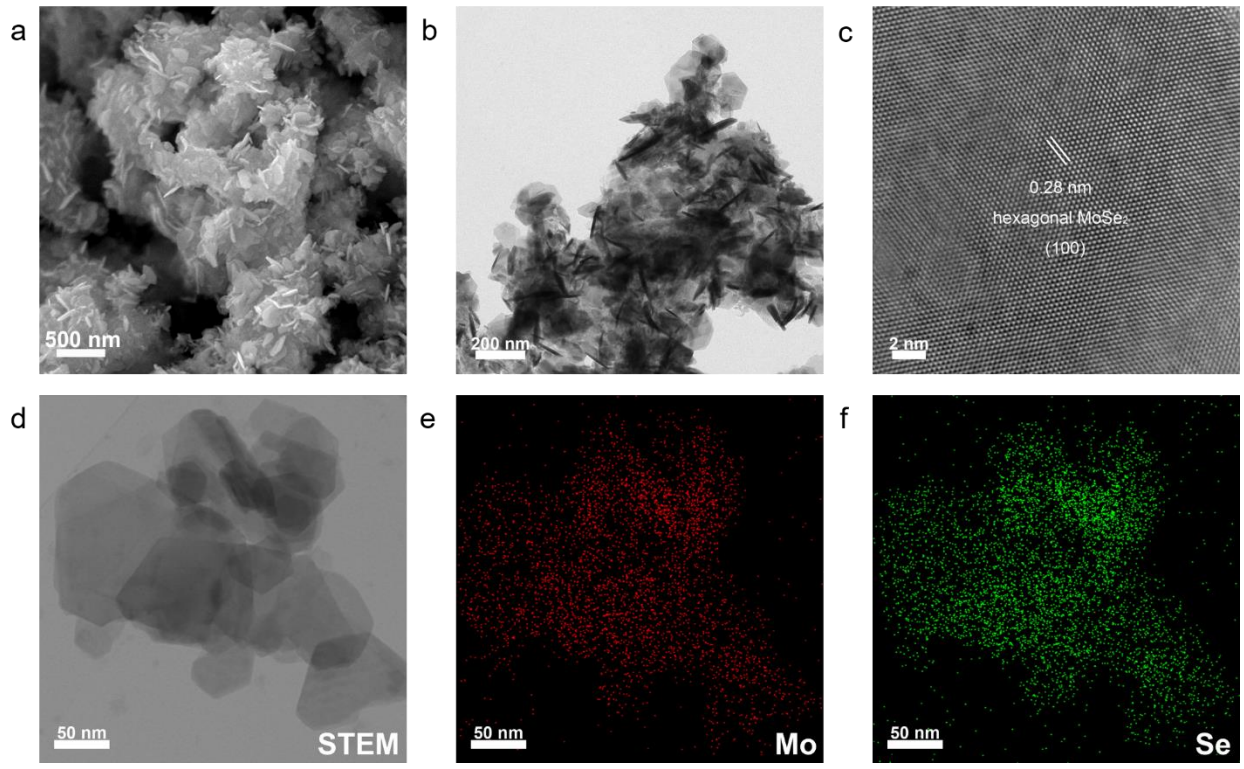

Fig. S34. Morphology and microstructure of 2H $MoSe_2$ by engineering non-van der Waals solid $MoSi_2$ with Se vapour at 1173 K. a, SEM image, showing the highly expanded structure for the resultant $MoSe_2$, which is dramatically different from that of solid $MoSi_2$. **b**, TEM image of the expanded $MoSe_2$, showing many transparent nanosheets, indicating the thin nature. **c**, HRTEM image, disclosing clear lattice fringes with a distance of 0.28 nm, indexed well to the distance between the (100) facets of $MoSe_2$. **d-f**, STEM image (**d**), and elemental mapping images, demonstrating the uniform distributions of Mo (**e**) and Se (**f**) species in the nanosheets.

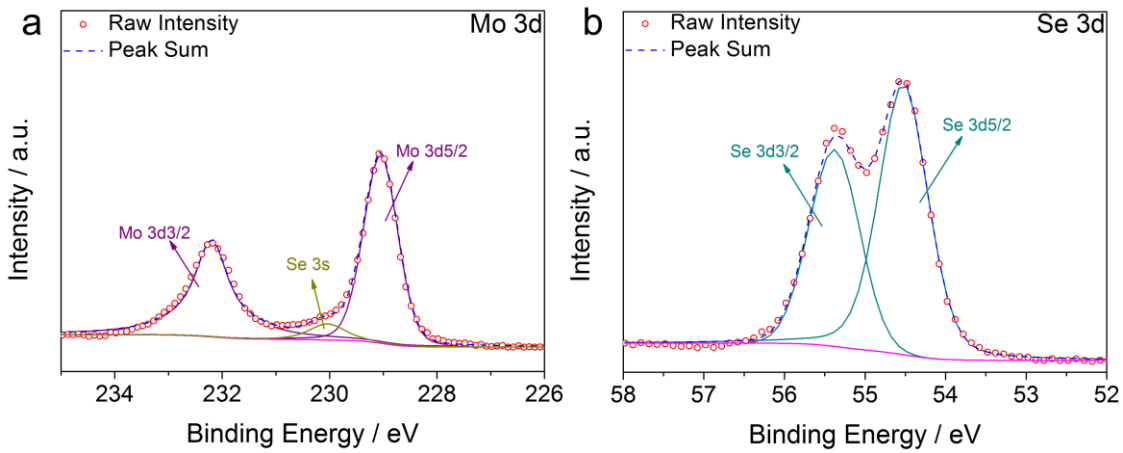

Fig. S35. XPS spectra of 2H $MoSe_2$ by engineering non-van der Waals solid $MoSi_2$ with Se vapour at 1173 K. a, High-resolution Mo 3d XPS spectra, **b**, high-resolution Se 3d XPS spectra of the resultant $MoSe_2$. As shown in Fig. S35a, high-resolution Mo 3d spectra could be deconvoluted into two peaks at 229.1 and 232.2 eV for Mo 3d5/2 and Mo 3d3/2, respectively, which are originated from Mo-Se bonds. In addition, the peak at 230.0 is indexed to the Se 3s (ref. [22]). High-resolution Se 3d spectra (Fig. S35b) reveal two peaks at 54.5 and 55.4 eV, corresponding to the Se 3d5/2 and Se 3d3/2 of Se-Mo bonds, respectively.

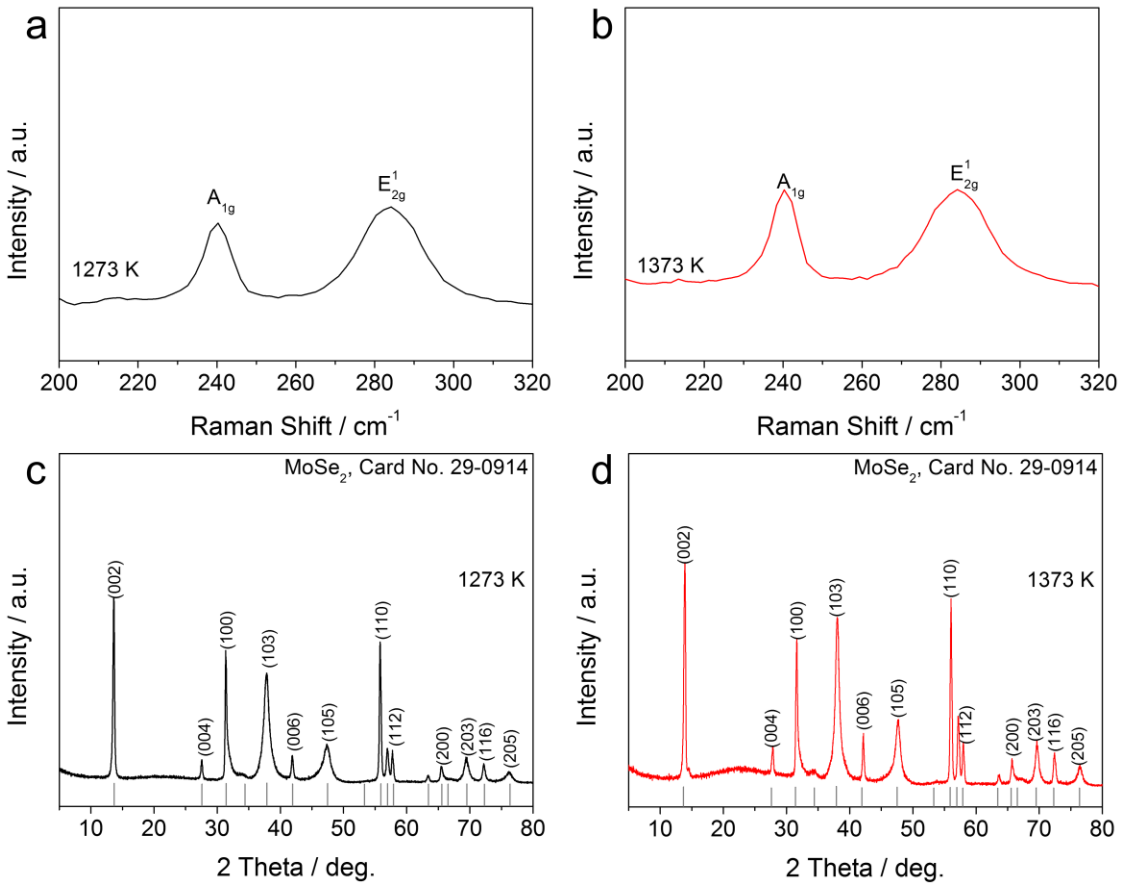

Fig. S36. Raman spectra and XRD patterns of 2H $MoSe_2$ produced from $MoSi_2$ at the temperatures of 1273 and 1373 K. a, **b**. Raman spectra, and **c**, **d**. XRD patterns for the resultant $MoSe_2$ derived from $MoSi_2$ at the temperatures of 1273 and 1373 K.

To evaluate the influence of the reaction temperature on the crystal quality of $MoSe_2$ produced from $MoSi_2$, Raman and XRD measurements were carried out. As shown in Figs. S36a and S36b, with increasing the reaction temperature to 1273 and 1373 K, the characteristic peaks at 241 and 283 cm^{-1} for the out-of-plane A_{1g} and in-plane $E_{2g}{}^1$ vibrational modes of $MoSe_2$ (ref. [23]), respectively, are visible in the Raman spectra. In the XRD patterns (Figs. S36c and S36d), there are a series of diffraction peaks at 13.7°, 31.4°, 37.9° and 55.9°, indexed to (002), (100), (103) and (110) facets of hexagonal $MoSe_2$ (JCPDS Card No. 29-0914), respectively. Clearly, with increasing the reaction temperature to 1273 and 1373 K, all the diffraction peaks become more

narrow and intense, instead of some broad peaks of $MoSe_2$ at a relatively low temperature of 1173 K (Fig. S33b).

Table S1. Transition-metal chalcogenides fabricated on the basis of a large family of non-van der Waals solids via our conversion reaction.

Non-van der Waals solids	S	H_2S	Se	H_2S+P	Se+P
Mo_2GeC	MoS_2 (Hexagonal, P63/mmc, 2H)	MoS_2 (Hexagonal, P63/mmc, 2H)	$MoSe_2$ (Hexagonal, P63/mmc, 2H)	P-doped MoS_2 (1T-2H)	
Ti_3SiC_2	Ti_5S_8 (Hexagonal, P63mc)	Ti_5S_8 (Hexagonal, P63mc)	$TiSe_2$ (Hexagonal, P3m1, 1T)		P-doped $TiSe_2$ (1T)
Ti_2SnC	Ti_5S_8 (Hexagonal, P63mc)	Ti_5S_8 (Hexagonal, P63mc)	$TiSe_2$ (Hexagonal, P3m1, 1T)		
Ti_2AlC	Ti_5S_8 (Hexagonal, P63mc)	Ti_5S_8 (Hexagonal, P63mc)	$TiSe_2$ (Hexagonal, P3m1, 1T)		
Nb_2AlC	NbS_2 (Rhombohedral, R3m)	NbS_2 (Rhombohedral, R3m)	$NbSe_2$ (Hexagonal, P-6m2)		
Ta_2AlC		TaS_2 (Hexagonal, P-3m1)			
TiNbAlC			Nb-doped $TiSe_2$ (1T)		
Mo_2TiAlC_2			$MoSe_2/TiSe_2$		
$(W_{2/3}Y_{1/3})_2AlC$	Y-doped WS_2 (2H)	Y-doped WS_2 (2H)		Y, P co-doped WS_2 (1T-2H)	
MoB	MoS_2 (Hexagonal, P63/mmc, 2H)	MoS_2 (Hexagonal, P63/mmc, 2H)	$MoSe_2$ (Hexagonal, P63/mmc, 2H)		
$MoSi_2$			$MoSe_2$ (Hexagonal, P63/mmc, 2H)		
Mo_2CT_x		MoS_2 (Hexagonal, P63/mmc, 2H)			

Table S2. Conversion reaction temperatures for various non-van der Waals solids to transition-metal chalcogenides.

Non-van der Waals solids	S	H_2S	Se	H_2S+P	Se+P
Mo_2GeC	MoS_2 1073 K# 900 K†	MoS_2 973-1373 K# 900 K†	$MoSe_2$ 1073 K# 900 K†	MoS_2 1073 K# 900 K†	
Ti_3SiC_2	Ti_5S_8 1273 K#	Ti_5S_8 1273 K#	$TiSe_2$ 1073-1373 K#		P-doped $TiSe_2$ 1173 K#
Ti_2SnC	Ti_5S_8 1173 K# 1000 K†	Ti_5S_8 1173 K# 1000 K†	$TiSe_2$ 1173 K# 1000 K†		
Ti_2AlC	Ti_5S_8 1273 K#	Ti_5S_8 1273 K#	$TiSe_2$ 1273 K#		
Nb_2AlC	NbS_2 1273 K#	NbS_2 1273 K#	$NbSe_2$ 1273 K#		
Ta_2AlC		TaS_2 1273 K#			
TiNbAlC			Nb-doped $TiSe_2$ 1273-1373 K#		
Mo_2TiAlC_2			$MoSe_2/TiSe_2$ 1273 K#		
$(W_{2/3}Y_{1/3})_2AlC$	Y-doped WS_2 1273 K#	Y-doped WS_2 1273 K#		Y, P co-doped WS_2 1273 K#	
MoB	MoS_2 1173 K#	MoS_2 1173-1373 K#	$MoSe_2$ 1073-1373 K#		
$MoSi_2$			$MoSe_2$ 1173-1373 K#		
Mo_2CT_x		MoS_2 873-1373 K#			

Note: # represents the experimentally demonstrated temperatures. † represents the minimum temperature evaluated from temperature-vapour pressure relationships in Fig. 1b.

S3. Characterization of 2D heteroatom-doped transition-metal chalcogenides derived from MAX phases

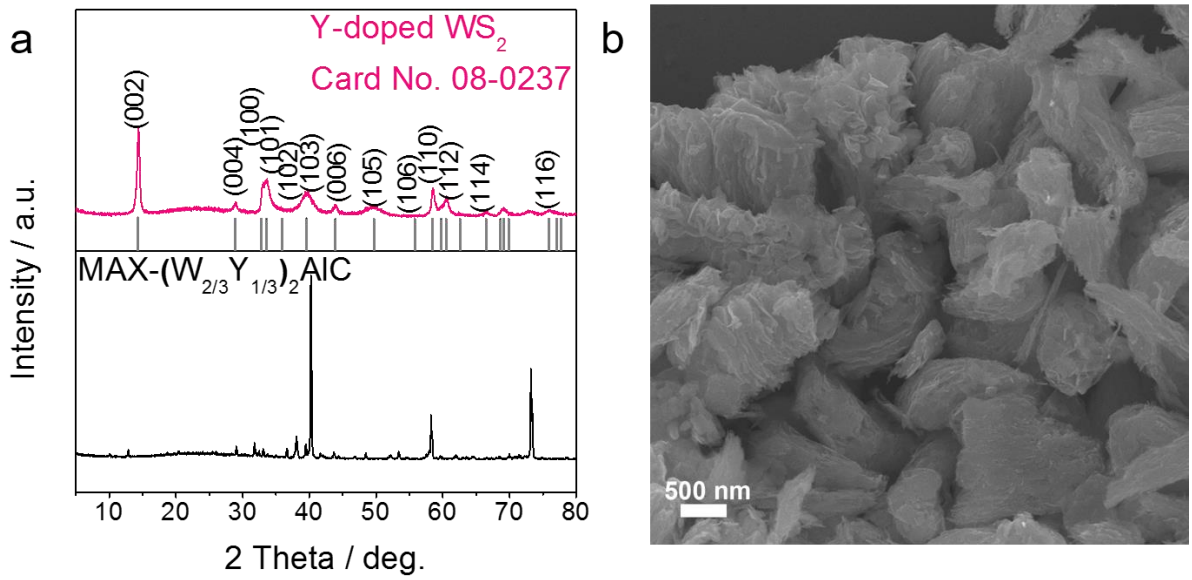

Fig. S37. Material characterization of Y-doped WS_2 by engineering quaternary MAX-$(W_{2/3}Y_{1/3})_2AlC$ under H_2S gas at 1273 K. a, XRD patterns, and **b**, SEM image of Y-doped WS_2 derived from quaternary MAX-$(W_{2/3}Y_{1/3})_2AlC$.

By substituting ternary MAX phases with quaternary MAX phases during our conversion process, heteroatom-doped transition-metal chalcogenides could be fabricated. As shown in Fig. S37a, a series of diffraction peaks are presented at 14.3°, 28.9°, 43.9° and 58.4°, indexed to the (002), (004), (006) and (110) facets of hexagonal WS_2 (JCPDS No. 08-0237), respectively. And there is no any diffraction peak for starting material $(W_{2/3}Y_{1/3})_2AlC$ (ref. [1]) in the XRD patterns of Y-doped WS_2, demonstrating the complete conversion during our fabrication process. SEM image of Y-doped WS_2 (Fig. S37b) exhibits many nano-accordions with expanded structure, similar to the resultant MoS_2 derived from Mo_2GeC (Fig. S9).

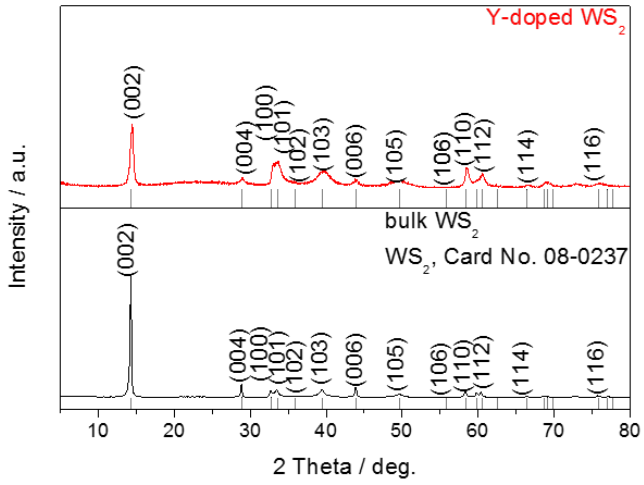

Fig. S38. XRD patterns of commercial bulk WS_2 and Y-doped WS_2 derived from $(W_{2/3}Y_{1/3})_2AlC$. In the XRD patterns of Y-doped WS_2, a series of diffraction peaks are presented at 14.3°, 28.9°, 43.9° and 58.4°, indexed to the (002), (004), (006) and (110) facets of hexagonal WS_2 (JCPDS No. 08-0237), respectively, same to those of bulk WS_2.

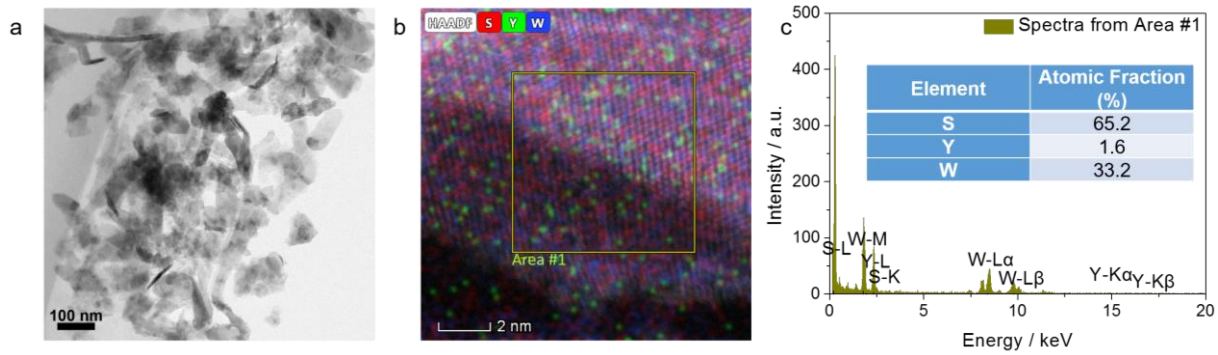

Fig. S39. TEM analysis of Y-doped WS_2 derived from $(W_{2/3}Y_{1/3})_2AlC$. a, TEM image of Y-doped WS_2. **b**, Overlapped elemental mapping image of S, W and Y species. **c**, EDS spectra acquired from the Area #1 from the elemental mapping image (**b**).

To evaluate the morphology and the composition of Y-doped WS_2, aberration-corrected transmission electron microscopy, energy dispersive X-ray spectroscopy (EDS) and elemental mapping measurements were conducted. As shown in Fig. S39a, numerous transparent nanosheets with several hundreds of nanometers in lateral size are visible. Overlapped elemental mapping image (Fig. S39b) reveals the co-existence of W, Y and S elements in the nanosheets, which could be further visualized by the EDS spectra (Fig. S39c) acquired from the Area #1 in Fig. S39b. Notably, the Y atoms are mainly mono-atomically dispersed in the nanosheets, associated with some degree of clustering Y. The atomic fraction of Y in Y-doped WS_2 is 1.6 at.%.

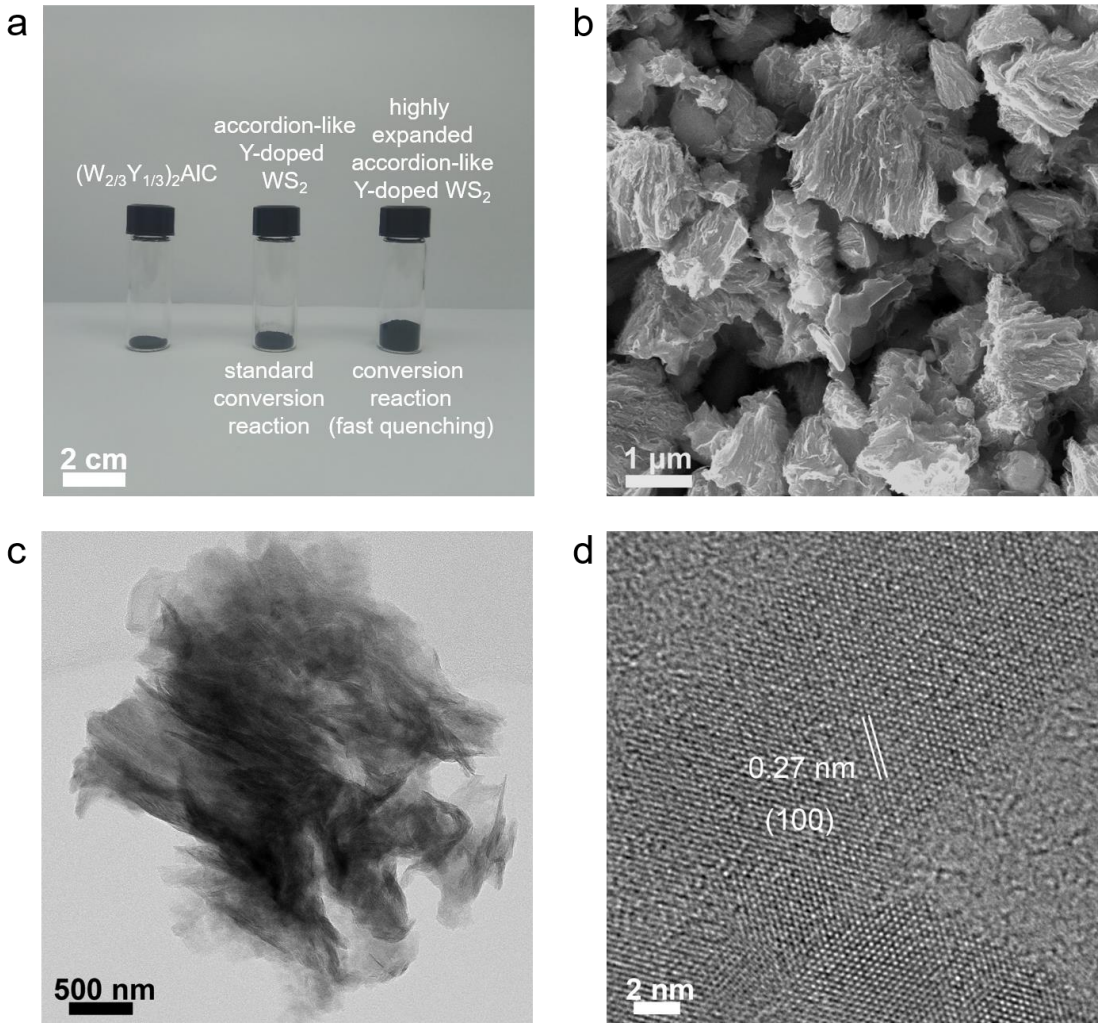

Fig. S40. Material characterization of highly expanded accordion-like Y-doped WS_2 synthesized from $(W_{2/3}Y_{1/3})_2AlC$ by conversion reaction in H_2S gas (fast quenching). a, Photographs of MAX-$(W_{2/3}Y_{1/3})_2AlC$, accordion-like Y-doped WS_2 synthesized by standard conversion reaction, highly expanded accordion-like Y-doped WS_2 synthesized by topological conversion reaction (fast quenching). **b-d**, SEM (**b**), TEM (**c**) and HRTEM (**d**) images of highly expanded accordion-like Y-doped WS_2 synthesized from $(W_{2/3}Y_{1/3})_2AlC$ by topological conversion reaction associated with fast quenching.

By engineering $(W_{2/3}Y_{1/3})_2AlC$ with H_2S gas at 1273 K and rapidly transferring the sample to a low temperature (room temperature) zone, highly expanded accordion-like Y-doped WS_2 was

produced. As shown in Fig. S40a, the expanded volume of highly expanded accordion-like Y-doped WS_2 is 7 times higher than that of MAX precursor and 2 times higher than that produced via our standard conversion reaction. SEM (Fig. S40b) and TEM (Fig. S40c) images exhibit the highly expanded accordion-like structure with ultrathin feature. HRTEM image (Fig. S40d) discloses a clear lattice distance of 0.27 nm, indexed to the interplanar spacing between the (100) facets of 2H WS_2.

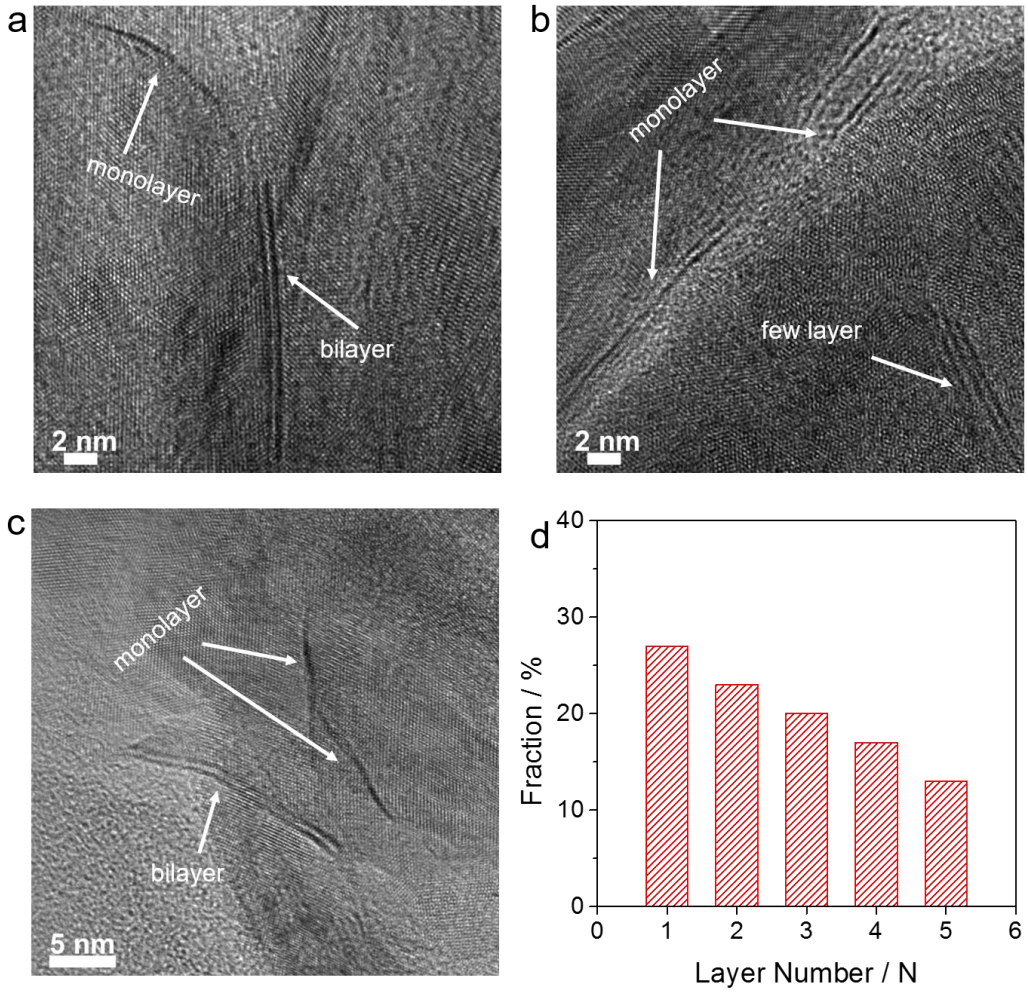

Fig. S41. Thickness analysis of highly expanded accordion-like Y-doped WS_2 synthesized via conversion reaction (fast quenching). a-c, Cross-sectional HRTEM images, and **d**, statistical analysis of Y-doped WS_2 nanosheets based on the thickness.

Cross-sectional HRTEM images (Fig. S41a-c) demonstrate the existence of monolayer, bilayer and few-layer Y-doped WS_2 in the highly expanded accordion-like structure. The fraction of monolayer is 27%, which is much higher than the yield from accordion-like Y-doped WS_2 produced via our standard topological conversion procedures (6%, Fig. S45c).

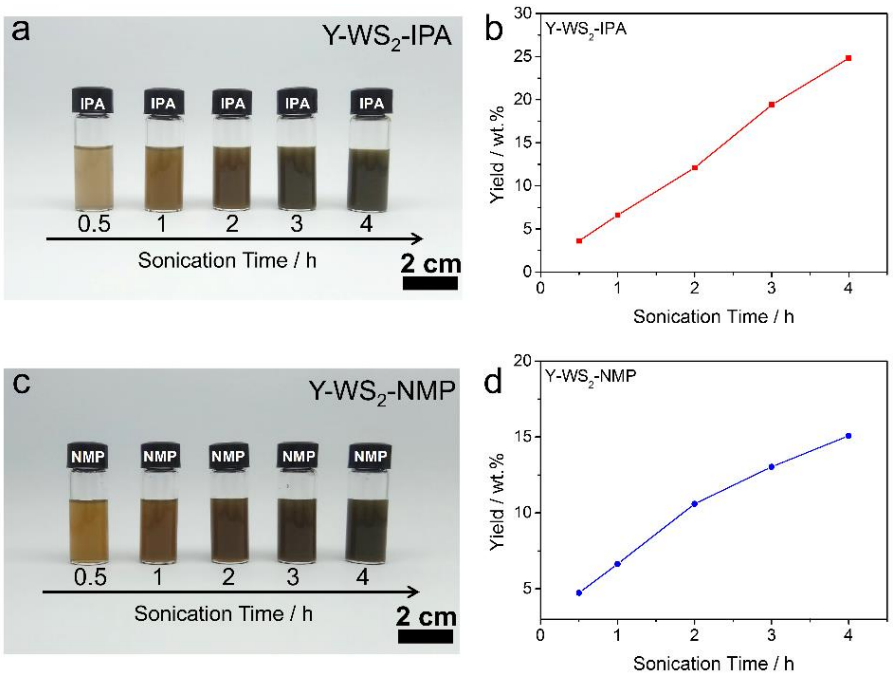

Fig. S42. Liquid-phase exfoliation of Y-doped WS_2 in IPA and NMP solvents. a, **c**. Photographs of the supernatants of WS_2 nanosheets exfoliated from accordion-like Y-doped WS_2 in IPA (**a**) and NMP (**c**) solvents with different sonication times from 0.5 to 4 h, showing that the colors of the supernatants become darker as increasing the sonication time. **b**, **d**. The yields of Y-doped WS_2 nanosheets exfoliated from accordion-like Y-doped WS_2 in IPA (**b**) and NMP (**d**) solvents plotted as a function of sonication time. The production yields of Y-doped WS_2 nanosheets exfoliated in IPA (Fig. S42b) and NMP (Fig. S42d) solvents were up to 24.8 and 15.1 wt.%, respectively, much higher than those reported for WS_2 exfoliated from bulk counterpart (1-2 wt.%)[6,14].

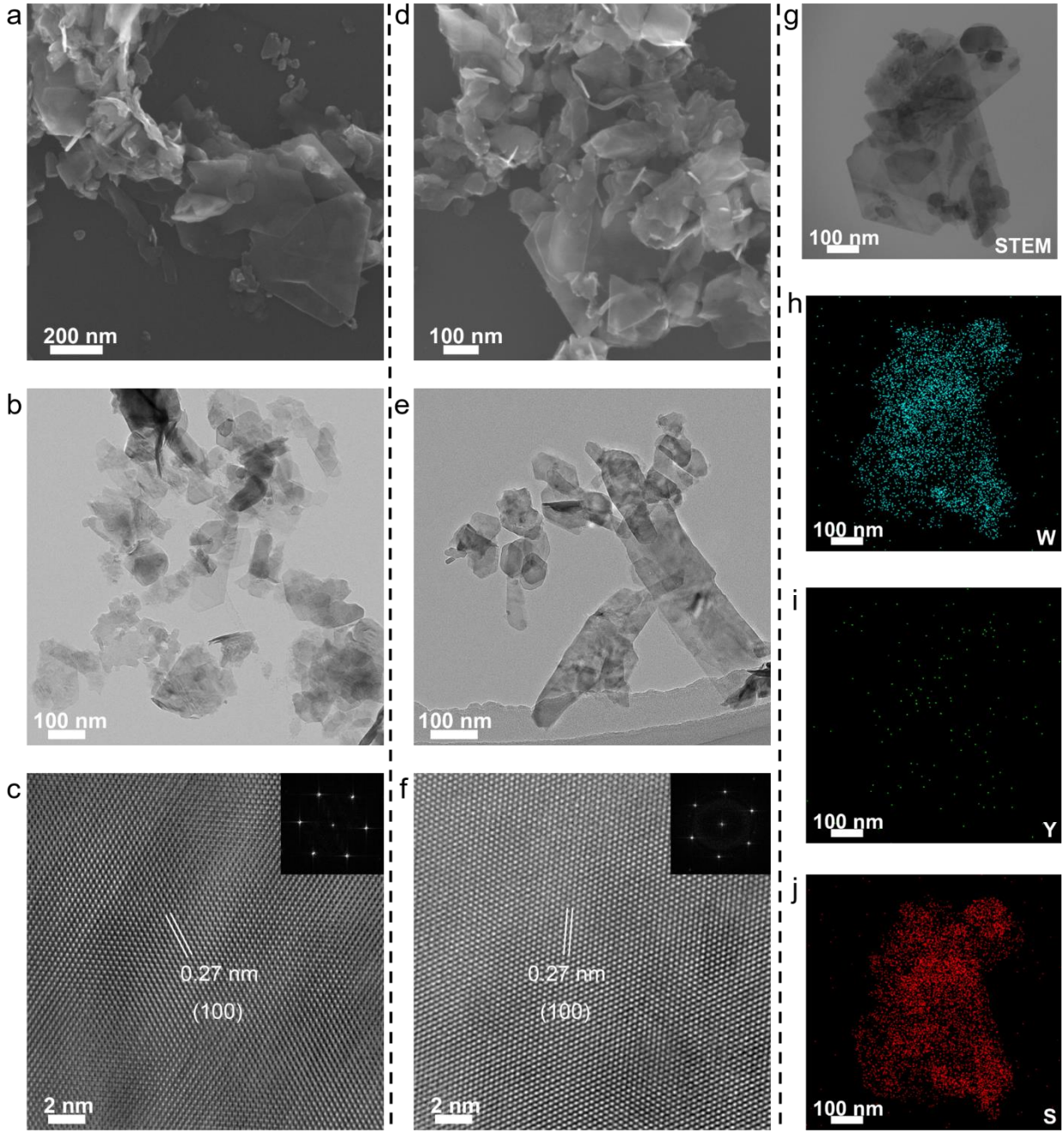

Fig. S43. Material characterization of Y-doped WS_2 nanosheets exfoliated from accordion-like Y-doped WS_2. a-c, SEM (**a**), TEM (**b**) and HRTEM (**c**) images of the exfoliated Y-doped WS_2 in IPA solvent. **d-f**, SEM (**d**), TEM (**e**) and HRTEM (**f**) images of the exfoliated Y-doped WS_2 in NMP solvents. **g-j**, STEM image (**g**), W (**h**), Y (**i**) and S (**j**) elemental mapping images of

exfoliated Y-doped WS_2 nanosheets. Insets in (**c**) and (**f**), the fast Fourier transform images of the corresponding HRTEM images.

To evaluate the free-standing Y-doped WS_2 nanosheets exfoliated from accordion-like Y-doped WS_2, scanning electron microscopy and transmission electron microscopy measurements were conducted. In Figs. S43a and S43d, some transparent and wrinkled 2D nanosheets are observed, suggesting the thin feature. TEM images (Figs. S43b and S43e) further reveal free-standing 2D transparent nanosheets under the electron beam, in good agreement with the observation from SEM images. HRTEM images (Figs. S43c and S43f) disclose the regular atomic arrangement and the hexagonal diffraction spots (insets), which demonstrates the high crystallinity of the resultant Y-doped WS_2 nanosheets. And a well-defined lattice distance of 0.27 nm is visible, indexed to the interplanar spacing between the (100) facets of 2H WS_2. STEM image (Fig. S43g) and elemental mapping images reveal the homogeneous distributions of W (Fig. S43h), Y (Fig. S43i) and S (Fig. S43j) species in the exfoliated Y-doped WS_2 nanosheets.

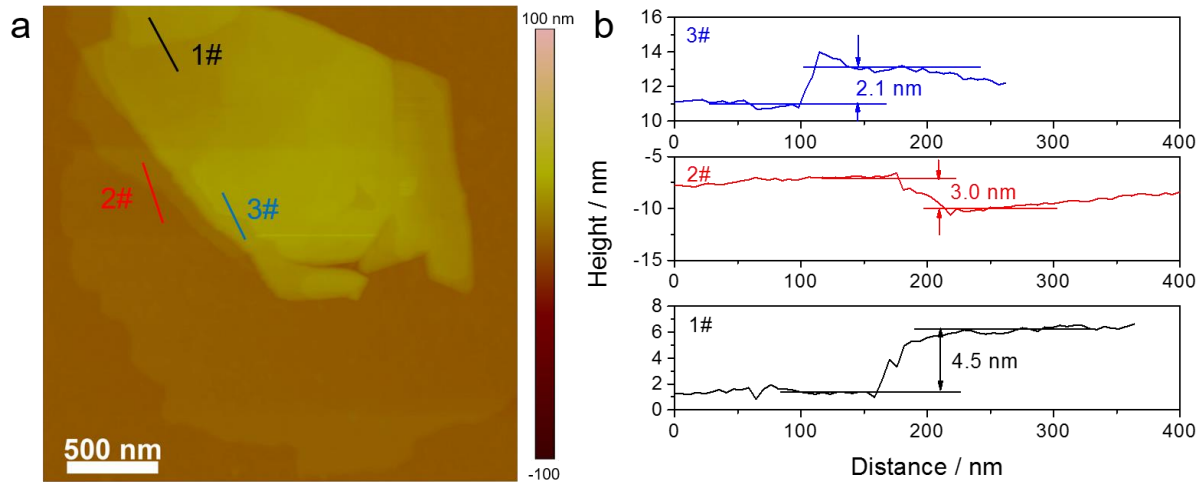

Fig. S44. Thickness analysis of Y-doped WS_2 nanosheets exfoliated from accordion-like Y-doped WS_2. a, AFM image, and **b**, the corresponding thickness analysis of Y-doped WS_2 nanosheets.

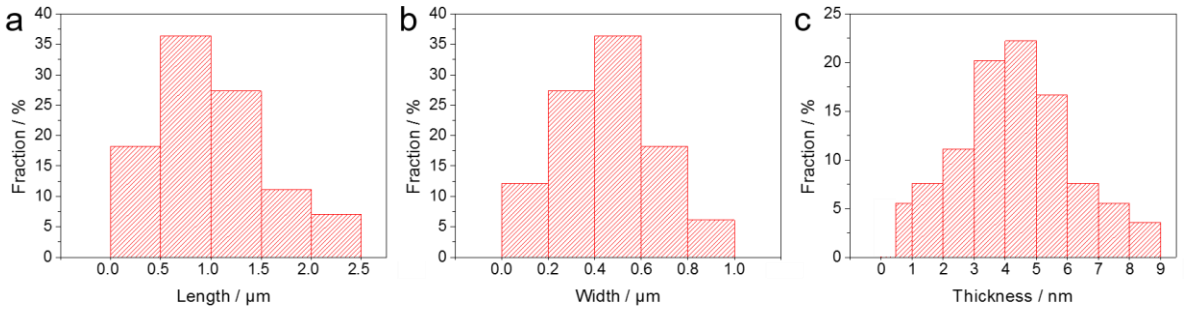

Fig. S45. Statistical analysis of Y-doped WS_2 nanosheets in accordion-like Y-doped WS_2. Statistical analysis of Y-doped WS_2 nanosheets based on the length (**a**), width (**b**) and thickness (**c**) of these nanosheets. As shown in Figs. S45a and S45b, the lateral sizes of the exfoliated Y-doped WS_2 nanosheets are mainly 0.3-1.5 μm in length and 0.2-0.8 μm in width, which are well consistent with the observations from SEM (Figs. S43a and S43d), TEM (Figs. S43b and S43e) and AFM (Fig. S44). Moreover, the thicknesses for the exfoliated Y-doped MoS_2 nanosheets are mainly 0.5-9 nm (Fig. S45c).

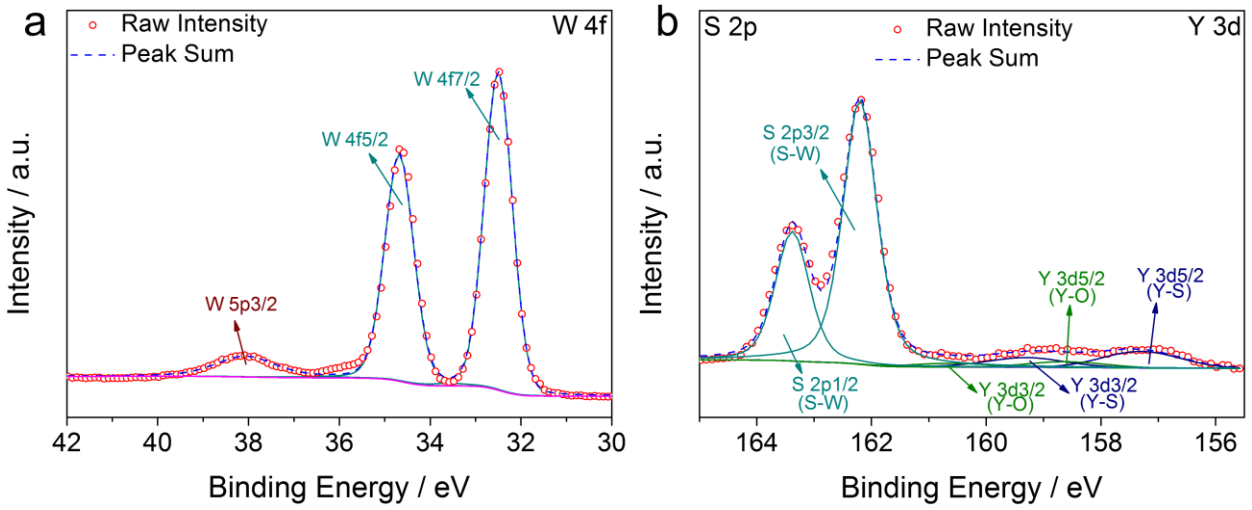

Fig. S46. XPS analysis of Y-doped WS_2 derived from $(W_{2/3}Y_{1/3})_2AlC$. a, High-resolution W 4f XPS spectra, **b**, high-resolution Y 3d and S 2p XPS spectra of the resultant Y-doped WS_2. Notably, the binding energy of Y 3d is very close to that of S 2p, so one baseline was set for both Y 3d and S 2p in (**b**).

To gain further insight into the chemical structure of Y-doped WS_2, X-ray photoelectron spectroscopy measurement and analysis were conducted. As shown in Fig. S46a, high-resolution W 4f XPS spectra could be fitted into two dominant peaks at 32.5 and 34.7 eV, corresponding to the W 4f7/2 and W 4f5/2 of W-S bonds in Y-doped WS_2, respectively. In addition, one peak is located at 38.1 eV, corresponding to the W 5p3/2 peak of W-O bonds. In the S 2p XPS spectra, one doublet located at 162.2 and 163.4 eV should be assigned to S 2p3/2 and S 2p1/2 peaks of S-W bonds, respectively. According to the literature[24], the binding energy of Y-O bonds should be presented at 158.6 eV (Y 3d5/2). Thus, in the high-resolution Y 3d XPS spectra (Fig. S46b), two peaks at 158.6 and 160.7 eV should be ascribed to the Y 3d5/2 and Y 3d3/2 peaks of Y-O bonds, respectively. One doublet located at 157.3 and 159.4 eV, is possibly assigned to the Y 3d5/2 and Y 3d3/2 peaks of Y-S bonds, respectively.

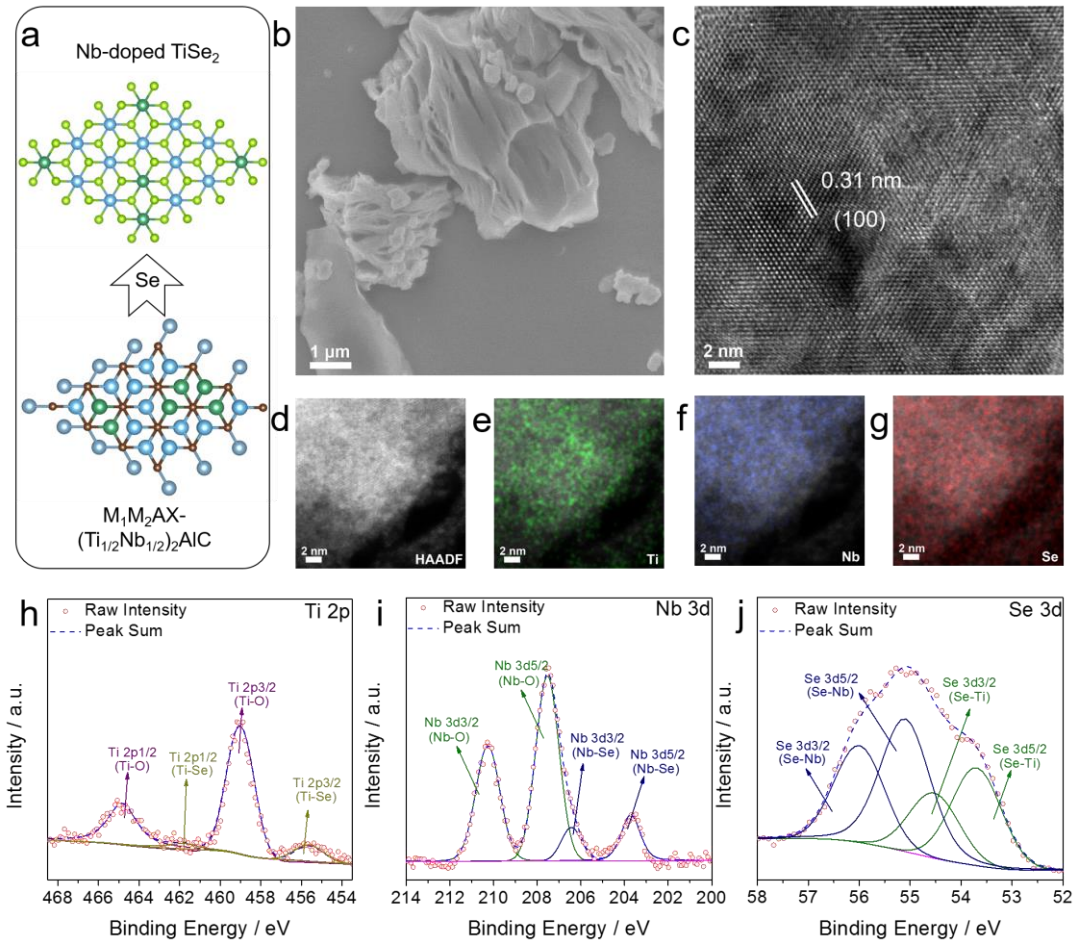

Fig. S47. Material characterization of Nb-doped $TiSe_2$ derived from $(Ti_{1/2}Nb_{1/2})_2AlC$ at 1273 K. a, Schematic diagram of the synthesis of Nb-doped $TiSe_2$ from $(Ti_{1/2}Nb_{1/2})_2AlC$. **b**, **c**. SEM (**b**) and HRTEM (**c**) images of Nb-doped $TiSe_2$. **d-g**, HAADF (**d**) and elemental mapping images, disclosing the uniform distributions of Ti (**e**), Nb (**f**) and Se (**g**) species. **h**, High-resolution Ti 2p spectra, **i**, high-resolution Nb 3d XPS spectra, and **j**, high-resolution Se 3d XPS spectra of Nb-doped $TiSe_2$ from $(Ti_{1/2}Nb_{1/2})_2AlC$.

Except for $(W_{2/3}Y_{1/3})_2AlC$, another quaternary MAX phases, $(Ti_{1/2}Nb_{1/2})_2AlC$, could be transformed to Nb-doped $TiSe_2$ under the action of Se vapour at a high temperature of 1273 K, as schematically illustrated in Fig. S47a. SEM image (Fig. S47b) shows some nano-accordions with expanded structure. HRTEM image (Fig. S47c) discloses a clear distance of 0.31 nm, which is

corresponding to the distance between the (100) facets for $TiSe_2$. STEM image (Fig. S47d) and elemental mapping images disclose the co-existence of Ti (Fig. S47e), Nb (Fig. S47f) and Se (Fig. S47g) in the nanosheets. To further confirm the composition of Nb-doped $TiSe_2$, X-ray photoelectron spectroscopy measurement and analysis were carried on. As shown in Fig. S47h, high-resolution Ti 2p XPS spectra could be fitted into two doublets at 455.6/461.8 and 459.0/464.8 eV. One doublet at 455.6 and 461.8 eV is assigned to the Ti 2p3/2 and Ti 2p1/2 peaks of Ti-Se bonds, respectively. Another doublet located at 459.0 and 464.8 eV is indexed to the Ti 2p3/2 and Ti 2p1/2 peaks of Ti-O bonds, respectively. High-resolution Nb 3d XPS spectra (Fig. S47i) could be deconvoluted into two doublets, in which one doublet is located at 203.8 and 206.5 eV, corresponding to Nb 3d5/2 and Nb 3d3/2 peaks of Nb-Se bonds, respectively; and the other at 207.6 and 210.3 eV is indexed to the Nb 3d5/2 and Nb 3d3/2 peaks of Nb-O bonds, respectively. In Fig. S47j, high-resolution Se 3d spectra could be fitted into two doublets at 53.7/54.5 eV and 55.1/56.0 eV, respectively. The first doublet at 53.7 and 54.5 eV is indexed to the Se 3d5/2 and Se 3d3/2 peaks for Se-Ti bonds, respectively. The second doublet at 55.1 and 56.0 eV is corresponding to the Se 3d5/2 and Se 3d3/2 peaks for the Se-Nb bonds, respectively.

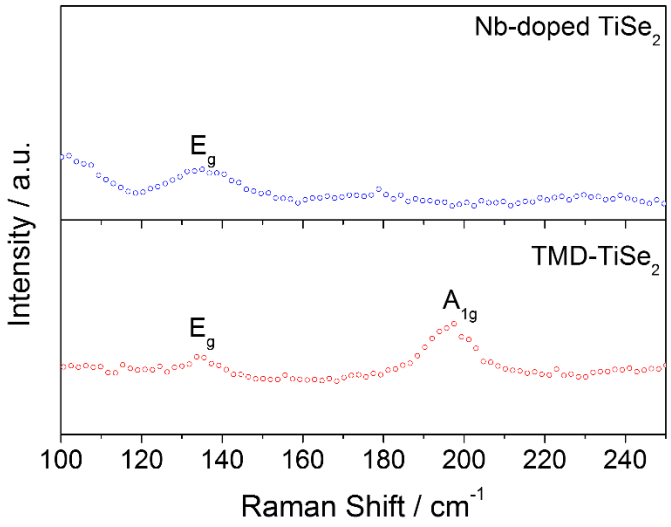

Fig. S48. Raman spectra of Nb-doped $TiSe_2$ from MAX-$(Ti_{1/2}Nb_{1/2})_2AlC$ at 1373 K and $TiSe_2$ from MAX-Ti_3SiC_2 at 1273 K. Raman spectra of Nb-doped $TiSe_2$, showing the typical peaks at 136 cm^{-1} for E_g vibrational mode of $TiSe_2$. As shown in Fig. S48, in the case of Nb-doped $TiSe_2$, the A_{1g} peak is disappeared, and the peak intensities are much weaker than those of pure $TiSe_2$, similar to the reported heteroatoms-doped transition-metal dichalcogenides, in which the heteroatom doping would significantly decrease the Raman peaks intensities[25,26].

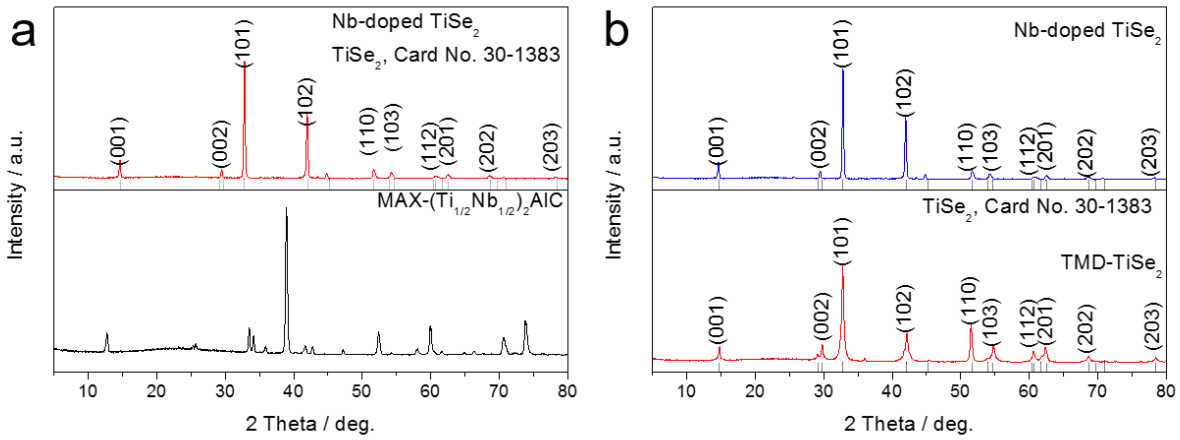

Fig. S49. XRD patterns of MAX-$(Ti_{1/2}Nb_{1/2})_2AlC$, Nb-doped $TiSe_2$ from $(Ti_{1/2}Nb_{1/2})_2AlC$, $TiSe_2$ from Ti_3SiC_2. a, XRD patterns of Nb-doped $TiSe_2$ and $(Ti_{1/2}Nb_{1/2})_2AlC$. **b**, XRD patterns of Nb-doped $TiSe_2$ and accordion-like $TiSe_2$. In Fig. S49a, different from the XRD patterns for MAX-$(Ti_{1/2}Nb_{1/2})_2AlC$ (ref. [2]), the XRD patterns of Nb-doped $TiSe_2$ show a series of diffraction peaks at 29.7°, 32.8°, 42.1° and 51.6°, corresponding to (002), (101), (102) and (110) facets of hexagonal $TiSe_2$ (JCPDS No. 30-1383), respectively, demonstrating the transformation of non-van der Waals $(Ti_{1/2}Nb_{1/2})_2AlC$ to van der Waals Nb-doped $TiSe_2$. Moreover, the XRD patterns of Nb-doped $TiSe_2$ exhibit the same diffractions peaks as those of accordion-like $TiSe_2$ (Fig. S49b).

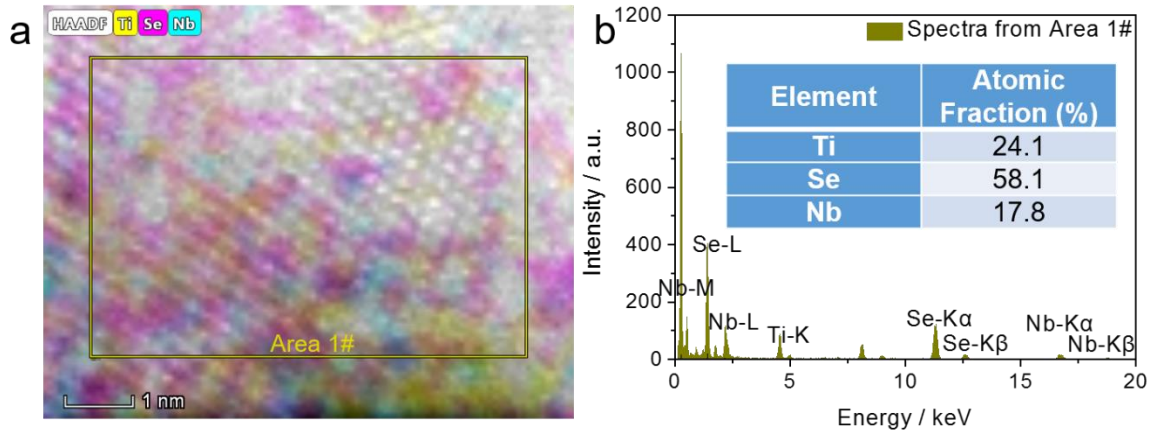

Fig. S50. EDS analysis of Nb-doped $TiSe_2$ from $(Ti_{1/2}Nb_{1/2})_2AlC$. a, Overlapped mapping image, demonstrating the co-existence of Ti, Se and Nb species. **b**, EDS spectra acquired from the Area 1# highlighted in (**a**), indicating that the atomic fraction of Nb in Nb-doped $TiSe_2$ is 17.8 at.%.

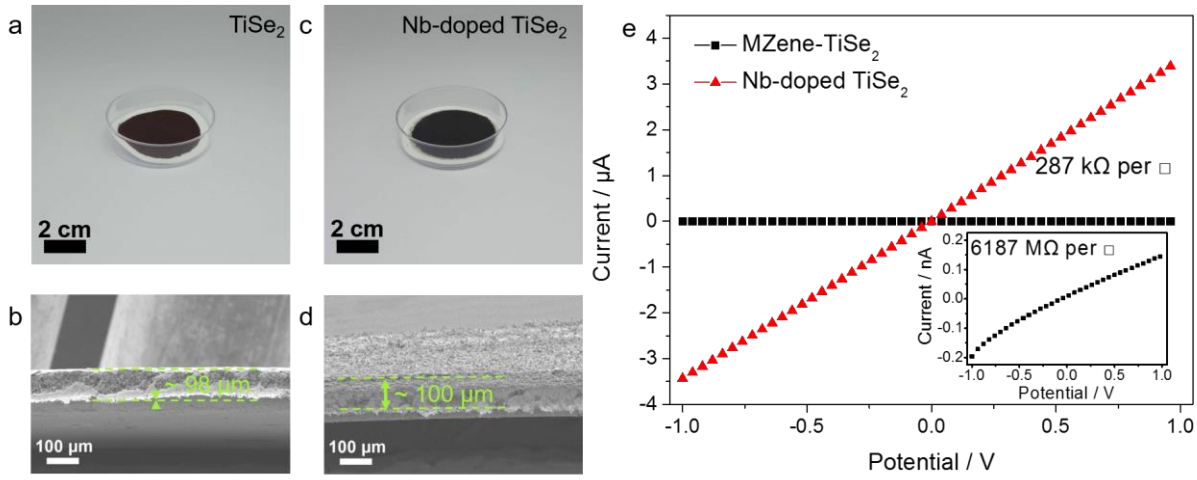

Fig. S51. Electrical property of $TiSe_2$ from Ti_3SiC_2 and Nb-doped $TiSe_2$ from $(Ti_{1/2}Nb_{1/2})_2AlC$. **a**-**d**, Photographs and thicknesses for $TiSe_2$ (**a**, **c**) and Nb-doped $TiSe_2$ (**b**, **d**) thin films, respectively, indicating the similar sizes and thicknesses. **e**, Current versus voltage curves for $TiSe_2$ and Nb-doped $TiSe_2$ thin films, where the sheet resistance for Nb-doped $TiSe_2$ thin film is 287 kΩ per □, four orders of magnitude lower than that of $TiSe_2$ thin film (6187 MΩ per □), demonstrating that electron transfer can be enhanced by Nb doping in $TiSe_2$.

Table S3. Electrical conductivities for transition-metal chalcogenides.

	Electrical conductivity / S cm^{-1}
Bulk WS_2	8.13×10^{-2}
Y-doped WS_2	2.31×10^{-3}
Y, P co-doped WS_2	0.0205
P-doped WS_2	0.012
Accordion-like $TiSe_2$	2.71×10^{-4}
Nb-doped $TiSe_2$	1.81

As shown in Table S3, the electrical conductivity of accordion-like 1T $TiSe_2$ is 2.71×10^{-4} S cm^{-1}, which is close to the reported value for 1T $TiSe_2$ (1×10^{-3} S cm^{-1})[27], much lower than that of Nb-doped $TiSe_2$ (1.81 S cm^{-1}). Moreover, the electrical conductivity of Y-doped WS_2 is 2.31×10^{-3} S cm^{-1}, lower than that of accordion-like Y, P co-doped WS_2 (0.0205 S cm^{-1}). This should be ascribed to the presence of 1T phase in the resultant Y, P co-doped WS_2.

S4. Characterization of 2D heteroatoms (Y and P) co-doped WS_2 with 1T phase derived from quaternary MAX-$(W_{2/3}Y_{1/3})_2AlC$

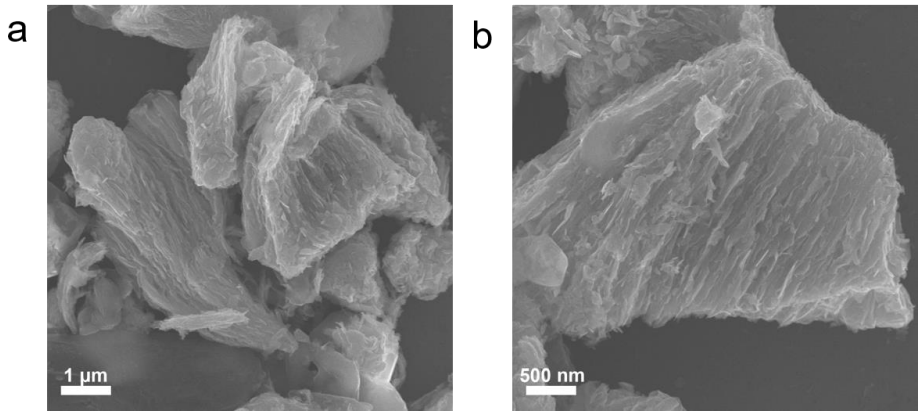

Fig. S52. Morphology characterization of Y, P co-doped WS_2 from engineering $(W_{2/3}Y_{1/3})_2AlC$ by H_2S gas and P vapour at 1273 K. a, **b**. SEM images, showing expanded accordion-like structure, similar to the Y-doped WS_2 (Fig. 3b) derived from MAX-$(W_{2/3}Y_{1/3})_2AlC$.

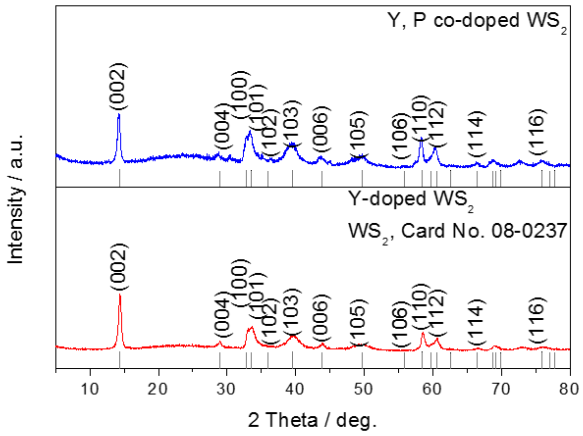

Fig. S53. XRD patterns of Y, P co-doped WS_2 (from engineering $(W_{2/3}Y_{1/3})_2AlC$ by H_2S gas and P vapour) and Y-doped WS_2 (from engineering $(W_{2/3}Y_{1/3})_2AlC$ by H_2S gas). In the XRD patterns of Y, P co-doped WS_2, there are a series of diffraction peaks presented at 14.3°, 28.9°, 43.9° and 58.4°, indexed to the (002), (004), (006) and (110) facets of hexagonal WS_2 (JCPDS No. 08-0237), respectively, same to those of Y-doped WS_2.

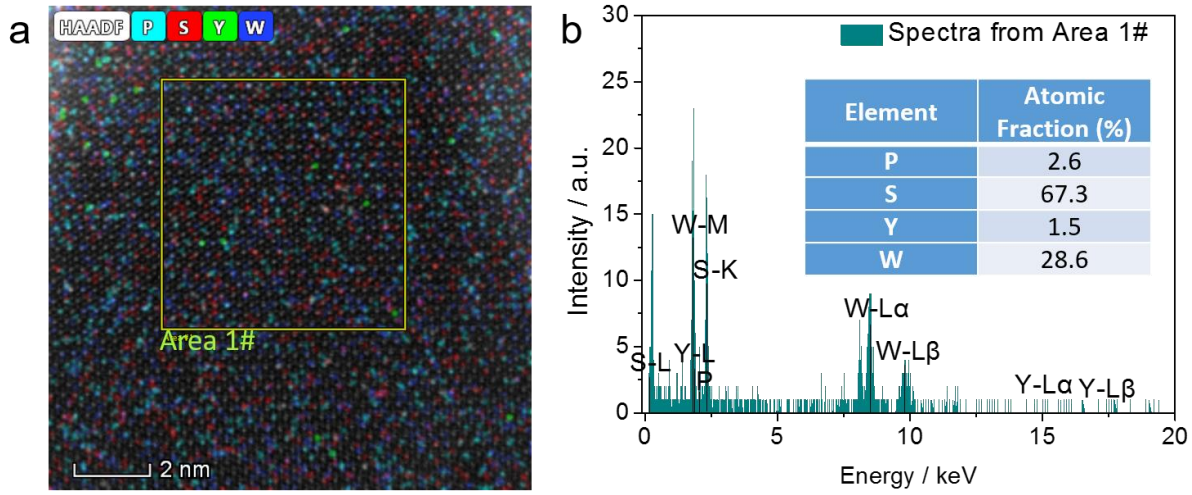

Fig. S54. EDS analysis of Y, P co-doped WS_2 from engineering $(W_{2/3}Y_{1/3})_2AlC$ by H_2S gas and P vapour. a, Overlapped mapping image of P, S, Y and W species. **b**, EDS spectra acquired from the Area 1# highlighted in (**a**).

To further identify the composition of Y, P co-doped WS_2, energy dispersive X-ray spectroscopy (EDS) and elemental mapping measurements were conducted. As shown in Fig. S54a, overlapped elemental mapping image reveals the co-existence of P, S, Y and W elements in the nanosheets, which could be further visualized by the EDS spectra (Fig. S54b) acquired from the Area 1# in Fig. S54a. Notably, the Y atoms are mainly mono-atomically dispersed in the nanosheets. The atomic fractions of Y and P in Y, P co-doped WS_2 are 1.5 and 2.6 at.%, respectively.

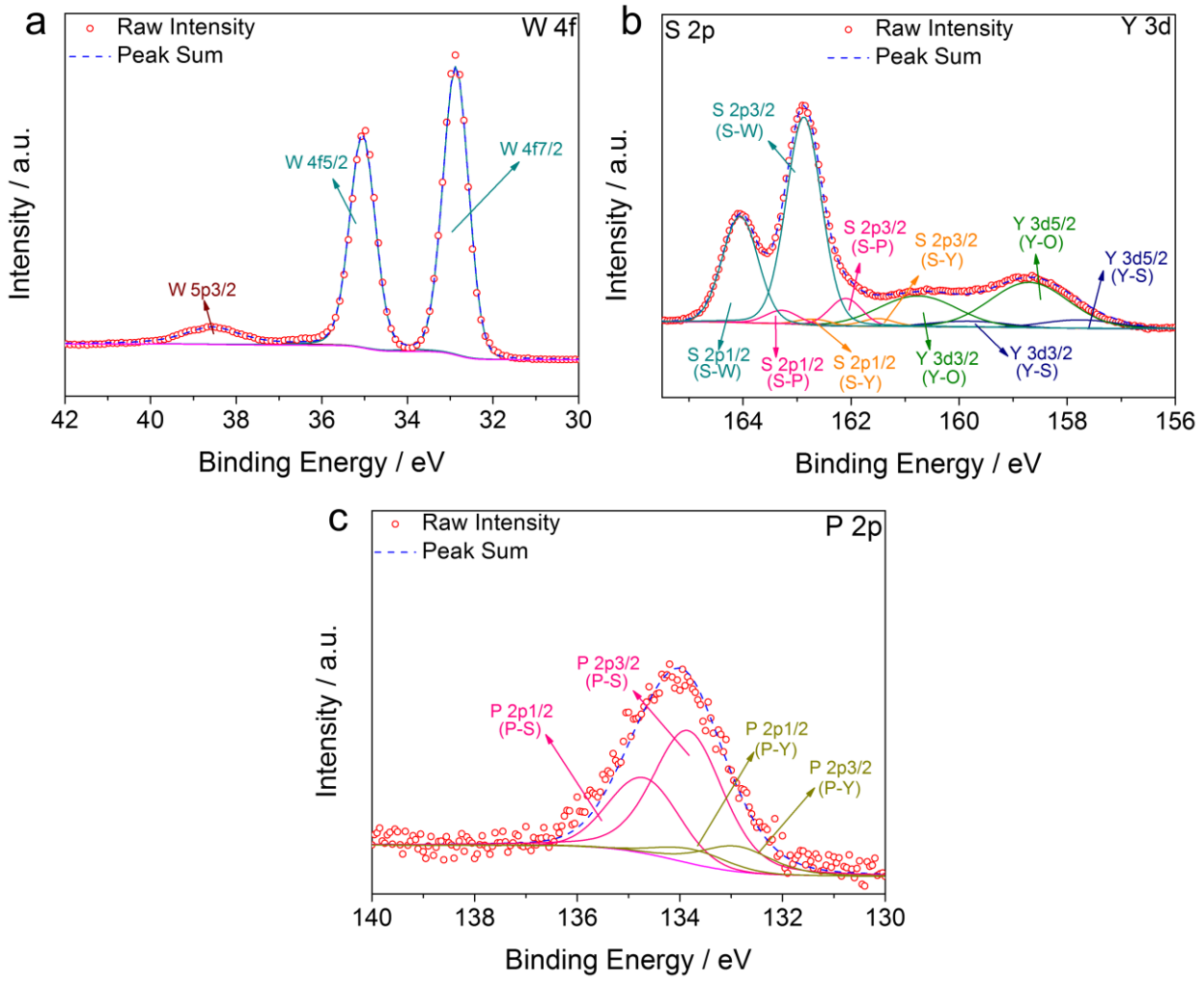

Fig. S55. XPS analysis of Y, P co-doped WS_2 from engineering $(W_{2/3}Y_{1/3})_2AlC$ by H_2S gas and P vapour. a, High-resolution W 4f XPS spectra, **b**, S 2p and Y 3d XPS spectra, and **c**, P 2p spectrum of Y, P co-doped WS_2. Notably, the binding energy of Y 3d is very close to that of S 2p, so one baseline was set for both Y 3d and S 2p in (**b**).

To gain insight into the chemical structure of Y, P co-doped WS_2, X-ray photoelectron spectroscopy measurement and analysis were conducted. As shown in Fig. S55a, high-resolution W 4f XPS spectra could be fitted into two peaks at 32.9 and 35.1 eV for W 4f7/2 and W 4f5/2, respectively, which are assigned to W-S bonds. In addition, one peak located at 38.6 eV is corresponding to the W 5p3/2 peak of W-O bonds. For high-resolution S 2p and Y 3d XPS spectra

(Fig. S55b), the fitting of the XPS spectra is very hard since there are five species (W, Y, S, P, O) in one sample and low levels of the dopants, as well as the close binding energies between strong S 2p (161-165 eV) and weak Y 3d (156-161 eV) peaks. As for the S 2p spectra of Y, P co-doped WS_2, the fitting procedure was carried out as following: one dominant doublet at the binding energies of 162.9/164.1 eV were firstly added, which should be assigned to S-W bonds. And then we added one doublet at the binding energies of 162.1/163.3 eV, which may be assigned to the S-P bonds. Then one doublet at the binding energies of 161.5/162.7 eV was added, which may be assigned to the S-Y bonds according to the literature on S-Y bonds (161.5 eV for S 2p3/2)[28]. In the Y 3d XPS spectra (Fig. S55b), one doublet at 157.6 and 159.7 eV should be assigned to Y 3d5/2 and Y 3d3/2 peaks of Y-S bonds, respectively, according to the reported Y-S bonds (157.6 eV for Y 3d5/2)[28]. Another doublet located at 158.6 and 160.7 eV should be corresponding to Y 3d5/2 and Y 3d3/2 peaks of Y-O bonds[24], respectively. Owing to the low levels of the P and Y dopants, the doublet for Y-P bonds in high-resolution Y 3d XPS spectra was not considered. For high-resolution P 2p XPS spectra (Fig. S55c), one doublet located at 133.8 and 134.6 eV should be assigned to P 2p3/2 and P 2p1/2 peaks of P-S bonds, respectively, close to the reported P-S bonds (134.2 eV for P 2p3/2)[29] and far from the reported P-O bonds (135.6 eV for P 2p3/2)[30]. Another doublet at 132.9 and 133.7 may be corresponding to Y 3d5/2 and Y 3d3/2 peaks of Y-P bonds, respectively. All the XPS peak fitting parameters were listed in Table S9.

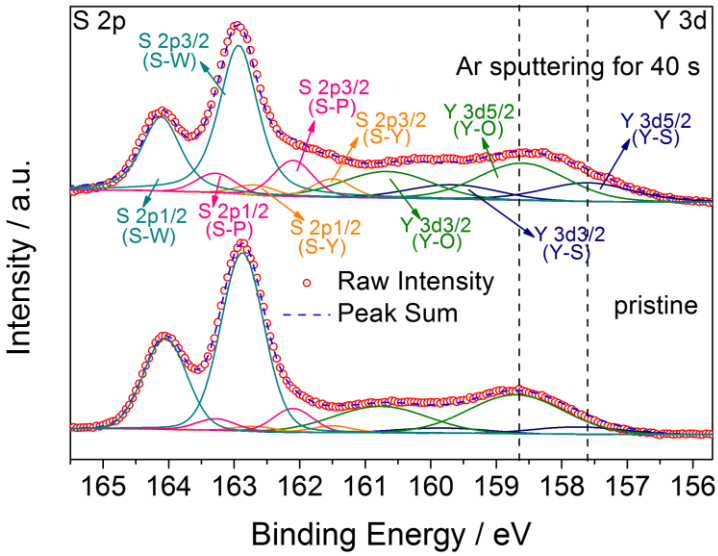

Fig. S56. XPS spectra of Y, P co-doped WS_2 before and after Ar sputtering. High-resolution S 2p and Y 3d XPS spectra of Y, P co-doped WS_2 before and after Ar sputtering for 40 s. Notably, the binding energy of Y 3d is very close to that of S 2p, so one baseline was set for both Y 3d and S 2p XPS spectra.

To possibly fit the Y 3d spectra of Y, P co-doped WS_2, we conducted Ar sputtering XPS spectra of Y, P co-doped WS_2 (Fig. S56, sputtering for 40 s) to gain the influence of Ar sputtering on the Y-O bonds. For comparison, after Ar sputtering, the highest intensity of the Y 3d spectra was shifted from 158.6 to 158.3 eV, suggesting that the previously highest intensity peak at 158.6 eV should be assigned to Y-O bonds, which is also well consistent with the reported Y-O bonds[24]. Hence, one doublet located at 158.6 and 160.7 eV was assigned to the Y 3d5/2 and Y 3d3/2 peaks of Y-O bonds, respectively. After Ar sputtering for 40 s, the low binding energy range (156-157.5 eV) in Y 3d spectra become stronger. So we added one doublet at 157.6/159.7 eV in the Y 3d spectra, which may be assigned to the Y-S bonds according to the reported Y 3d5/2 of Y-S bonds at 157.6 eV (ref. [28]). Owing to the low levels of the P and Y dopants, the doublet for Y-P bonds in high-resolution Y 3d XPS spectra was not considered.

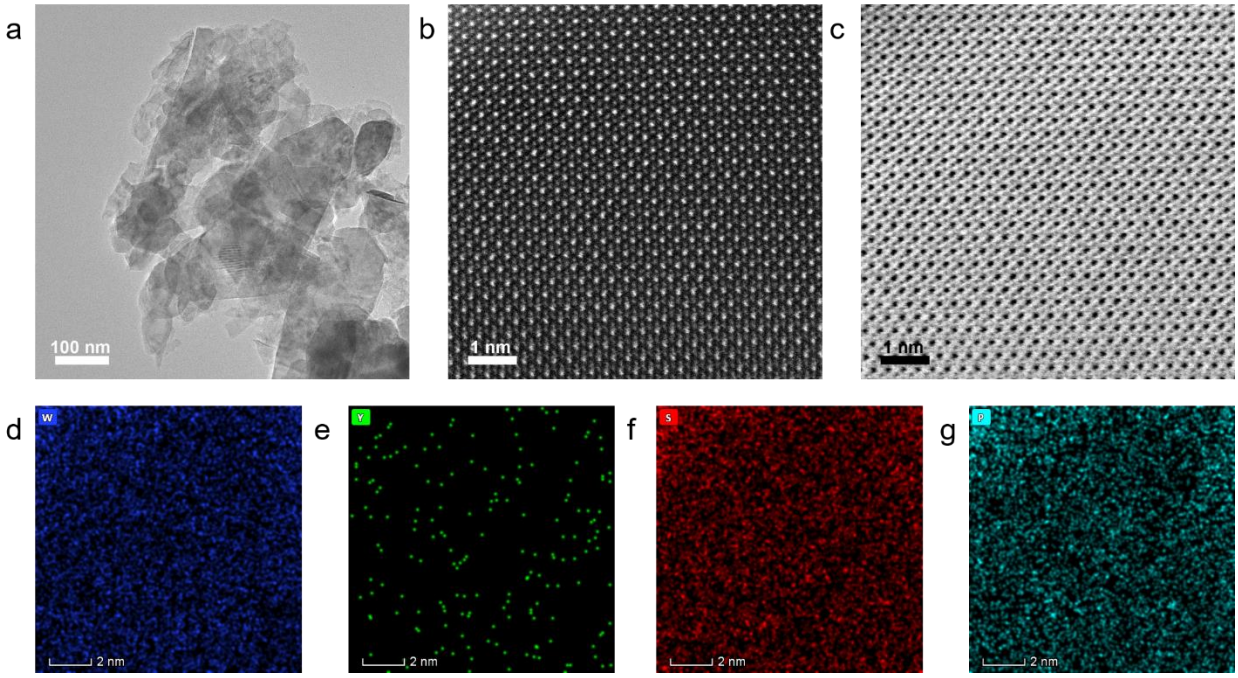

Fig. S57. Structural analysis of Y, P co-doped WS_2 from engineering $(W_{2/3}Y_{1/3})_2AlC$ by H_2S gas and P vapour. a, TEM image. **b**, **c**. HAADF-STEM (**b**) and ABF (**c**) images. **d-g**, Elemental mapping images of W (**d**), Y (**e**), S (**f**) and P (**g**) in Y, P co-doped WS_2 nanosheets.

The microstructure of Y, P co-doped WS_2 was evaluated via aberration-corrected scanning transmission electron microscopy and elemental mapping measurements. As shown in Fig. S57a, there are some free-standing nanosheets in the TEM image of exfoliated Y, P co-doped WS_2, which are transparent under the electron beam. By using image contrast, the S and W elements can be clearly identified in HAADF-STEM image (Fig. S57b) and annular bright field (ABF) image (Fig. S57c). All the metal W atoms are located at the center of octahedral units, in accordance with the atomic models of 1T phase[31]. Elemental mapping images reveal the uniform distributions of W (Fig. S57d), S (Fig. S57f) and P (Fig. S57g) in Y, P co-doped WS_2. Y is mainly mono-atomically dispersed in the nanosheets (Fig. S57e).

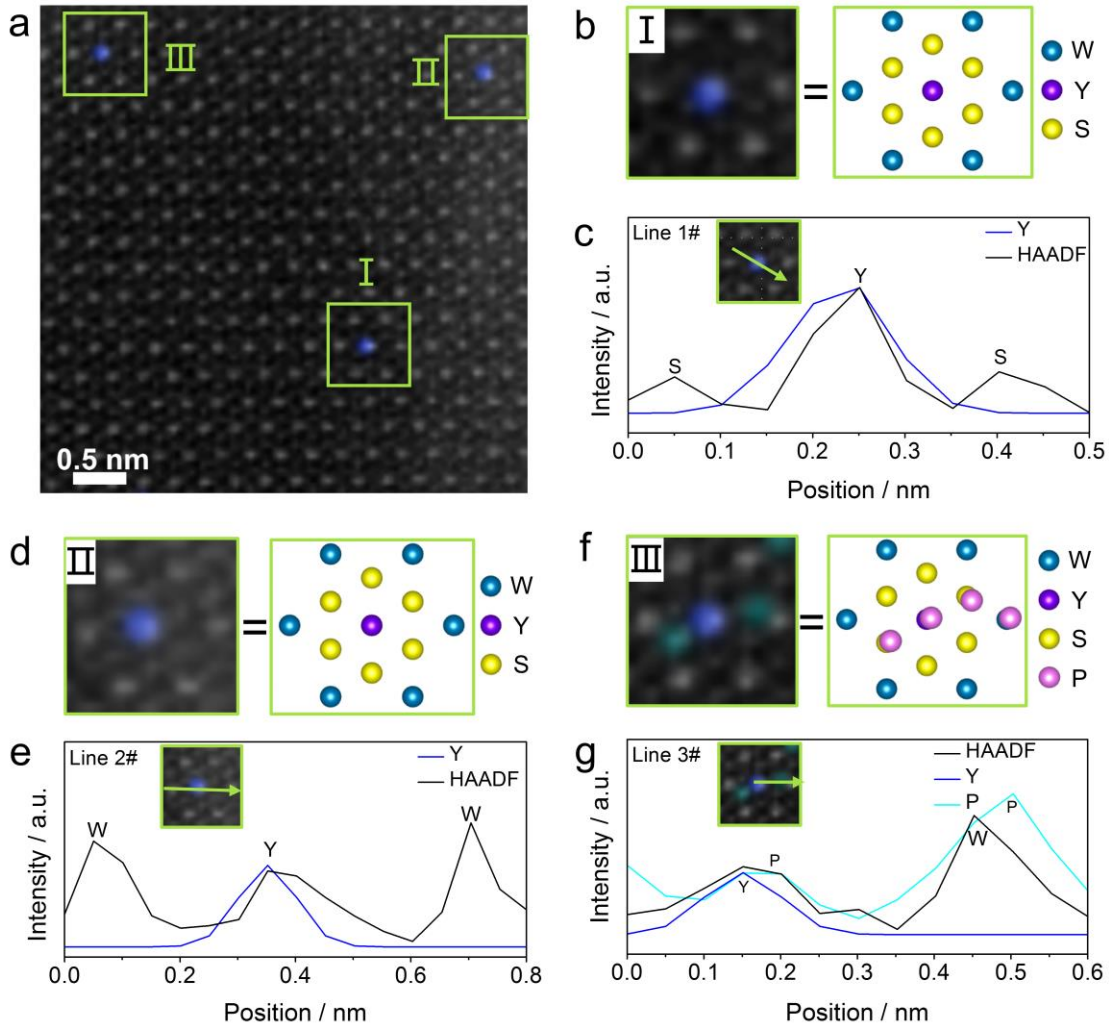

Fig. S58. Atomic structure analysis of Y, P co-doped WS_2. a, Atomic-resolution Y elemental mapping image. **b**, **d**. Y elemental mapping images with high magnification for Area I (**b**), II (**d**) highlighted in (**a**), and the corresponding atomic configuration. **c**, **e**. Line intensity profiles acquired from the highlighted arrow in Insets of Area I (**b**), II (**d**). **f**, Y, P elemental mapping image with high magnification for Area III in (**a**), and the corresponding atomic configuration. **g**, Line intensity profiles acquired from the highlighted arrow in Inset of Area III (**f**).

To gain the fine structure of Y, P co-doped WS_2, atomic-resolution STEM, elemental mapping images and the corresponding analysis were conducted. In the atomic-resolution Y elemental mapping images as shown in Figs. S58a, S58b and S58d, all the Y atoms are located at the center

of octahedral units, occupying the W sites in 1T WS_2. This can be further demonstrated via the line intensity profiles (Figs. S58c and S58e for Area I and II, respectively), in which the intensities of Y sites are weaker than that of W sites and stronger than that of S sites, directly demonstrating the presence of Y-S bonds in Y, P co-doped WS_2. By carefully analyzing the Y, P elemental mapping image (Fig. S58f) and the line intensity profiles (Fig. S58g), it is clear that the P atoms are located on the top of both Y and S sites, suggesting that there are Y-P and P-S bonds appeared in P, Y co-doped WS_2.

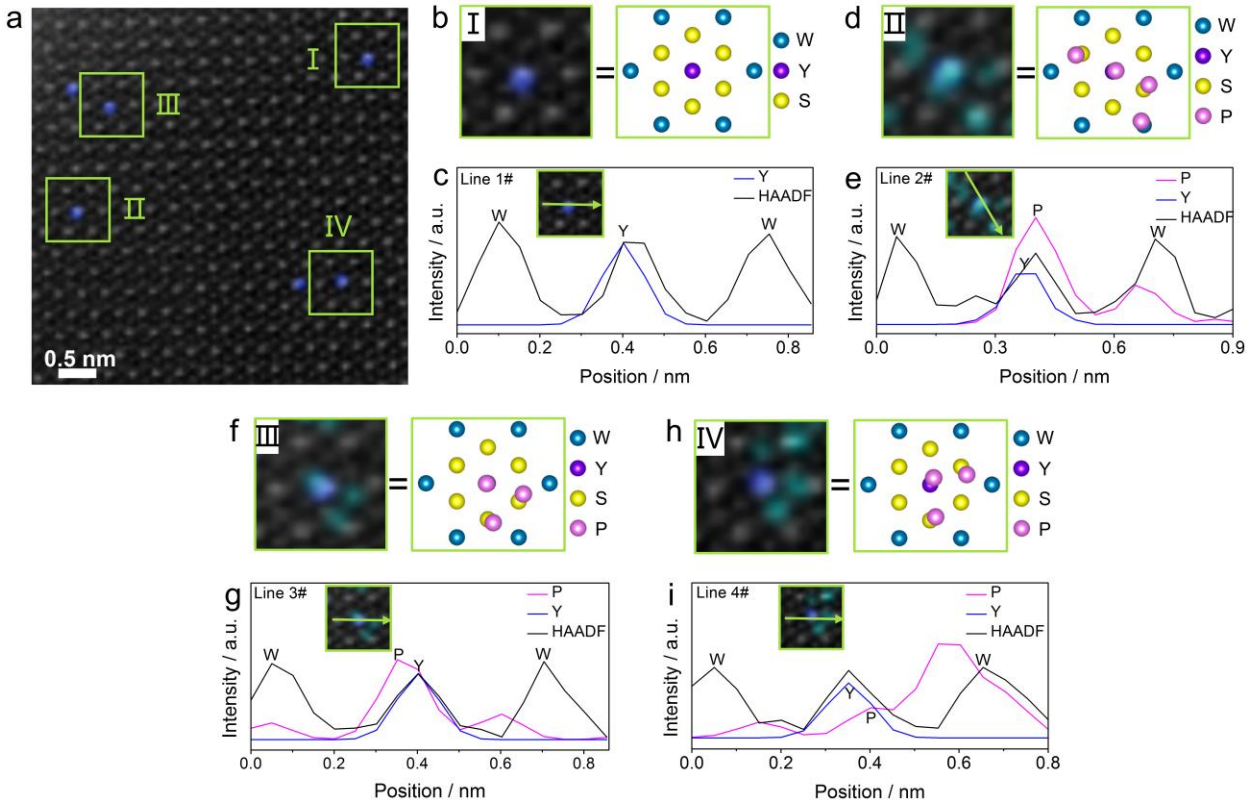

Fig. S59. Atomic structure analysis of Y, P co-doped WS_2. a, Atomic-resolution Y elemental mapping image. **b**, Y elemental mapping image with high magnification for Area I highlighted in (**a**), and the corresponding atomic configuration. **c**, Line intensity profiles acquired from the highlighted arrow in Insets of Area I (**b**). **d**, **f**, **h**. Y, P elemental mapping images with high magnifications for Area II (**d**), III (**f**) and IV (**h**) highlighted in (**a**), and the corresponding atomic configuration. **e**, **g**, **i**. Line intensity profiles acquired from the highlighted arrow in Insets of Area II (**d**), III (**f**) and IV (**h**).

In the atomic-resolution Y elemental mapping images as shown in Fig. S59a and S59b, all the Y atoms are located at the center of octahedral units, occupying the W sites in 1T WS_2. This could be further demonstrated via the line intensity profiles (Figs. S59c for Area I), in which the intensities of Y sites are weaker than that of W sites and stronger than that of S sites, directly demonstrating the presence of Y-S bonds in Y, P co-doped WS_2. In the Y, P elemental mapping

images (Figs. S59d, S59f and S59h), all the Y atoms occupy the W sites in WS_2 and P atoms are located on the top of both Y and S sites, demonstrating the presence of Y-S, Y-P and P-S bonds, which can be further confirmed by the line intensity profiles (Figs. S59e, S59g and S59i).

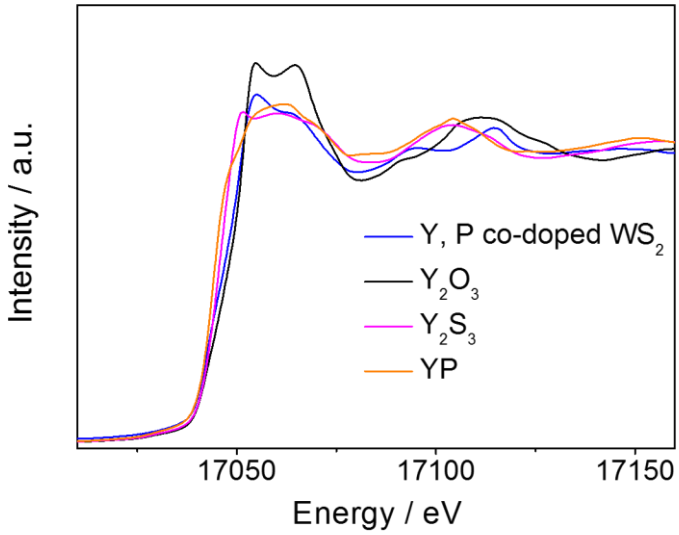

Fig. S60. Y K-edge XANES spectra of Y, P co-doped WS_2 compared with those of Y_2O_3, Y_2S_3 and YP. Y K-edge XANES spectra (Fig. S60) show that the adsorption edge of Y, P co-doped WS_2 is located between those of Y_2S_3 and Y_2O_3, indicating that some Y species are presented in the state of oxidation, which can also be verified the Fourier transforms spectra of EXAFS results (Fig. 4e).

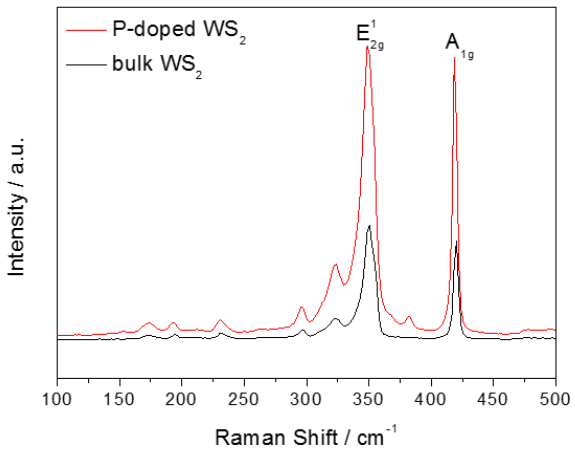

Fig. S61. Raman spectra of commercial bulk WS_2 and P-doped WS_2 from engineering bulk WS_2 under P vapour. Raman spectra of P-doped WS_2, exhibiting the typical in-plane $E_{2g}{}^1$ (349 cm^{-1}) and out-of-plane A_{1g} (418 cm^{-1}) vibrational modes for 2H WS_2 (ref. [32]), demonstrating that independent P adsorbed/doped on WS_2 cannot afford 1T phase in P-doped WS_2. This result is consistent with the theoretical calculation in Fig. S68.

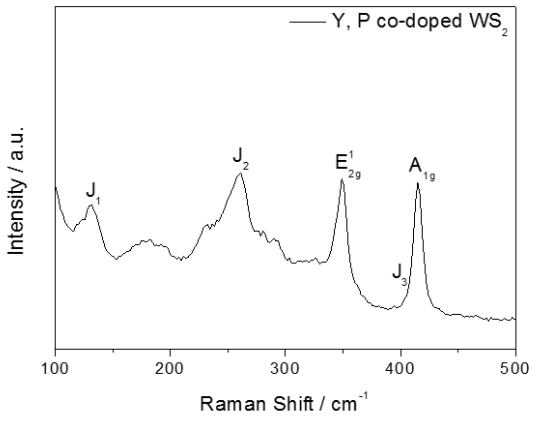

Fig. S62. Raman spectra of Y, P co-doped WS_2 from engineering $(W_{2/3}Y_{1/3})_2AlC$ by H_2S gas and P vapour after storing at ambient conditions for one year. The typical peaks of J_1, J_2 and J_3 for 1T WS_2 still exist in Y, P co-doped WS_2, demonstrating the good stability of our 1T WS_2 in P, Y co-doped WS_2.

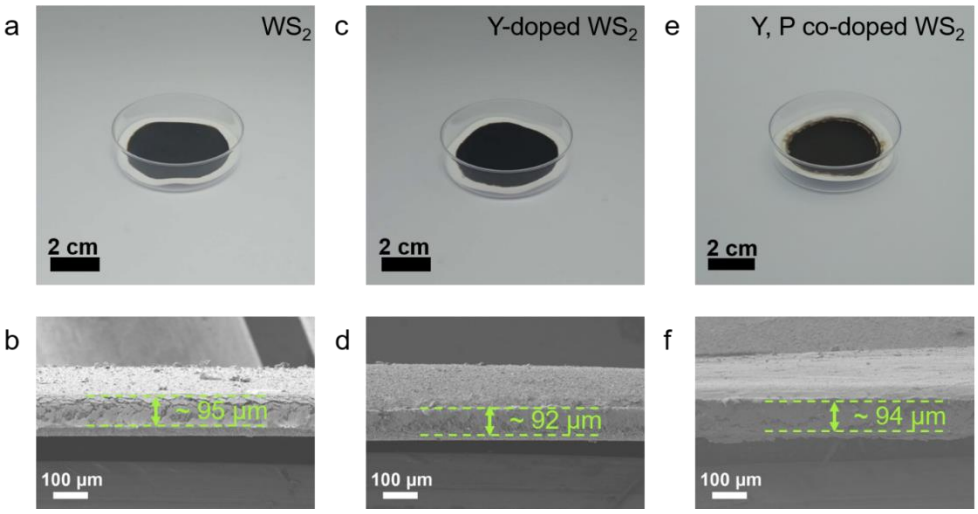

Fig. S63. Morphology characterization of WS_2, Y-doped WS_2 and Y, P co-doped WS_2 thin films from the corresponding nanosheets. a-f, Photographs and thickness analysis of WS_2 (**a**, **b**), Y-doped WS_2 (**b**, **d**) and Y, P co-doped WS_2 (**e**, **f**) thin films, respectively, showing the similar sizes and thicknesses.

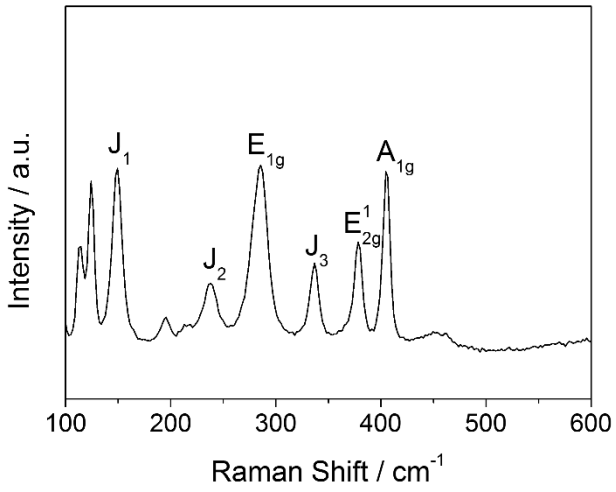

Fig. S64. Raman spectra of P-doped MoS_2 produced from engineering Mo_2GeC by H_2S gas and P vapour. Raman spectra of the resultant P-doped MoS_2, showing three peaks at 149, 237 and 336 cm^{-1}, corresponding to the J_1, J_2 and J_3 peaks of 1T MoS_2 (ref. [33]), respectively. In addition, there are two dominant peaks at 378 and 405 cm^{-1}, indexed to the $E_{2g}{}^1$ and A_{1g} of 2H MoS_2. This demonstrates that 1T and 2H phases are co-existed in the P-doped MoS_2 produced from engineering Mo_2GeC by H_2S gas and P vapour.

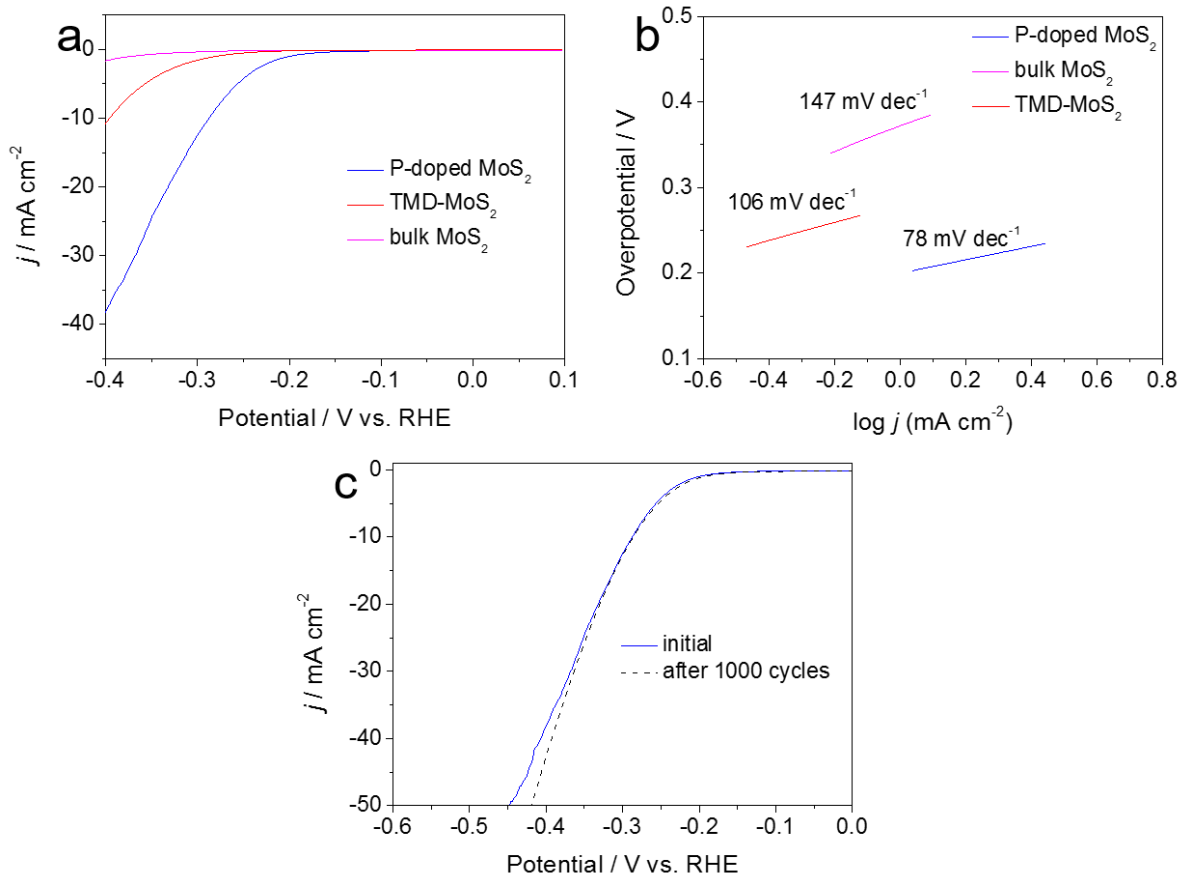

Fig. S65. Electrocatalytic properties of accordion-like MoS_2 (derived from Mo_2GeC by H_2S gas) and P-doped MoS_2 (from engineering Mo_2GeC by H_2S gas and P vapour) for HER. a, Polarization curves of P-doped MoS_2, accordion-like MoS_2 and bulk MoS_2 in a 1 M KOH electrolyte. **b**, Tafel plots derived from the corresponding polarization curves. **c**, Polarization curves before (blue line) and after (black dashed line) 1000 CV sweeps.

Considering the unique accordion-like structure, highly exposed surface and tunable phases of MoS_2 produced from MAX-Mo_2GeC, we preliminarily evaluate the electrocatalytic properties of hydrogen evolution reaction (HER). Clearly, in Figs. S65a and S65b, P-doped MoS_2 with 1T phase exhibits a low Tafel slope of 78 mV dec^{-1}, superior to both accordion-like MoS_2 (106 mV dec^{-1}) and bulk MoS_2 (147 mV dec^{-1}). These results are lower than those reported for 1T MoS_2 for HER

(106 mV dec^{-1})[33], ascribed to the dramatically reduced charge transfer resistance caused by the metallic nature of 1T phase. The current density could be further improved after 1000 CV sweeps by electrochemical activation. Up to 1000 cycles, the P-doped MoS_2 still exhibits a good long-term stability (Fig. S65c).

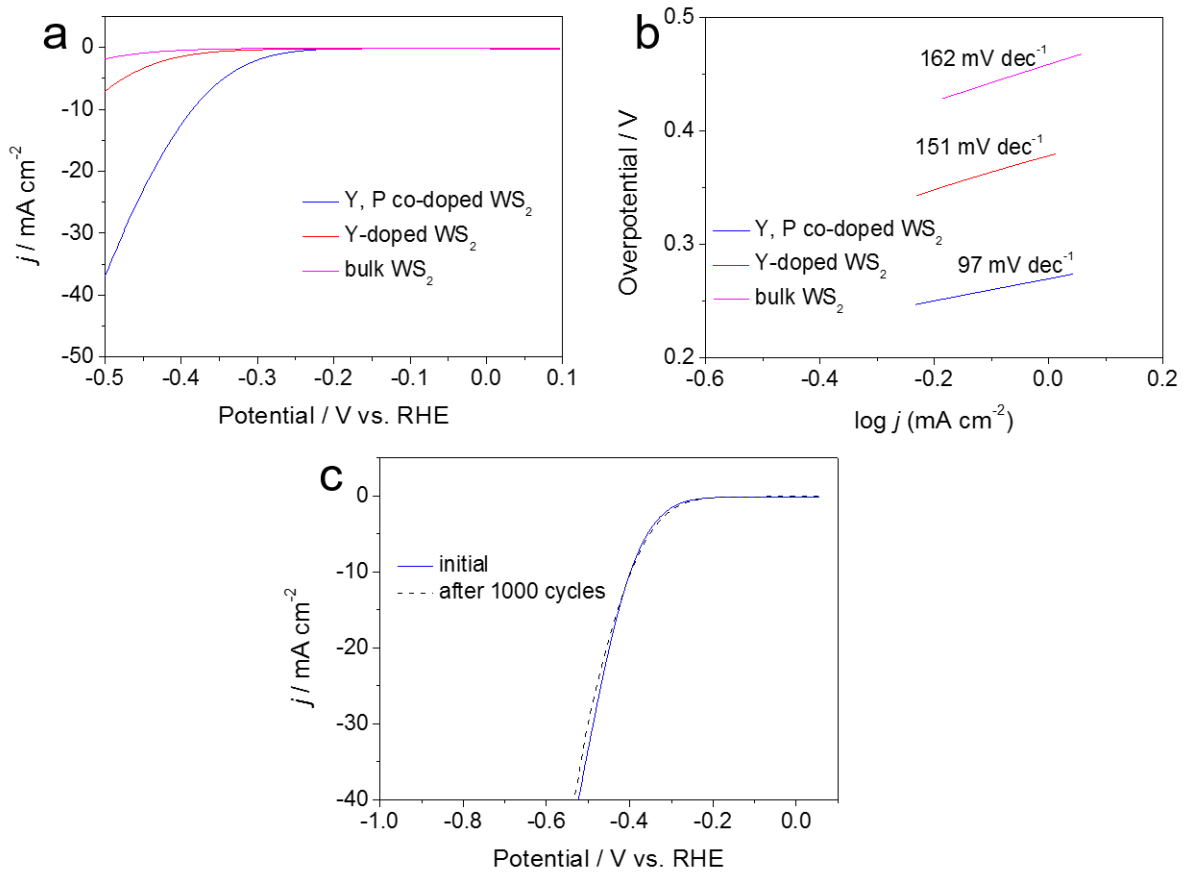

Fig. S66. Electrocatalytic properties of Y, P co-doped WS_2 (derived from $(W_{2/3}Y_{1/3})_2AlC$ by H_2S gas and P vapour) and Y-doped WS_2 (derived from engineering $(W_{2/3}Y_{1/3})_2AlC$ by H_2S gas) for HER. a, Polarization curves of Y, P co-doped WS_2, Y-doped WS_2 and bulk WS_2 in a 1 M KOH electrolyte. **b**, Tafel plots derived from the corresponding polarization curves. **c**, Polarization curves before (blue line) and after (black dashed line) 1000 CV sweeps.

Considering the accordion-like structure and identified 1T phase of P, Y co-doped WS_2, we also evaluate the electrocatalytic properties of hydrogen evolution reaction (HER). As displayed in Figs. S66a and S66b, Y, P co-doped WS_2 with 1T phase exhibits a low Tafel slope of 97 mV dec^{-1}, superior to both Y-doped WS_2 (151 mV dec^{-1}) and bulk WS_2 (162 mV dec^{-1}), ascribed to the dramatically reduced charge transfer resistance caused by the metallic nature of 1T phase. The

current density shows slightly decay after 1000 CV sweeps, indicative of the good stability of Y, P co-doped WS_2 (Fig. S66c).

Table S4. logK_f values for GeS[34].

phase	T/K [1]	logK_f [2]	phase	T/K [1]	logK_f [2]
solid	298.15	13.489	gas	298.15	-8.003
	300	13.407		300	-7.898
	400	10.083		400	-3.711
	500	8.026		500	-1.300
	600	6.634		600	0.258
	700	5.633		700	1.342
	800	4.879		800	2.314
	900	4.224		900	2.666
liquid	1000	3.533		1000	2.829
	1100	3.019		1100	2.959

Notes:

[1] T represents Kelvin temperature.

[2] K_f is equilibrium constant of formation reaction and logK_f values are acquired from the literature[34].

Table S5. logK_f for GeSe[34].

phase	T/K [1]	logK_f [2]	phase	T/K [1]	logK_f [2]
solid	298.15	12.351	gas	298.15	-9.359
	300	12.276		300	-9.246
	400	9.272		400	-4.686
	500	7.459		500	-2.002
	600	6.147		600	-0.345
	700	5.204		700	0.808
	800	4.492		800	1.650
	900	3.936		900	2.288
liquid	1000	3.561		1000	2.784
	1100	3.079		1100	2.942

Notes:

[1] T represents Kelvin temperature.

[2] K_f is equilibrium constant of formation reaction and logK_f values are acquired from the literature[34].

Table S6. logK_f values for SnS[34].

phase	T/K [1]	logK_f [2]	phase	T/K [1]	logK_f [2]
solid-A	298.15	18.585	gas	298.15	-11.407
	300	18.468		300	-11.286
	400	13.755		400	-6.431
	500	10.854		500	-3.630
	600	8.778		600	-1.934
	700	7.280		700	-0.762
	800	6.154		800	0.094
solid-B	900	5.211		900	0.675
	1000	4.208		1000	0.876
	1100	3.392		1100	1.035
liquid	1200	2.772		1200	1.165
	1300	2.316		1300	1.271
	1400	1.932		1400	1.359

Notes:

[1] T represents Kelvin temperature.

[2] K_f is equilibrium constant of formation reaction and logK_f values are acquired from the literature[34].

Table S7. logK_f values for SnSe[34].

phase	T/K [1]	logK_f [2]	phase	T/K [1]	logK_f [2]
sol	298.15	15.335	gas	298.15	-13.798
	300	15.240		300	-13.661
	400	11.373		400	-8.179
	500	9.031		500	-4.951
	600	7.243		600	-3.056
	700	5.948		700	-1.740
	800	4.968		800	-0.779
	900	4.202		900	-0.050
	1000	3.585		1000	0.518
	1100	2.842		1100	0.734

Notes:

[1] T represents Kelvin temperature.

[2] K_f is equilibrium constant of formation reaction and logK_f values are acquired from the literature[34].

Table S8. Boiling points for SiS, Al_2S_3 and Al_2Se_3.

Substance	Boiling Point / K
SiS	1213.15 [1]
Al_2Se_3	1220.15 [2]
Al_2S_3	1773.15 [2]

Note:

[1] Boiling point for SiS is acquired from the literature[35].

[2] Boiling points for Al_2Se_3 and Al_2S_3 can be obtained from *Wikipedia*.

Table S9. XPS peak fitting parameters for the as-prepared transition-metal chalcogenide samples.

Sample	Region	Binding energy / eV	FWHM / eV	Peak ratio	Assigned to
GeS	Ge 3d5/2 (3d3/2)	30.1 (30.7)	0.9	3:2	Ge-S
	Ge 3d5/2 (3d3/2)	32.0 (32.6)	0.9	3:2	Ge-O
	S 2p3/2 (2p1/2)	161.8 (163.0)	0.9	2:1	S-Ge
	S 2p3/2 (2p1/2)	162.9 (164.1)	0.9	2:1	S
SiSe	Si 2p3/2 (2p1/2)	103.2 (104.1)	1.45	2:1	Si-Se
	Si 2p3/2 (2p1/2)	104.6 (105.5)	1.45	2:1	Si-O
SnS	Sn 3d5/2 (3d3/2)	485.7 (494.1)	0.95	3:2	Sn-S
	Sn 3d5/2 (3d3/2)	486.8 (495.2)	0.95	3:2	Sn-O
	S 2p3/2 (2p1/2)	161.0 (162.2)	0.7	2:1	S-Sn (II)
	S 2p3/2 (2p1/2)	161.5 (162.7)	0.8	2:1	S-Sn (IV)
TMD-MoS_2	Mo 3d5/2 (3d3/2)	229.6 (232.8)	0.75	3:2	Mo-S
	S 2s	226.8	1.75	——	S
	S 2p3/2 (2p1/2)	162.4 (163.6)	0.75	2:1	S-Mo
Bulk MoS_2	Mo 3d5/2 (3d3/2)	229.7 (232.8)	0.75	3:2	Mo-S
	S 2s	226.9	1.75	——	S
	S 2p3/2 (2p1/2)	162.5 (163.7)	0.75	2:1	S-Mo
TMD-$TiSe_2$	Ti 2p3/2 (2p1/2)	455.8 (461.9)	1.7	2:1	Ti-Se
	Ti 2p3/2 (2p1/2)	459.0 (465.2)	1.7	2:1	Ti-O
	Se 3d5/2 (3d3/2)	53.8 (54.7)	1.25	3:2	Se-Ti
	Se 3d5/2 (3d3/2)	55.5 (56.3)	1.25	3:2	Se
$MoSe_2$ from MoB	Mo 3d5/2 (3d3/2)	229.1 (232.2)	0.75	3:2	Mo-Se
	Se 3s	230.1	0.8	——	Se
	Se 3d5/2 (3d3/2)	54.6 (55.4)	0.75	3:2	Se-Mo
MoS_2 from MoB	Mo 3d5/2 (3d3/2)	229.5 (232.7)	0.85	3:2	Mo-S
	S 2s	226.7	1.75	——	S
	S 2p3/2 (2p1/2)	162.3 (163.5)	0.85	2:1	S-Mo
$MoSe_2$ from $MoSi_2$	Mo 3d5/2 (3d3/2)	229.1 (232.2)	0.75	3:2	Mo-Se
	Se 3s	230.0	0.8	——	Se
	Se 3d5/2 (3d3/2)	54.5 (55.4)	0.75	3:2	Se-Mo
Y-doped WS_2	W 4f7/2 (4f5/2)	32.5 (34.7)	0.7	4:3	W-S
	S 2p3/2 (2p1/2)	162.2 (163.4)	0.7	2:1	S-W
	Y 3d5/2 (3d3/2)	157.3 (159.4)	1.6	3:2	Y-S
	Y 3d5/2 (3d3/2)	158.6 (160.7)	1.6	3:2	Y-O
Nb-doped $TiSe_2$	Ti 2p3/2 (2p1/2)	459.0 (464.8)	1.7	2:1	Ti-O
	Ti 2p3/2 (2p1/2)	455.6 (461.8)	1.7	2:1	Ti-Se
	Nb 3d5/2 (3d3/2)	203.8 (206.5)	1.1	3:2	Nb-Se
	Nb 3d5/2 (3d3/2)	207.6 (210.3)	1.1	3:2	Nb-O
	Se 3d5/2 (3d3/2)	53.7 (54.5)	1.25	3:2	Se-Ti
	Se 3d5/2 (3d3/2)	55.1 (56.0)	1.25	3:2	Se-Nb

Y, P co-doped WS_2	W 4f7/2 (4f5/2)	32.9 (35.1)	0.7	4:3	W-S
	S 2p3/2 (2p1/2)	162.9 (164.1)	0.7	2:1	S-W
	S 2p3/2 (2p1/2)	161.5 (162.7)	0.7	2:1	S-Y
	S 2p3/2 (2p1/2)	162.1 (163.3)	0.7	2:1	S-P
	Y 3d5/2 (3d3/2)	157.6 (159.7)	1.6	3:2	Y-S
	Y 3d5/2 (3d3/2)	158.6 (160.7)	1.6	3:2	Y-O
	P 2p3/2 (2p1/2)	132.9 (133.7)	1.6	2:1	P-Y
	P 2p3/2 (2p1/2)	133.8 (134.6)	1.6	2:1	P-S

S5. Theory calculations

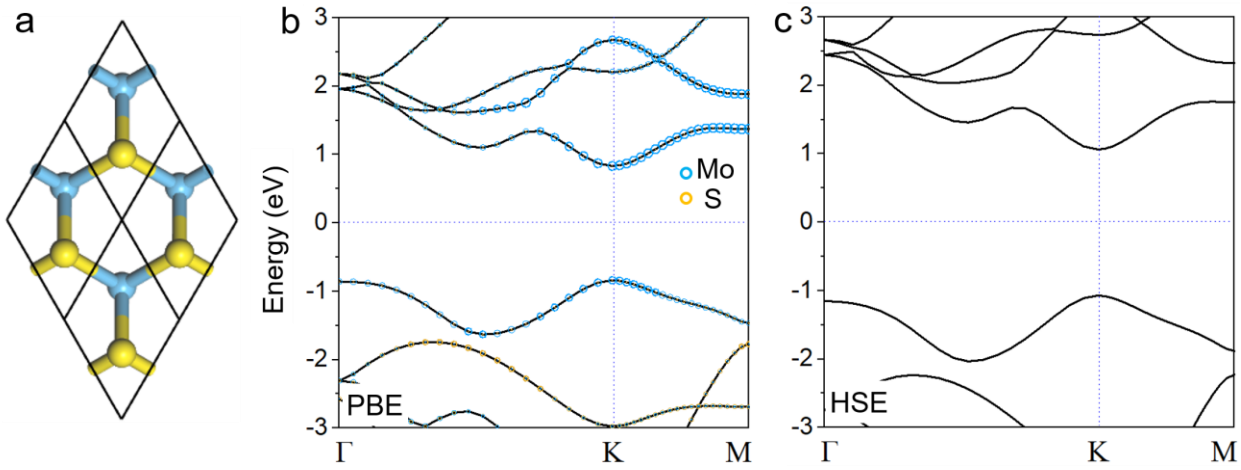

Fig. S67. Calculated band structure for 2H MoS_2 unit cell by PBE and HSE functional. a, Atomic structure of 2H MoS_2 unit cell. **b**, **c**. Calculated band structure of 2H MoS_2 by PBE (**b**) and HSE (**c**) functionals. The blue and yellow circles correspond to the band decomposition of Mo and S atoms, respectively.

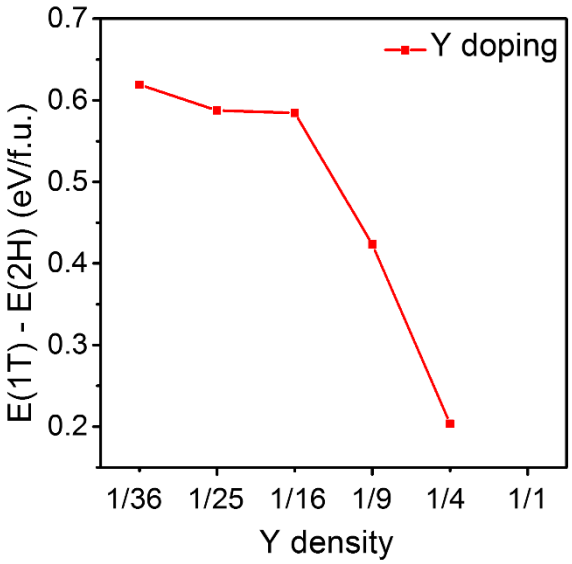

Fig. S68. Energy differences between 1T and 2H phases WS_2 plotted as a function of Y density. Energy differences between 1T and 2H phases (E_{1T}–E_{2H}) of Y-doped WS_2 as a function of Y density, demonstrating that the energy differences significantly decrease with the increasing of Y doping level. However, it remains difficult to reverse the relative stability by Y doping.

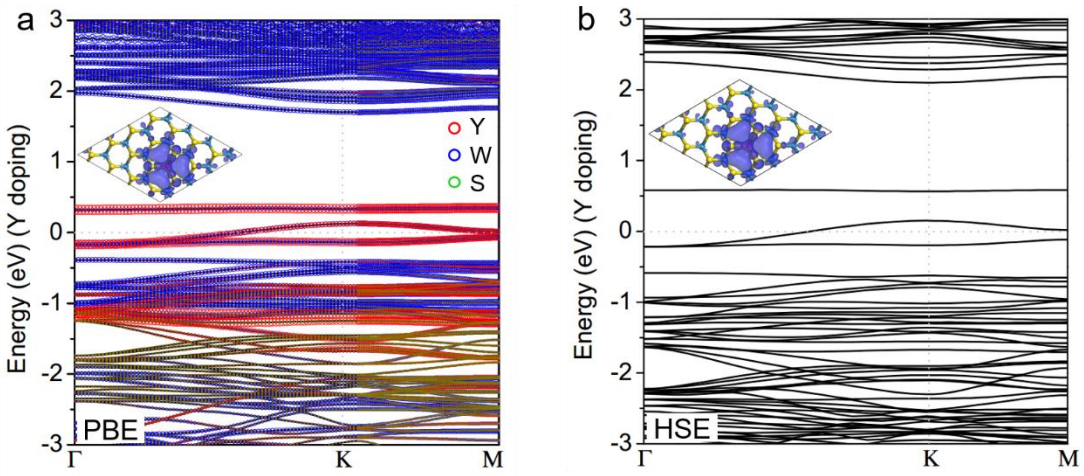

Fig. S69. Calculated band structure for Y-doped WS_2 by PBE and HSE functional. a, **b**. The energy intervals are [-0.3 eV, 0.4 eV] for (**a**) PBE calculation and [-0.5 eV, 0.6 eV] for (**b**) HSE calculation in order to display distributions of similar bands. The isosurface values are 0.02 e/$Å^3$. The red, blue and dark yellow circles correspond to the band decomposition of Y, W and S atoms. The Y-doped WS_2 is calculated with one Y doping in 4×4 supercells of relaxed WS_2 and the corresponding lattice constants are 12.73 Å. Insets are partial charge density distributions of states around the Fermi level by these two methods.

The band structure for Y-doped WS_2 calculated by both PBE (Fig. S69a) and HSE (Fig. S69b) functional reveals that the bands near Fermi level are mainly contributed by Y atoms, corresponding to the localized behavior, which can also be verified by the partial charge density distributions of states around the Fermi level by these two methods (Insets in Fig. S69). Thus the electron transfer ability in Y-doped WS_2 will be weaken.

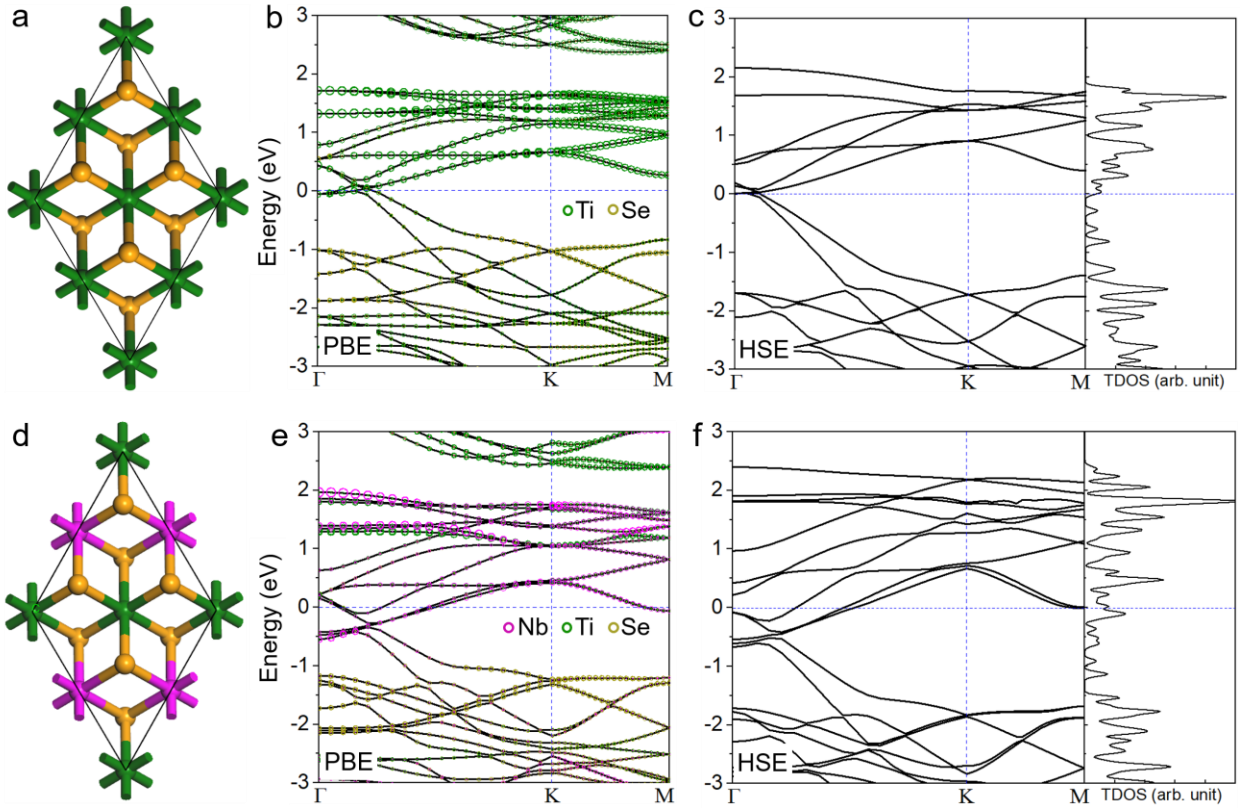

Fig. S70. Calculated band structures of 1T $TiSe_2$ and Nb-doped $TiSe_2$. a, Atomic structure of 1T $TiSe_2$ with 2×2×1 supercell. **b**, Calculated band structure of $TiSe_2$ by PBE functional. **c**, Calculated band structure and total density of states (TDOS) of $TiSe_2$ supercell by HSE functional. **d**, Atomic structure of Nb-doped $TiSe_2$ with 2×2×1 supercell. **e**, Calculated band structure of Nb-doped $TiSe_2$ by PBE functional. **f**, Calculated band structure and TDOS of Nb-doped $TiSe_2$ by HSE functional. Here, the Nb-doped $TiSe_2$ is calculated by replacing half of Ti atoms with Nb atoms. The Fermi energies are set to zero. The purple, dark green and golden circles correspond to the band decomposition of Nb, Ti and Se atoms, respectively.

For 1T $TiSe_2$ and Nb-doped $TiSe_2$, the electrical conductivity σ can be written as $\sigma=\frac{ne^2\tau}{m}$, where n is the electron density, τ is the relaxation time, m is the electron mass. It can be seen that the conductivity is directly proportional to electron density. Intrinsic $TiSe_2$ displays typical metallic

band structure (Fig. S70c), but its density of states around Fermi level is low, so the conductivity is low for metallic $TiSe_2$. After Nb doping, the density of states around Fermi level increases significantly (Fig. S70f), leading to enhanced electrical conductivity for Nb-doped $TiSe_2$.

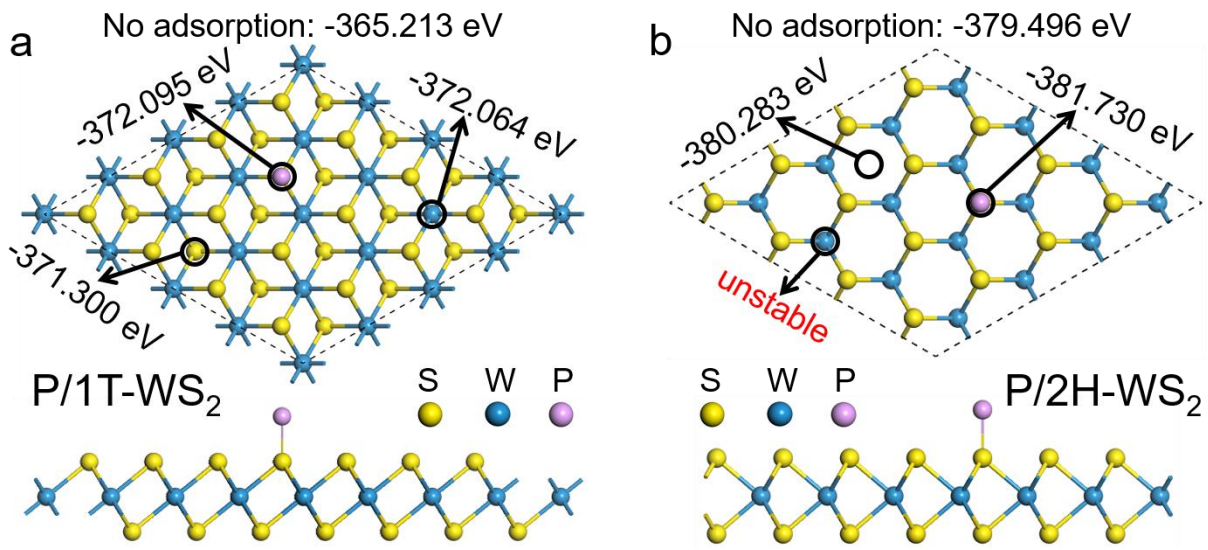

Fig. S71. Adsorption models and calculated energies of P on 1T-/2H-WS_2. a, **b**. Adsorption models and calculated energy for P adsorbed on 1T-WS_2 (**a**) and 2H-WS_2 (**b**), where it tends to form P-S bonds owing to the lowest energy of P on the top of S atom among the different sites (S site, W site and hollow site). Blue W, purple P and yellow S atoms.

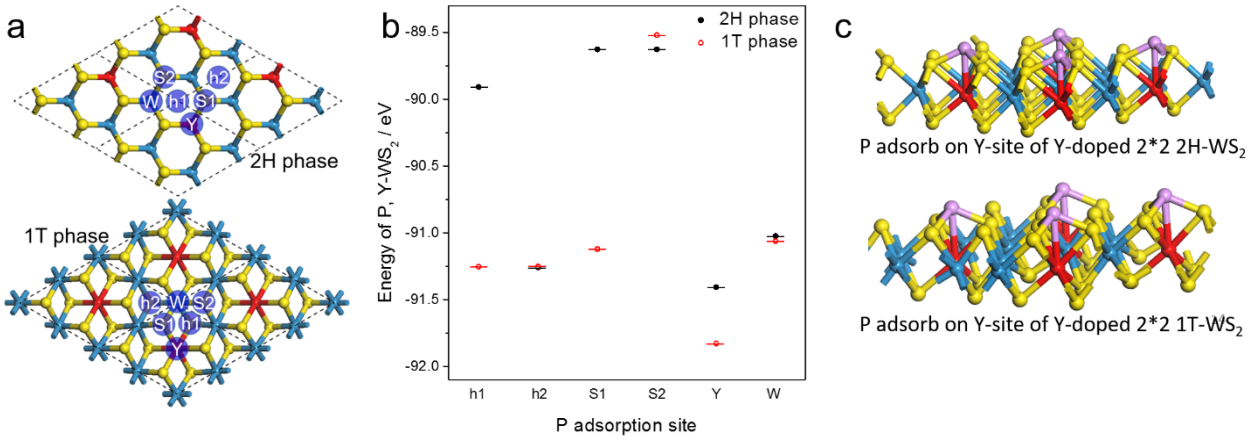

Fig. S72. Atomic configurations for P adsorbed on Y doped 1T-/2H-WS_2. a, Schematic illustration of P adsorption sites on 2H and 1T Y-doped WS_2. **b**, The corresponding energies of P adsorption on different sites in panel (**a**). **c**, P atoms adsorbed on the top of Y atoms will tend to form P-Y bonds, associated with the formation of P-S bonds.

To further gain insight into the P-Y and P-S bonds in P, Y co-doped WS_2, density functional theory calculation was conducted. In Fig. S72a, as P atoms adsorb on the hollow site 2 (h2), sulfur site 2 (S2) and tungsten site (W), the energy differences between 2H and 1T WS_2 are negligible. However, when P atoms adsorb on the top of Y atoms and their neighbors such as hollow site 1 (h1), sulfur site 1 (S1), the energy of 1T WS_2 would be surprisingly lower than that of 2H phases (Fig. S72b), revealing that there is a unique yttrium-phosphorous (Y-P) joint effect that stabilizes the configuration of 1T phase. Therefore, P atoms adsorbed on the top of Y atoms will tend to form P-Y bonds, associated with the formation of P-S bonds, as shown in Fig. S72c.

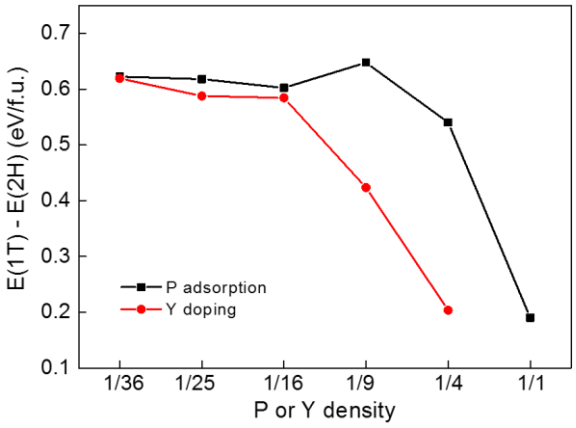

Fig. S73. Energy differences (E_{1T} - E_{2H}) of one P adsorption or one Y-doping in the n×n WS_2 supercells. Theoretically, the energy of 2H-WS_2 is much lower than 1T phase (larger than 0.6 eV per formula unit). The energy differences between these two phases significantly decrease with increasing Y-doping or P-adsorbing density. Nonetheless, we find that it is difficult to reverse the relative energy distribution by independent Y doping or P adsorption.

S6. References

References

1. Meshkian, R. et al. W-based atomic laminates and their 2D derivative $W_{1.33}C$ MXene with vacancy ordering. *Adv. Mater.* **30**, 1706409-1706416 (2018).

2. Naguib, M. et al. Two-dimensional transition metal carbides. *ACS Nano* **6**, 1322-1331 (2012).

3. Anasori, B. et al. Two-dimensional, ordered, double transition metals carbides (MXenes). *ACS Nano* **9**, 9507-9516 (2015).

4. Dong, H. Y., Yan, C. K., Chen, S. Q. & Zhou, Y. C. Solid-liquid reaction synthesis and thermal stability of Ti_2SnC powders. *J. Mater. Chem.* **11**, 1402-1407 (2001).

5. Halim, J. et al. Synthesis and characterization of 2D molybdenum carbide (MXene). *Adv. Funct. Mater.* **26**, 3118-3127 (2016).

6. Coleman, J. N. et al. Two-dimensional nanosheets produced by liquid exfoliation of layered materials. *Science* **331**, 568-571 (2011).

7. Blöchl, P. E. Projector augmented-wave method. *Phys. Rev. B* **50**, 17953-17979 (1994).

8. Kresse, G. & Furthmüller, J. Efficiency of ab-initio total energy calculations for metals and semiconductors using a plane-wave basis set. *Comp. Mater. Sci.* **6**, 15-50 (1996).

9. Monkhorst, H. J. & Pack, J. D. Special points for Brillouin-zone integrations. *Phys. Rev. B* **13**, 5188-5192 (1976).

10. Perdew, J. P., Burke, K. & Ernzerhof, M. Generalized gradient approximation made simple. *Phys. Rev. Lett.* **77**, 3865-3868 (1996).

11. Heyda, J., Scuseria, G. E. & Ernzerhof, M. Hybrid functionals based on a screened Coulomb

potential. *J. Chem. Phys.* **118**, 8207-8215 (2003).

12. Whittles, T. J. et al. Band alignments, valence bands, and core levels in the tin sulfides SnS, SnS_2, and Sn_2S_3: experiment and theory. *Chem. Mater.* **28**, 3718-3726 (2016).

13. Lin, Z. et al. Solution-processable 2D semiconductors for high-performance large-area electronics. *Nature* **562**, 254-258 (2018).

14. Zhou, K.-G., Mao, N.-N., Wang, H.-X., Peng, Y. & Zhang, H.-L. A mixed-solvent strategy for efficient exfoliation of inorganic graphene analogues. *Angew. Chem. Int. Ed.* **50**, 10839-10842 (2011).

15. Qian, Q., Zhang, Z. & Chen, K. J. In situ resonant Raman spectroscopy to monitor the surface functionalization of MoS_2 and WSe_2 for high-k integration: a first-principles study. *Langmuir* **34**, 2882-2889 (2018).

16. Rajaji, V., Janaky, S., Sarma, S. C., Peter, S. C. & Narayana, C. Pressure induced topological and structural phase transitions in 1T-$TiSe_2$: a Raman study. *J. Phys-Condens. Mat.* **31**, 165401-165408 (2019).

17. Cui, L. et al. Raman spectroscopy of optical phonon and charge density wave modes in 1T-$TiSe_2$ exfoliated flakes. *Solid State Commun.* **266**, 21-25 (2017).

18. Duong, D. L. et al. Raman characterization of the charge density wave phase of 1T-$TiSe_2$: from bulk to atomically thin layers. *ACS Nano* **11**, 1034-1040 (2017).

19. Wang, H. et al. Large-area atomic layers of the charge-density-wave conductor $TiSe_2$. *Adv. Mater.* **30**, 1704382-1704388 (2018).

20. Wang, J. et al. Controlled synthesis of two-dimensional 1T-$TiSe_2$ with charge density wave transition by chemical vapour transport. *J. Am. Chem. Soc.* **138**, 16216-16219 (2016).

21. Snow, C. S., Karpus, J. F., Cooper, S. L., Kidd, T. E. & Chiang, T. C. Quantum melting of the charge-density-wave state in 1T-$TiSe_2$. *Phys. Rev. Lett.* **91**, 136402-136405 (2003).

22. Yousaf, M. *et al.* A 3D trilayered CNT/$MoSe_2$/C heterostructure with an expanded $MoSe_2$ interlayer spacing for an efficient sodium storage. *Adv. Energy Mater.* **9**, 1900567-1900577 (2019).

23. Lu, X. et al. Rapid and nondestructive identification of polytypism and stacking sequences in few-layer molybdenum diselenide by Raman spectroscopy. *Adv. Mater.* **27**, 4502-4508 (2015).

24. Yuji Baba, T. A. S. Application of X-ray-induced Auger electron spectroscopy to sate analyses of hydrogen implanted in Y, Zr and Nb metals. *Surf. Interface Anal.* **6**, 171-173 (1984).

25. Jo, S.-H. et al. A high-performance WSe_2/h-BN photodetector using a triphenylphosphine (PPh_3)-based n-doping technique. *Adv. Mater.* **28**, 4824-4831 (2016).

26. Kochat, V. et al. Re doping in 2D transition metal dichalcogenides as a new route to tailor structural phases and induced magnetism. *Adv. Mater.* **29**, 1703754-1703761 (2017).

27. Di Salvo, F. J., Moncton, D. E. & Waszczak, J. V. Electronic properties and superlattice formation in the semimetal $TiSe_2$. *Phys. Rev. B* **14**, 4321-4328 (1976).

28. Vasquez, R. P. XPS core level spectra of some Y compounds. *J. Electron Spectrosc. Relat. Phenom.* **50**, 167-170 (1990).

29. Pelavin, M., Hendrickson, D. N., Hollander, J. M. and Jolly, W. L. Phosphorus 2p electron binding energies correlation with extended Hückel charges. *J. Phys. Chem.* **74**, 1116-1121 (1970).

30. Gresch, R., W. Müller-Warmuth, Dutz, H. X-ray photoelectron spectroscopy of sodium phosphate glasses. *J. Non-Cryst. Solids* **34**, 127-136 (1979).

31. Zhou, J. et al. A library of atomically thin metal chalcogenides. *Nature* **556**, 355-359 (2018).

32. Voiry, D. et al. Enhanced catalytic activity in strained chemically exfoliated WS_2 nanosheets for hydrogen evolution. *Nat. Mater.* **12**, 850-855 (2013).

33. Huang, Y. et al. Atomically engineering activation sites onto metallic 1T-MoS_2 catalysts for enhanced electrochemical hydrogen evolution. *Nat. Commun.* **10**, 982-992 (2019).

34. Barin, I. *Thermochemical Data of Pure Substances, Third Edition*, VCH Verlagsgesellschaft mbH, Weinheim (1995).

35. Yaws, C. L. *The Yaws of Handbook of Physical Properties for Hydrocarbons and Chemicals, Second Edition*, Elsevier Inc, Oxford (2015).